



**HAL**  
open science

# Contribution to numerical simulation analysis of the flow in the ram accelerator in Subdetonative combustion mode

Tarek Bengherbia

► **To cite this version:**

Tarek Bengherbia. Contribution to numerical simulation analysis of the flow in the ram accelerator in Subdetonative combustion mode. Engineering Sciences [physics]. ISAE-ENSMA Ecole Nationale Supérieure de Mécanique et d'Aérotechnique - Poitiers, 2009. English. NNT: . tel-00491860

**HAL Id: tel-00491860**

**<https://theses.hal.science/tel-00491860>**

Submitted on 14 Jun 2010

**HAL** is a multi-disciplinary open access archive for the deposit and dissemination of scientific research documents, whether they are published or not. The documents may come from teaching and research institutions in France or abroad, or from public or private research centers.

L'archive ouverte pluridisciplinaire **HAL**, est destinée au dépôt et à la diffusion de documents scientifiques de niveau recherche, publiés ou non, émanant des établissements d'enseignement et de recherche français ou étrangers, des laboratoires publics ou privés.

# THESE

Pour l'obtention de Grade de  
DOCTEUR DE L'ECOLE NATIONALE SUPERIEUR DE MECANIQUE ET  
D'AEROTECHNIQUE  
(Diplôme National – Arrêté du 7 aout 2006)

Ecole Doctorale : Science pour l'Ingénieur et Aéronautique

Secteur de Recherche : Combustion.

Présentée par :

**Tarek Bengherbia**

\*\*\*\*\*

## CONTRIBUTION TO NUMERICAL SIMULATION ANALYSIS OF THE FLOW IN THE RAM ACCELERATOR IN THE SUBDETONATIVE PROPULSION MODE

\*\*\*\*\*

Directeur de Thèse:

**Professeur Pascal Bauer**

Co-directeur de thèse :

**Dr. Yufeng Yao**

Soutenu le : 03 Décembre 2009

devant la Commission d'Examen

\*\*\*\*\*

### JURY

M. Pascal BAUER, Professeur à l'ENSMA, Examineur

M. Michel CHAMPION, Directeur de Recherche CNRS, Poitiers, Examineur

M. Amer CHPOUN, Professeur à l'Université d'Evry, Examineur

M. Marc GIRAUD, Dr. Ingénieur, Expert en Science Balistique, Exobal, Saint-Louis, Examineur

Dr. Carl KNOWLEN, Senior Researcher, University of Washington, Seattle, USA, Rapporteur

M. Yufeng YAO, Directeur de l'Aerospace Research Centre, Kingston University, Londres, Examineur

M. David ZEITOUN, Professeur à l'Université de Provence, Rapporteur

*To my mum Yamena  
and my wife Gonca.*

# Table of Contents

Table of Contents	v
List of Tables	viii
List of Figures	ix
Résumé	i
Abstract	iii
Acknowledgements	v
Introduction	1
<b>1 Quasi-steady and unsteady one-dimensional modeling of ram accelerator in thermally choked propulsion mode</b>	<b>19</b>
1.1 Introduction . . . . .	19
1.2 Unsteady 1-D conservation equations . . . . .	20
1.3 Calculation procedure . . . . .	24
1.4 Comparison with experimental data . . . . .	25
1.5 Compressibility effects of unreacted propellant on thermally choked ram accelerator performance . . . . .	34
1.6 Summary . . . . .	37
<b>2 Conservation equations for reacting flows</b>	<b>39</b>
2.1 Introduction . . . . .	39
2.2 primitive variables . . . . .	39
2.3 Thermochemistry . . . . .	40
2.4 Viscous tensor . . . . .	43

2.5	Molecular transport of species and heat . . . . .	43
2.6	Chemical kinetics . . . . .	44
2.7	Stoichiometry in premixed flames . . . . .	45
2.8	Conservation of momentum . . . . .	46
2.9	Conservation of mass and species . . . . .	46
2.10	Conservation of energy . . . . .	47
2.11	Summary . . . . .	50
<b>3</b>	<b>Turbulent combustion modeling</b>	<b>51</b>
3.1	Introduction . . . . .	51
3.2	Elementary notion of turbulence . . . . .	52
3.3	RANS simulation for turbulent combustion . . . . .	55
3.3.1	Averaging the balance equations . . . . .	55
3.3.2	Unclosed terms in Favre averages balance equations . . . . .	57
3.4	Classical turbulence models . . . . .	59
3.4.1	The Two-equation model $k - \varepsilon$ . . . . .	59
3.4.2	The Two-equation model $k - \omega$ . . . . .	60
3.4.3	The Base Line model ( <i>BSL</i> ) . . . . .	64
3.4.4	The Shear Stress Transport model ( <i>SST</i> ) . . . . .	65
3.5	Turbulent premixed flames . . . . .	66
3.5.1	Introduction . . . . .	66
3.5.2	Interaction between turbulence and chemical kinetics . . . . .	68
3.5.3	The Arrhenius approach . . . . .	69
3.5.4	The Eddy Break Up (EBU) model . . . . .	70
3.5.5	The Eddy Dissipation Model (EDM) . . . . .	70
3.6	Summary . . . . .	73
<b>4</b>	<b>Numerical modeling</b>	<b>75</b>
4.1	Introduction . . . . .	75
4.2	Geometry . . . . .	76
4.3	Two-dimensional simulations . . . . .	77
4.4	Computational procedure . . . . .	77
4.4.1	Mesh guidelines . . . . .	78
4.4.2	Wall function . . . . .	80
4.5	Determining turbulence parameters . . . . .	83
4.5.1	Turbulence intensity . . . . .	83
4.5.2	Turbulence length scale . . . . .	84
4.5.3	Boundary conditions . . . . .	85

4.6	Radiation . . . . .	87
4.6.1	Spherical harmonic method . . . . .	90
4.6.2	Boundary condition treatment for the P-1 model at walls . . . . .	91
4.7	Combustion setup . . . . .	93
4.7.1	Reaction mechanism . . . . .	93
4.8	Flame radiation losses . . . . .	96
4.9	Initialization . . . . .	97
4.10	Summary . . . . .	97
<b>5</b>	<b>Results and discussion</b>	<b>98</b>
5.1	Introduction . . . . .	98
5.2	The influence of the reactional mechanism . . . . .	99
5.3	Comparison with the experimental data . . . . .	103
5.4	Thrust . . . . .	127
5.5	Summary . . . . .	129
<b>6</b>	<b>Refinement on the one dimensional ram accelerator model</b>	<b>131</b>
6.1	Introduction . . . . .	131
6.2	Influence of the control volume length in the unsteady assumption . . . . .	133
6.3	Summary . . . . .	138
<b>7</b>	<b>Conclusion</b>	<b>139</b>
7.1	Future work . . . . .	141
<b>A</b>	<b>Appendix A: One dimensional model</b>	<b>143</b>
A.1	Introduction . . . . .	143
A.2	Real gas effects on the prediction of ram accelerator performance . . . . .	147
A.3	Equations of state . . . . .	149
A.3.1	Boltzmann . . . . .	150
A.3.2	Percus-Yevick . . . . .	150
A.3.3	Becker-Kistiakowsky-Wilson (BKW) . . . . .	151
<b>B</b>	<b>Appendix B: Ram accelerator projectile geometry and scaling</b>	<b>153</b>
<b>C</b>	<b>Appendix C: Convergence history</b>	<b>155</b>
	<b>Bibliography</b>	<b>159</b>

# List of Tables

1.1	Computed and experimental Chapman-Jouguet speed . . . . .	25
4.1	Mesh size near the wall . . . . .	79
4.2	Mesh size . . . . .	80
4.3	Turbulent intensity and turbulent length scale . . . . .	86
4.4	Reaction rate equation data, one step . . . . .	94
4.5	Reaction rate equation data, two steps . . . . .	94
4.6	Reaction rate equation data, five steps . . . . .	95
5.1	Maximum Pressure & Temperature, in-coming velocity $V_0 = 1829 \text{ m/s}$ . .	101
5.2	Radiation effects, in-coming velocity $V_0 = 1829 \text{ m/s}$ . . . . .	102
5.3	Thrust, in-coming velocity $V_0 = 1829 \text{ m/s}$ . . . . .	103
5.4	Pressure tracers position . . . . .	104
6.1	The control volume function of the incoming velocity . . . . .	136

# List of Figures

1	Ram accelerator vs ramjet . . . . .	2
2	Ram accelerator launcher system . . . . .	2
3	Ram accelerator combustion regimes . . . . .	4
1.1	Schematic of the one-dimensional control volume . . . . .	21
1.2	Algorithm for quasi-steady calculation . . . . .	26
1.3	Algorithm for unsteady calculation . . . . .	27
1.4	Non-dimensional Thrust-Mach plot for $2.95CH_4 + 2O_2 + 5.7N_2$ propellant with quasi-steady modeling (Ideal gas EoS was used at station 1, and various real gas EoS at station 2.), $P_1 = 5.15 MPa$ . . . . .	29
1.5	Non-dimensional Thrust-Mach plot for $2.95CH_4 + 2O_2 + 5.7N_2$ propellant with unsteady modeling (Ideal gas EoS was used at station 1, and various real gas EoS at station 2.); $L_{CV} = 2L_p$ , $P_1 = 5.15 MPa$ . . . . .	30
1.6	Velocity-distance plot for $2.95CH_4 + 2O_2 + 5.7N_2$ propellant with quasi-steady modeling (Ideal gas EoS was used at station 1, and various real gas EoS at station 2.), $P_1 = 5.15 MPa$ . . . . .	31
1.7	Velocity-distance plot for $2.95CH_4 + 2O_2 + 5.7N_2$ propellant with unsteady modeling (Ideal gas EoS was used at station 1, and and various real gas EoS at station 2.), $L_{CV} = 2L_p$ , $P_1 = 5.15 MPa$ . . . . .	32



1.8	Non-dimensional Thrust-Mach plot for $2.95CH_4 + 2O_2 + 5.7N_2$ propellant at $p_1 = 5.15$ MPa; $L_{CV} = 2L_p$ (Ideal gas EoS was used at station 1, and Boltzmann EoS was used for the calculation of properties of combustion products) . . . . .	33
1.9	Velocity-distance plot for $2.95CH_4+2O_2+5.7N_2$ propellant at $p_1 = 5.15$ MPa; $L_{CV} = 2L_p$ (Ideal gas EoS was used at station 1, and Boltzmann EoS was used for the calculation of properties of combustion products) . . . . .	33
1.10	Non-dimensional Thrust-Mach plot for $2.6CH_4 + 2O_2 + 5.92N_2$ propellant, $p_1 = 15$ MPa; $L_{CV} = 2L_p$ (Ideal gas EoS was used at station 1, and Boltzmann EoS was used for the calculation of properties of combustion products), Experimental data from [54] . . . . .	35
1.11	Non-dimensional Thrust-Mach plot for $2.6CH_4 + 2O_2 + 5.92N_2$ propellant, $p_1 = 20$ MPa; $L_{CV} = 2L_p$ (Ideal gas EoS was used at station 1, and Boltzmann EoS was used for the calculation of properties of combustion products), Experimental data from [54] . . . . .	35
1.12	Non-dimensional Thrust-Velocity plot for $2.95CH_4 + 2O_2 + 5.7N_2$ at $P_1 = 20$ MPa (Boltzmann EoS was used for the calculation of properties of combustion products) . . . . .	36
4.1	3D geometry to be considered in the simulation . . . . .	77
4.2	Multi-bloc structured mesh topology for 2-D flow . . . . .	78
4.3	Planck mean absorption coefficient for $CO_2$ , $H_2O$ , $CH_4$ and $CO$ as function of gas temperature [133] . . . . .	96
5.1	Temperature profiles on the projectile body and the center line, using one, two, and five steps reaction mechanism, in-coming velocity $V_0 = 1829$ m/s	100
5.2	Pressure profiles on the projectile body and the center line, using one, two, and five steps reaction mechanism, in-coming velocity $V_0 = 1829$ m/s . . .	100
5.3	Pressure profiles on the tube wall, Experimental velocity= $1240$ m/s . . . .	109
5.4	Pressure profiles on the tube wall, Experimental velocity= $1240$ m/s . . . .	109

5.5	Pressure profiles on the tube wall, Experimental velocity=1370m/s . . . . .	110
5.6	Pressure profiles on the tube wall, Experimental velocity; P6=1470m/s, P8=1520m/s . . . . .	110
5.7	Pressure profiles on the tube wall, Experimental velocity; P8=1520m/s, P10=1590m/s . . . . .	111
5.8	Pressure profiles on the tube wall, Experimental velocity; P10=1590m/s, P11=1620m/s . . . . .	111
5.9	Pressure profiles on the tube wall, Experimental velocity; P15=1710m/s, P16=1740m/s . . . . .	112
5.10	Pressure profiles on the tube wall, Experimental velocity; P16=1740m/s, P	112
5.11	Pressure field map of the ram accelerator, CFD calculations ( <i>Top</i> ), Experimental data ( <i>bottom</i> ), velocity=1091 - 2035m/s . . . . .	113
5.12	Pressure field map of the ram accelerator, Experimental data ( <i>Top</i> ), CFD calculations ( <i>bottom</i> ), velocity=1091 - 2035m/s . . . . .	114
5.13	Pressure contours, in-coming velocity=1091m/s . . . . .	115
5.14	Pressure contours, in-coming velocity=1173m/s . . . . .	115
5.15	Pressure contours, in-coming velocity=1247m/s . . . . .	115
5.16	Pressure contours, in-coming velocity=1374m/s . . . . .	115
5.17	Pressure contours, in-coming velocity=1476m/s . . . . .	115
5.18	Pressure contours, in-coming velocity=1519m/s . . . . .	116
5.19	Pressure contours, in-coming velocity=1622m/s . . . . .	116
5.20	Pressure contours, in-coming velocity=1733m/s . . . . .	116
5.21	Pressure contours, in-coming velocity=1829m/s . . . . .	116
5.22	Pressure contours, in-coming velocity=1842m/s . . . . .	116
5.23	Pressure contours, in-coming velocity=1891m/s . . . . .	117
5.24	Pressure contours, in-coming velocity=1900m/s . . . . .	117
5.25	Pressure contours, in-coming velocity=1917m/s . . . . .	117
5.26	Pressure contours, in-coming velocity=1930m/s . . . . .	117
5.27	Pressure contours, in-coming velocity=1943m/s . . . . .	117

5.28	Pressure contours, in-coming velocity=1519m/s . . . . .	118
5.29	Pressure contours, in-coming velocity=2007m/s . . . . .	118
5.30	Pressure contours, in-coming velocity=2017m/s . . . . .	118
5.31	Pressure contours, in-coming velocity=2027m/s . . . . .	118
5.32	Pressure contours, in-coming velocity=2035m/s . . . . .	118
5.33	Temperature contours, in-coming velocity=1091m/s . . . . .	119
5.34	Temperature contours, in-coming velocity=1173m/s . . . . .	119
5.35	Temperature contours, in-coming velocity=1247m/s . . . . .	119
5.36	Temperature contours, in-coming velocity=1374m/s . . . . .	119
5.37	Temperature contours, in-coming velocity=1476m/s . . . . .	119
5.38	Temperature contours, in-coming velocity=1519m/s . . . . .	120
5.39	Temperature contours, in-coming velocity=1622m/s . . . . .	120
5.40	Temperature contours, in-coming velocity=1733m/s . . . . .	120
5.41	Temperature contours, in-coming velocity=1829m/s . . . . .	120
5.42	Temperature contours, in-coming velocity=1842m/s . . . . .	120
5.43	Temperature contours, in-coming velocity=1891m/s . . . . .	121
5.44	Temperature contours, in-coming velocity=1900m/s . . . . .	121
5.45	Temperature contours, in-coming velocity=1817m/s . . . . .	121
5.46	Temperature contours, in-coming velocity=1930m/s . . . . .	121
5.47	Temperature contours, in-coming velocity=1943m/s . . . . .	121
5.48	Temperature contours, in-coming velocity=1519m/s . . . . .	122
5.49	Temperature contours, in-coming velocity=2007m/s . . . . .	122
5.50	Temperature contours, in-coming velocity=2017m/s . . . . .	122
5.51	Temperature contours, in-coming velocity=2027m/s . . . . .	122
5.52	Temperature contours, in-coming velocity=2035m/s . . . . .	122
5.53	Mach number contours, in-coming velocity=1091m/s . . . . .	123
5.54	Mach number contours, in-coming velocity=1173m/s . . . . .	123
5.55	Mach number contours, in-coming velocity=1247m/s . . . . .	123
5.56	Mach number contours, in-coming velocity=1374m/s . . . . .	123

5.57	Mach number contours, in-coming velocity= $1476m/s$ . . . . .	123
5.58	Mach number contours, in-coming velocity= $1519m/s$ . . . . .	124
5.59	Mach number contours, in-coming velocity= $1622m/s$ . . . . .	124
5.60	Mach number contours, in-coming velocity= $1733m/s$ . . . . .	124
5.61	Mach number contours, in-coming velocity= $1829m/s$ . . . . .	124
5.62	Mach number contours, in-coming velocity= $1842m/s$ . . . . .	124
5.63	Mach number contours, in-coming velocity= $1891m/s$ . . . . .	125
5.64	Mach number contours, in-coming velocity= $1900m/s$ . . . . .	125
5.65	Mach number contours, in-coming velocity= $1817m/s$ . . . . .	125
5.66	Mach number contours, in-coming velocity= $1930m/s$ . . . . .	125
5.67	Mach number contours, in-coming velocity= $1943m/s$ . . . . .	125
5.68	Mach number contours, in-coming velocity= $1519m/s$ . . . . .	126
5.69	Mach number contours, in-coming velocity= $2007m/s$ . . . . .	126
5.70	Mach number contours, in-coming velocity= $2017m/s$ . . . . .	126
5.71	Mach number contours, in-coming velocity= $2027m/s$ . . . . .	126
5.72	Mach number contours, in-coming velocity= $2035m/s$ . . . . .	126
5.73	Comparison of the CFD predicted thrust with experimental data. . . . .	127
5.74	Thrust vs velocity . . . . .	128
6.1	Non-dimensional Thrust-Mach plot for $2.95CH_4 + 2O_2 + 5.7N_2$ propellant with quasi-steady and unsteady modeling; $L_{CV} = 2L_p$ , $P_0 = 5.15MPa$ , (Ideal gas EoS was used at station 1, and Boltzmann EoS was used for the calculation of properties of combustion products) . . . . .	132
6.2	Non-dimensional Thrust-Mach plot for $2.95CH_4+2O_2+5.7N_2$ propellant), $P_0 = 5.15MPa$ , various values for $L_{CV}$ were used (Ideal gas EoS was used at station 1, and Boltzmann EoS was used for the calculation of properties of combustion products) . . . . .	134

6.3	Velocity-distance plot for $2.95CH_4+2O_2+5.7N_2$ propellant, $P_0 = 5.15MPa$ , various values for $L_{CV}$ were used (Ideal gas EoS was used at station 1, and Boltzmann EoS was used for the calculation of properties of combustion products) . . . . .	134
6.4	Non-dimensional Thrust-Mach plot for $2.95CH_4 + 2O_2 + 5.7N_2$ propellant, $P_0 = 5.15MPa$ , various values for $L_{CV}$ were used (Ideal gas EoS was used at station 1, and Boltzmann EoS was used for the calculation of properties of combustion products) . . . . .	137
6.5	Velocity-distance plot for $2.95CH_4+2O_2+5.7N_2$ propellant, $P_0 = 5.15MPa$ , various values for $L_{CV}$ were used (Ideal gas EoS was used at station 1, and Boltzmann EoS was used for the calculation of properties of combustion products) . . . . .	137
A.1	Control volume model used for the numerical analysis . . . . .	143
C.1	Convergence history for the velocity and pressure (Top, $V_0 = 1120 m/s$ , Bottom, $V_0 = 1829 m/s$ ) . . . . .	156
C.2	Convergence history for mass fraction of the fuel and the combustion products (Top, $V_0 = 1120 m/s$ , Bottom, $V_0 = 1829 m/s$ ) . . . . .	157
C.3	Monitoring points at different locations in the computational domain showing that the steady state solution has been achieved. i.e., presented here are the Temperature and velocity (Top, $V_0 = 1120 m/s$ , Bottom, $V_0 = 1829 m/s$ ) . . . . .	158

# Résumé

## **Contribution à l'étude des performances d'un accélérateur à effet stato en régime sous-détonatif**

La faisabilité de l'accélérateur par effet stato, désigné par le terme raccourci 'RAMAC' (tiré de la dénomination anglo-saxonne 'ram accelerator'), a été démontrée en 1986 à l'Université de Washington. Depuis, ce type d'accélérateur fait l'objet de nombreuses études destinées à accroître, in fine, ses performances jusqu'à ses limites physiques. Un des atouts potentiels considérables par rapport aux canons à poudre classiques réside dans la possibilité de lancer des masses conséquentes sans avoir recours à des pressions rédhibitoires. En effet, la vitesse finale obtenue avec un procédé RAMAC dépend, entre autres, de la longueur du tube, et les niveaux de pression finalement atteints sont indépendants de la masse et de la taille du projectile. Si la possibilité d'augmenter calibre et longueur du tube sans limitations technologiques se confirme, le principe RAMAC pourrait être utilisé pour accélérer des projectiles de masse importante à des vitesses hypersoniques, lui conférant ainsi un avantage indéniable sur tous les autres types de lanceurs. L'accélération du projectile se déroule en trois phases correspondant aux régimes dits sous-détonatif, trans-détonatif et super-détonatif, caractérisés chacun par la vitesse relative du projectile comparée à la célérité de la détonation dans le mélange considéré. Le mode sous-détonatif est, à l'heure actuelle, le mieux connu. Le laboratoire de l'Université Washington possède, à cet égard, un grand nombre de données expérimentales. Un développement important de cette technologie avait été fait à l'Institut Franco-allemand de Recherches de Saint-Louis (ISL), sous l'impulsion

de M. Giraud, qui a été un des précurseurs pour l'étude de cette technologie, en tube lisse de calibre 90 mm ds 1992 pour le mode de combustion sous-détonatif, étudié ensuite mode de combustion surper-détonatif dans un tube rainuré de calibre 30 mm par les chercheurs de l'équipe allemande. La compréhension des phénomènes mis en jeu dans cette technologie est subordonnée à une importante étude expérimentale associée à la mise au point de moyens numériques. Le travail présenté dans ce mémoire a pour objectif d'analyser par voie numérique le processus de combustion qui s'opère autour du projectile. Il s'agit d'interpréter les résultats générés par un code CFD de combustion turbulente. Ces résultats sont comparés aux données expérimentales existantes disponibles au Laboratoire de l'Université de Washington. Les valeurs calculées ont permis de parfaire la fiabilité d'un code de calcul monodimensionnel en régime sous-détonatif basé sur la résolution analytique et numérique des équations de conservation en instationnaire. En effet, dans le cas de pressions initiales très élevées, atteignant 20 MPa, l'accélération générée ne permet plus de se référer à un régime stationnaire. D'autre part, le choix de l'équation d'état des produits de combustion devient primordial. Pour ces raisons, les calculs analytiques font intervenir des équations d'état dont la validité est discutée. La poussée générée par l'accélérateur est calculée et les valeurs déduites de cette analyse 1D sont en excellent accord avec les expériences. Cette démarche a pour but d'apporter une contribution en termes de prédiction des performances de poussée d'un accélérateur à effet stato et de choix du mélange réactif optimal.

# Abstract

## **Thrust Prediction of the Ram Accelerator in the Sub-Detonative Combustion Mode**

The ram accelerator is a ramjet-in-tube hypervelocity launcher that uses chemical energy to propel projectiles to very high velocities. A projectile similar to centerbody of a supersonic ramjet travels through a tube filled with high pressure combustible gas, which burns on or behind the projectile to provide the thrust. The ram accelerator was first introduced in 1983 at University Washington; many facilities have been setup, in USA, France/Germany, Japan, and China. Velocities up to 2.7Km/s have been attained with 38mm, 75g projectiles at University of Washington, 2.2Km/s with 90mm, 1Kg projectiles at ISL-France, and 2.0Km/s with 120mm, 5Kg projectiles at the U.S Army Research Laboratory, and 2.3km/s with 25mm, 12g projectiles at Tohoku University, Japan. Three velocity regimes, centered about the CJ detonation speed, have been identified that exhibits different acceleration characteristics, indicating the existence of different propulsive cycles. One of these propulsive cycles is the thermally choked ram accelerator mode, which operates with in-tube Mach numbers typically ranging from 2.5 to 5 and at projectile velocities below the Chapman-Jouguet detonation speed of the propellant mixture. Our research program focuses on predicting the ram accelerator performances in the thermally choked propulsive mode. Two approaches have been applied, the first is to develop a one-dimensional computer program which includes the quasi-steady and unsteady assumption. This program incorporates the following equations of state: ideal gas, Boltzmann, Percus-Yevick, and Becker-Kistiakowsky-Wilson. The second approach is to use the Computational



fluid dynamics solutions of the Reynolds Averaged Navier-Stokes equations to numerically predict the thrust in the thermally choked propulsive mode. Simulations were carried out for a series of in-coming velocities. The shear-stress transport turbulence model and the eddy dissipation combustion model, with detailed reaction mechanism have been used to simulate the fully turbulent reactive flow field in the ram accelerator. Simulations take into account the effect of the radiation/turbulence interactions. The spherical harmonic P1 method was used, the gray medium assumption is employed and the Planck-mean absorption coefficients are used to determine the radiative properties of the gas-phase species. The predicted thrust from the one-dimensional modeling and the CFD simulation were compared with data from a representative experiment at the University of Washington 38-mm-bore facility.

# Acknowledgements

I would like to give my special thanks to everybody who provided me with the inspiration and guidance to complete this body of work.

I am touched to have been able to work with such dedicated professionals in their field. In particular I would like to pay tribute to Professor Pascal Bauer for providing the overall direction, in particular the special guidance he gave for the analytical and thermodynamics part of this work. It has been a unique experience to be under his tutelage. I would also like to give special thanks to Professor Michel Champion for his expert guidance regarding turbulent combustion since the early stage of this work. None of this would be possible without the kindness and help that Dr Yufeng Yao has afforded me by providing the computer tools, software and platform needed to conduct my research. I am very privileged to have been able to work closely with Dr. Carl Knowlen and I thank him for his insightful comments and guidance with regards to providing and interpreting the data. I am indebted to him for the endless hours he has spent with me to keep me on track. Also, on a personal level he has been a motivation for me to succeed and do the very best I can. I would like express my appreciation to both Professor Amer Chpoun for being part of the jury and Professor David Zeitoun for his review despite being extremely busy with University work. I am extremely grateful the time and expertise that is being afforded to me. Lastly, I would like to thank Dr, Marc Giraud, Expert en Science Balistique, for his high level knowledge of the ramac and ballistics and his pioneering work in this technology. On a personal level I would like to thank Dr. Mohamed Maida, and Dr Assia Maida, for their insightful commentary on my work. Finally, I would like to thank my beautiful Gonca for her love and encouragement and most of all I am grateful to my parents

for their patience and *love* love. Without them this work would never have come into existence (literally).

# Introduction

In 1962 a French engineer named Costes, who worked at the "Commissariat à l'Énergie Atomique" wrote a paper about accelerating projectiles in tubes filled with gases, and described the projectile thrust that is generated by the combustion of the propellant in the tube. In 1983, Hertzberg [1] re-invented this concept, and called it "Ram accelerator". The positive results from the experiments were obtained in 1986 at the University of Washington in Seattle. The principle of this concept still remains the same, as described by Hertzberg [1].

The projectile in the ram accelerator resembles the centerbody of the ramjet and the tube wall acts as its outer cowling. Both devices use a normal shock wave system to decelerate the flow to subsonic for combustion, figure 1. Unlike the air breathing ramjet, the ram accelerator does not have a nozzle to mechanically choke the flow. Instead, the flow of combustion products is choked by the heat release itself at full tube area (thermal choking). Another key difference is that the ramjet must carry fuel and inject it into the incoming air, whereas the ram accelerator projectile does not carry fuel. Instead, it travels through an atmosphere of premixed fuel and oxidizer, figure 1.

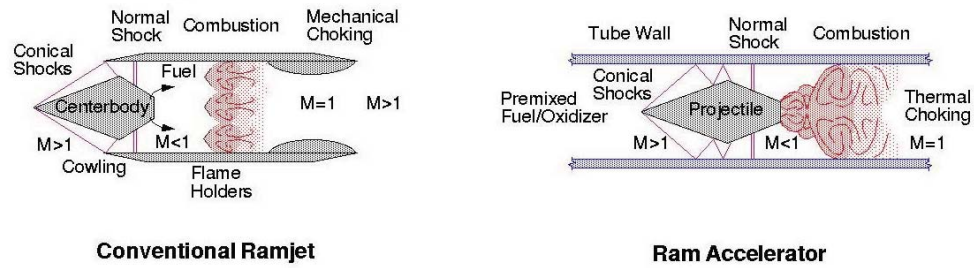


Figure 1: Ram accelerator vs ramjet

Since the ram accelerator projectile must travel supersonically, the system requires some type of pre-accelerator to provide an initial boost. Typically, a gas gun or powder gun is used to accelerate the projectile to 1 km/sec, or Mach 3, where ram acceleration can begin. By proper venting of the ram accelerator combustion products, the recoil can be completely eliminated, figure 2. Also, since the projectile is subcaliber, some mechanical means is required to stabilize the projectile in the tube. Either the projectile can have fins to keep it centered, or an axisymmetric projectile can ride on rails in the tube. The projectile is injected into the accelerator barrel

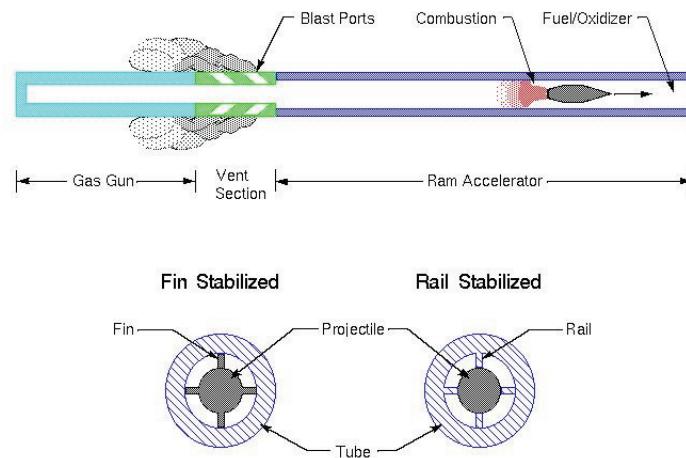


Figure 2: Ram accelerator launcher system

filled with the premixed propellants [2], [3], causing compression between the projectile and the barrel's walls. As the ram accelerator projectile compresses the fuel-air mixture, it is ignited and the combustion is stabilized at the base of the projectile. The resulting increase in pressure generates a thrust that accelerates projectiles to in-tube Mach numbers greater than 8. Thus, if propellant mixtures having a sound speed of 1000 m/s (e.g. fuel-rich  $H_2 - O_2$  mixtures) are used, muzzle velocities in excess of 8000 m/s are possible.

To span a wide velocity range in a typical ram accelerator system, multiple stages with propellants having different sound speeds are used to maintain high performance. Thin membranes that are easily punctured by the ram accelerator projectile are used to isolate the propellant stages. Each section is filled with a different fuel-air mixture chosen so that later sections have higher speeds of sound. As such, the ram can be maintained at optimal speeds of Mach 3 to 5, relative to the mixture that it travels through, during its entire acceleration period. Ram accelerators optimized to use supersonic combustion modes can generate even higher velocities (Mach 6-8) due to the ability to combust fuel that is still moving at supersonic speed.

There are several propulsive modes in which the ram accelerator can operate, which are characterized by the relative projectile velocity with respect to the Chapman-Jouguet detonation velocity ( $V_{CJ}$ ) [4], [5], [6], [7]. In subdetonative velocity regime ( $V$  less than  $V_{CJ}$ ), the combustion occurs subsonically and is thermally choked in the full tube area behind the projectile, with the blunt base acting as a flame holder,

figure 3. This mode of operation works best in the Mach number range of 3 to 5. The thrust of the thermally choked modes decreases as the projectile reaches the CJ detonation velocity, where theoretically the thrust goes to zero. At superdetonative velocities ( $V$  greater than  $V_{CJ}$ ), the combustion has moved up onto the body and the energy release takes place entirely supersonically in the annular region between the projectile and tube wall [4], [8], [9] [6], [10], [11], [12], [13], [14], [15], [16]. The combustion could be an oblique detonation, shock induced combustion, boundary layer combustion, or a combination of these, figure 3. This mode is analogous to a scramjet or oblique detonation wave engine. Superdetonative operation can, in principle, accelerate projectiles to nearly three times the detonation velocity of hydrogen-oxygen propellant mixture, which corresponds to velocities in excess of 10Km/s. [4], [13], [14], [15], [17], [18].

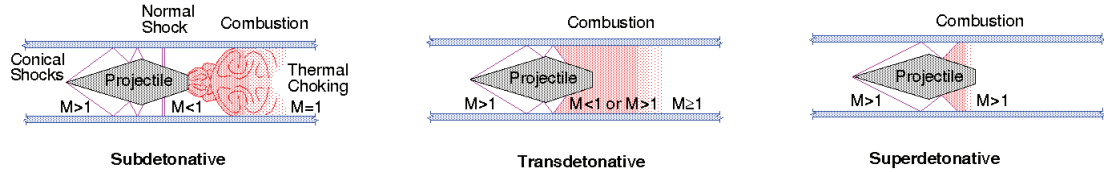


Figure 3: Ram accelerator combustion regimes

While theoretically the thermally choked mode is limited to values below the detonation velocity, experimentally it is observed that a projectile can accelerate from below to above the CJ detonation velocity in a single propellant mixture. This transition from thermally choked to superdetonative operation, called "transdetonative" [19], results from mixed mode combustion occurring on and behind the projectile in both subsonic and supersonic flow, figure 3.

Since the first proof of ram accelerator was demonstrated at the University of Washington [2], much has been learned about the phenomena that governs the ram accelerator. The ram accelerator has been the subject of research for many laboratories in the world, USA, France, Japan, China. The three major active facilities are the University of Washington (USA), the Institute of Saint-Louis-ISL(France) and the US Army Research Laboratory-ARL facility (USA).

At the University of Washington, Bruckner [5], [20][21], carried out experiments to examine the operation of the ram accelerator in different propulsion regimes using methane and ethylene based propellant mixtures in a 16 m long, 38-mm-bore ram accelerator. Projectiles of 45-90 g were accelerated to velocities up to 2650 m/s. The transdetonative propulsion regime was investigated by Burnham *et al* [1990] [19], a velocity of 2400 m/s was obtained by accelerating a 70 g projectiles mass through 16 m accelerator tube. Knowlen [22] presented new techniques for photographing projectiles in the ram accelerator. More experiments were carried out to investigate the regimes of heat release and Mach number in which the ram accelerator will operate [23]. Different propellant mixtures have been used in the experiments. Several distinct mechanisms have been identified which limit the peak velocity that can be reached in a particular propellant mixture. The experiments focus on the phenomena which determines how the unstart Mach number depends on propellant energetics. Variations in projectile materials have been used to experimentally investigate the unstart mechanisms in this chemistry regime. It was found that the nose cone material has a significant effect on the unstart Mach number and the comparison with the experiments confirms that Mach number and heat release are the primary variables that



determine ram accelerator performance. In 1996 Knowlen [24] conducted experiments investigating the superdetonative propulsive cycles using projectiles fabricated from aluminum and titanium alloys. Experiments have demonstrated that acceleration is possible at velocities greater than the Chapman-Jouguet (CJ) detonation speed of a gaseous propellant mixture and the projectile materials were found to play a significant role in these experiments. Elvander [25], [26] investigates methods for achieving high velocity operation for thermally choked operation. Experiments were performed with the reduced-mass projectile in methane/oxygen and methane/oxygen mixtures diluted with additional hydrogen or helium. An average of 38,000 g acceleration over 2 m and 33,000 g over 4 m was achieved. Bundy [27] investigated the ram accelerator at high fill pressure (greater than 5 MPa). It was found that the amplitude of the wall tube pressure data was found to be varying linearly with increasing fill pressures once the ram accelerator operation was established. Results show a gain of 500 m/s in just 3m of test section. More experiments have been carried out at high fill pressure, i.e  $P > 8.5 \text{ MPa}$  [28], pressure up to 20 MPa [29]. Results show that projectiles having throat of 29mm require a minimum entrance velocity of 1250 m/s, which is 100 m/s faster than that used for experiments at fill pressure below 7MPa. Projectiles with 25mm throat were successfully accelerated at fill pressure up to 15MPa with entrance velocity of 1300 m/s. Knowlen [30] conducted an experimental investigation of ram accelerator operational characteristics at fill pressures up to 20 MPa. Projectiles were injected at an entrance velocity of 1250 m/s, successfully ram accelerator operation has been achieved for 4 m in 20 MPa. Velocity gains greater than 1000 m/s were achieved and average accelerations of 46,000 g with 118 gm projectiles were attained. Bundy [31] carried out the same experiments at high fill pressure of 20

MPa in 38 mm bore ram accelerator. Projectiles of 23 mm throat diameter were injected at entrance velocity of 1250. A total velocity gain of 900 m/s and average acceleration of 42-46 Kgee have been achieved for projectiles of 106 -116 g in ram tube of 4 m. Knowlen [32], carried out an investigation to study the shock-induced-combustion ramjet propulsive cycle in the 38-mm-bore ram accelerator facility. The projectiles made of titanium-alloy were injected in ram accelerator tube filled with methan/ethane propellant at Mach numbers greater than 5.5. Positive acceleration was observed in the Mach range of 5.5-7 for distances of up to 6 meters.

The ram accelerator at ISL includes two versions RAMAC90, and RAMC30 (projectile calibre 90 mm and 30 mm) [33], [34], [35] [36] [37]. The first positive results were obtained at ISL was in 1992. These installations have been modified allowing enhanced RAMAC entrance performances, i.e the launching of higher masses at the same initial velocities. Experiments were conduct by Giraud in 1992, [33], on two smooth-bore experiments tools 30 and 90 mm, respectively, to study the scaling effects for whole ram process. In this work, he highlights the effect of the diffuser geometry on the RAMAC performances, i.e the importance of the profile, size and the number of the guiding fins, and also the effect of the Mach number, the reproducibility of the RAMAC process by using multi stage ram to obtain higher velocities. Later on, in 1993,[34] experiments were carried out to study the transition in combustion process of the sbudetonative combustion mode to superdetonative mode. More experiments [38] were focused on the initiation process and the effect of the sabot in successful RAMAC operations. In 1998, Giraud [39] conducted an experiment to investigated the subdetonative combustion mode, the shape and the size of the fins was addressed and

experiments were carried out at fill pressures ranging from 3 to 4,5 MPa. The ignition was achieved without any external devices. In 1999 Legendre [40], at the same laboratory conducted a series of experiments to determine the operational conditions to accelerate a 90 mm-caliber projectile with mass of 1.5Kg to a velocity of 3Km/s. The successful operation was achieved for a maximum velocity of 1985 m/s with projectile caliber of 90 mm and 1.34 kg mass. More experiments were carried out to enhance the RAMAC performance in subdetonative propulsion mode [41] and to determine the experimental conditions required to accelerate a projectile in the mass range from 1.5 to 2 kg up to a muzzle velocity of 3km/s while keeping the maximum acceleration below 40,000 g. Different material configurations for the projectile afterbody have been investigated, and new configuration was adopted which relies on a short magnesium part fitted to the base of an aluminum afterbody. This configuration (denoted as semi-combustible) is designed so that magnesium particles are steadily injected and burnt-out within the combustion zone at the base, therefore providing an additional heat release and consequently a significantly greater forward thrust. Experimental results achieved in both 30 and 90 mm along a 300-caliber-long ram-section and using up to three different gaseous mixtures are presented. For a given semi-combustible projectile and an injection velocity into the ram-section of 1380 m/s, a maximum muzzle velocity of 2380 m/s has been achieved in RAMAC 30-II and 2180 m/s in RAMAC 90, the initial projectile mass being 69 g and 1608 g respectively. Legendre [42] conducted an experiment to investigate the detonation characteristics (detonability limits and detonation velocities) of methane-oxygen-helium mixtures at initial pressures of up to 5 MPa in a 90 mm caliber, 11.7 m long smooth-bore detonation

tube. Stoichiometric as well as fuel-rich mixtures were investigated in order to provide performance data for ram accelerator applications. This investigation enabled to determine of the upper detonable area of these dense ternary mixtures under the present experimental conditions.

Henner in 1998 [43], [44], [45] investigates the scale effects on the ram accelerator and provided a good data for the shape and the characteristics of the sabot and their effects on the successful operation on the ram accelerator. The experiments were conducted in a 30-mm as well as in 90-mm facility. Major differences were observed in the initiation process. The results show that the diameter ratio is not the only factor, and the design of the sabot turn out to provide a major contribution in this process. The data derived from experiments show that the initiation of the mixture is related to the coupling of the sabot and the projectile in order to achieve the appropriate conditions of the pressure and temperature at the base of the projectile.

The ram accelerator at the U.S Ballistic Research Laboratory explores the scaling of the ram accelerator to 120mm diameter. The first successful experiments operation of the 120mm ram was in 1991 conducted by Kruczynski, [46], [47], [48], [49], [50], [51]. The experiments were carried out for fuel pressures as high as 10MPa. [52].A new method about flow visualization techniques for transient and steady combustion in the ram accelerator was demonstrated, [53]. It indicates intense combustion around the projectile until the obturator is far downstream of the projectile; stable combustion is then established on the projectile mid- and aft-sections. These observations suggest that reduction in the number of unstarts, as well as potential performance

increases, may be achieved by control of the obturator location relative to the projectile during the starting process. More experiments were carried out and they focused on investigating the starting process at low velocities around 750 m/s, [54] the results show that the combustion could happen and be stabilized, and the projectile was able to accelerate up to 1150m/s, where at this velocity the projectile can make a transition into propellant having high sound speeds. Further investigations were carried out to study the starting dynamics at high fill pressures, [54], [55]

In addition to the experiments outlines here, considerable work has been done in numerical modeling of ram accelerator performance. First a steady state one-dimensional model was developed by Carl Knowlen in 1991,[11], to predict the performance of the projectile in the thermally choked combustion mode. The main idea of this modeling is to describe the effects of the flow around the projectile as a global process between the state of the propellant entering the control volume and the state of the thermally choked exit flow. This modeling is based on the set of one-dimensional conservation equations [11], [56]. The flow properties are modified through a control volume by addition of chemical heat release and the rate of change of axial momentum. The velocity and acceleration histories predicted by the quasi-steady analysis for the thermally choked ram accelerator cycle are shown to correlate well with experiments [11] [56]. Theoretical prediction for the pressure at the thermal choking point match the tube wall pressure data, collected from behind the combustion zone at the projectile base, up to the C-J velocity of the propellant mixture. Good agreement between theory and experiments in the thermally choked propulsive cycle were obtained based on the quasi-steady model using ideal gas assumption. At the high level of pressure

that is encountered during the ram accelerator process, this assumption cannot be regarded as adequate. Thus, a more appropriate equation of state (EOS) should be used instead. It was found that using the ideal gas equation of state is no longer applicable above 1 PMa, where often it under-predicts the experimental thrust and velocity profiles at fill pressures greater than 1MPa. Bauer [57] presents the real gas effects on the analysis of ram accelerator performance. The same conservation equations are applied, and depending upon the level of pressure, several equations of state are available for dense gaseous energetic materials [58]. The virial type of EOS can be more or less sophisticated, depending upon the extent of complexity of the intermolecular modeling, and turns out to be totally appropriate for most gaseous explosive mixtures that have been investigated at moderate initial pressures, i.e., less than 10 MPa. Calculations were carried out to determine the performance of the ram accelerator in the thermally choked propulsion cycle using Boltzmann equation of state. It is based on very simplified molecular interactions, which makes it relatively easy to use in calculations [58]. Moreover, the energetic EOS needs to be taken into account. This concerns all the calorimetric coefficients, as well as the thermodynamic parameters, which can no longer be expressed as a function of temperature only. The higher the pressure level, the more sophisticated these corrections become, but the main relationships that account for real gas effects are basically the same. These include the use of a general form of analytical operators applied to correct the thermodynamic functions and coefficients. The equations governing the one-dimensional model were taken as a basis for the real gas corrections and were solved analytically.

A complete set of equations involving the real gas effects that can be used in the

ram accelerator modeling were presented by Bauer, [57]. From the calculation, it turns out that using Boltzmann equation of state, the projectile velocity and acceleration histories are in much better agreement with experimental data up to the CJ detonation velocity. Thrust calculations of the thermally choked ram accelerator propulsive mode based on quasi-steady, one-dimensional modeling of the flow process have been quite successful in predicting the experimental velocity-distance profile when real gas corrections are applied to the combustion products of propellants at initial fill pressures up to 8 MPa [59]. A further refinement of the modeling takes into account real gas corrections for the initial state at higher fill pressures. It turns out that the Redlich-Kwong equation of state accurately determines the thermodynamic properties of the unreacted propellant for fill pressures up to at least 20 MPa. Using this equation of state for the calculation of the sound speed for a typical CH<sub>4</sub>/O<sub>2</sub>/N<sub>2</sub> propellant provides a 15% higher value at 20 MPa than that predicted for an ideal gas; this increase significantly affects the operating characteristics of the ram accelerator at a given velocity. The corresponding thrust maximum increases by 30 %. This corrected theory is most appropriate under conditions of high pressure operation at relatively low acceleration levels; i. e., less than 10 000 g. A revision of the conservation equations to account for unsteady flow effects was conducted[60]. Unsteady state model was developed to consider the mass of the projectile into the modeling. The corresponding predicted thrust as a function of Mach number is significantly less than that derived from the quasi-steady model. By using a virial-type equation of state for the combustion products, a better agreement with experimental data was obtained. More theoretical work was carried out to determine the parameters that allow successful operation of ram accelerator in dense, gaseous propellants [61], for

this purpose experiments were conducted at Washington University at fill pressures up to 20 MPa. Results show that at high acceleration levels that typically arise from operating the ram accelerator at elevated pressure, however, the quasi-steady one-dimensional model overpredicts the experimental acceleration when a real-gas equation of state (EOS) is used. A revision to the quasi-steady model was made by Bundy et al [31], to account for projectile acceleration on the thrust, the finite length of the combustion zone, and the dependency of the real-gas heat release on the in-tube Mach number.

Considerable activity has also occurred in computational modeling of reactive flow in the ram accelerator. Yungster presents a numerical scheme for calculating hypersonic flows involving shock-induced combustion in the ram accelerator [62], [14]. The performance characteristics of the ram accelerator were investigated in the superdetonative velocity range of 5.0 to 10.0 km/s. The analysis was carried out using a TVD numerical scheme that includes nonequilibrium chemistry, real gas effects, and the flow were assumed to be inviscid. More work has been done to study the shock wave/boundary layer interactions [63], [15]. A detailed chemical reaction mechanism was used for Hydrogen/air mixtures based on 7 species and 8 steps reaction. Results show that the shock wave induces combustion in the boundary layer, which then propagate downstream. New results for considering the viscous effect on the modeling show that the shock-induced combustion always started in the boundary layer [64]. Stable, and unstable combustion process were identified based on the inflow conditions.

Different reaction mechanisms for methane/air mixtures based on (19 reacting species



and 52 steps reaction) [65], [66], and hydrogen/air mixtures based on (9 species and 19 steps reaction)[67] were used to simulate the reactive flow in the ram accelerator. Nusca conducted a computational fluid dynamics simulation to study the reactive flow field around 120 mm projectile, in the thermally choked combustion mode [68], [69] [70], [71] Detailed chemical reaction mechanisms were used for methane/air premixed gases originally developed by Westbrook [72]. More work has been done to study the effect of the sabot in the successful starting combustion process in the ram accelerator [73], [74], the temporal developments of shock-induced combustion [75]. and the fins effects on the three dimensional flow field associated with the ram accelerator projectile [76], [77]. Due to the three-dimensional nature of the projectile flow field as affected by the projectile fins, various combustion phenomena, and the phenomenon of projectile canting were observed. It was found that the flow field is highly influenced by the projectile fins, [78], [79]. In order to show the influence of the geometry of the fins on the ram accelerator performances, a numerical simulation of the flow characteristics around the projectile with and without fins was undertaken [80],[43], [81]. Moreover, a better knowledge of the gasdynamics of the flow was expected in order to improve the ram accelerator operations by reducing the risk of unstart. A series of calculations were conducted using the 3D numerical code TascFlow from AEA Technology. Different types of fins, i.e., various shapes and numbers were studied. The characteristics of the flow in terms of temperature, pressure and Mach number distributions were studied. The data show a drastic role of the fin geometry on the maximum temperature of the flow. Moreover, the elevated values of the stagnation temperature at the leading edge of the fins, namely up to

1600 K at Mach 5, may explain the combustion that locally takes place and eventually leads to an unstart. Further modeling shows that the flow field in the ram accelerator is highly transient and the combustion process is strongly affected by the projectile acceleration [82], [83]. During the acceleration of the projectile, the ablation phenomenon was observed, and has been investigated by several researchers [84], [85], [86]. It was found that the projectile unstart could happen due to the increase in clearance between the fins and the accelerator tube. Also the aerothermal load on the projectile is small when the propulsion mode is subdetonative. In 1996 Peterson, presents a new detailed chemical reaction mechanism [87] which was used by Nusca to simulate the reactive flow at high fill pressures ram accelerator [88], [89]. Further simulations [90] solved steady Navier-Stokes equations coupled with detailed chemical kinetics of 22 species and 32 steps reaction for methane/oxygen propellant, this mechanism was derived from Stanford RAMEC chemical mechanism. The second part of the modeling was to investigate the acceleration process by coupling the CFD calculation with an interior ballistics code. The simulations were carried out for a 120 mm ram accelerator projectile. More investigations were done to analyze the starting process and illustrate the importance of obturator in achieving a successful starting of the ram accelerator process, [91], [92]. Further work has been done to investigate the temporal evolution of the combustion process that is established during projectile transition from the launch tube into the ram accelerator section, [93], containing a premixed gas of hydrogen, oxygen and argon. The hydrogen-oxygen-argon chemistry is modeled with a nine-species, 19-step reaction mechanism. Results show that the combustion in the boundary layer enhances its separation, ultimately resulting in unstart.

Choi [94], [95], [96], [97] carried out a numerical study to investigate the ignition and the detonation initiation process in a scram accelerator operating in a superdetonative mode. The projectile was injected at velocity of 2500 m/s in ram accelerator tube filled with hydrogen/oxygen mixture, and the Nitrogen was used as diluent, by changing the amount of the nitrogen in the mixture to examine combustion characteristics and ram-accelerator operation limits. The results identify the combustion characteristics of the operational failures at lower and upper dilution limits that have been observed in experiments. Extensive studies were carried out using a new chemical kinetics mechanisms based on 3 and 9 steps reaction for methane/air gas mixture, [98] to simulate the reacting in-bore flowfield for a 90-mm ram-accelerator projectile propulsion system. Results show that the choice of chemical kinetics mechanism is of critical importance in achieving an accurate numerical simulation of the ram accelerator.

At the Freiburg conference in Germany 2004, Giraud [99] presented a paper summarizing nearly two decades of experiments and modeling of the ram accelerator.

Our research program focuses on predicting the ram accelerator performances in the thermally choked propulsive mode. Two approaches have been applied; the first is to develop a one-dimensional computer program which includes the quasi-steady and unsteady assumption. This program incorporates the following equations of state: ideal gas, Boltzmann, Percus-Yevick, and Becker-Kistiakowsky-Wilson. The second

approach is to use the Computational fluid dynamics solutions of the Reynolds Averaged Navier-Stokes equations to numerically predict the thrust in the thermally choked propulsive mode. The current research program will be organized as follows: chapter 1 is devoted to presenting in detail the thermally choked unsteady one-dimensional model. The general calculation procedure will be presented. The predicted ram accelerator performance from the unsteady one-dimensional modeling also using quasi-steady modeling will be validated against a key experimental data. The modeling will include different real gas equations of state, in addition it does investigate the performance of the ram accelerator at high fill pressures. The effect of the projectile acceleration will be presented and the choice of the control volume length will be discussed. In chapter 2, we will present the conservation equations needed for reacting flows have and show the main differences between these equations and the usual Navier-Stokes equations for non reacting cases. The elementary concepts of turbulence and flame/turbulence interaction including the averaging and filtering procedures are presented in chapter 3 details about the two equations turbulence model  $k - \varepsilon$  and  $k - \omega$  have been presented as both are used by the SST turbulence model, also the Eddy break Up (EBU) for the turbulent combustion is presented to give a brief history for the development of the Eddy Dissipation Model. This chapter presents some of the theories that have been put in place to address these issues. Chapter 4 deals with numerical modeling procedure, presenting the geometry, describe the computational procedure, and determining the turbulence parameters. Different chemical kinetic mechanisms will be presented and the approach for including thermal radiation is also presented. In chapter 5, we will present the results from CFD modeling. The choice of the chemical kinetics mechanism will be discussed as

well as the effect of the thermal radiation in the modeling. Results on pressure over a range of in-coming velocities will be compared to the experimental data, and the thrust will be predicted as well. After having investigated the variation of the control volume length over a range of incoming velocities from CFD modeling.

A further refinement on the unsteady one-dimensional model is proposed in chapter 6. Calculations will be carried out to predict the ram accelerator performance using various approaches for the control volume, as well as using the CFD findings for  $L_{CV}$ , the results will be compared with the experimental data. In chapter 7 we will summarize this dissertation research, present the corresponding conclusions and recommend future research in this area. More details about the equations of state used in the present work as well as the quasi-steady one-dimensional model are presented in appendix A, and the geometry of the ram accelerator projectile used for the CFD calculation is presented in appendix B. Appendix C outlines the convergence history for the velocity, pressure and the species mass fraction. The steady state solution is shown by different monitoring points located in different locations in the computational domain.

# Chapter 1

## Quasi-steady and unsteady one-dimensional modeling of ram accelerator in thermally choked propulsion mode

### 1.1 Introduction

The analysis of the ram accelerator [1] performance based on the one-dimensional model of the flow that propels the projectile was achieved by applying the conservation equations to a control volume traveling with the projectile. The performance of the ram accelerator can be obtained by using both quasi-steady and unsteady assumptions. Results show that the predicted thrust and acceleration based on the quasi-steady model are much greater than that observed in experiments due to the fact the quasi-steady model does not take into account the projectile mass in the modeling.

We developed a one-dimensional computer code called "TARAM" to predict the

performance of the ram accelerator in the thermally choked propulsive mode. The computer code is able to ram accelerator performance in both quasi-steady and unsteady flow assumptions. The current research code incorporates the following equations of state: ideal gas, Boltzmann, Percus-Yevick, and Becker-Kistiakowsky-Wilson (BKW). The code also includes the compressibility effects on the calculation. The results from the calculations will be compared against key experimental data from a representative experiment at the University of Washington 38-mm-bore facility. In this chapter we will present the unsteady model, details about the quasi-steady are given in appendix A.

## 1.2 Unsteady 1-D conservation equations

The predicted acceleration performance of the ram accelerator under conditions where the projectile is experiencing very high accelerations; i.e., greater than 30,000 g, based on the quasi-steady model, is much greater than that observed in experiments. This discrepancy is attributed to the increase of mass of the propellant accumulating in the control volume, such that it approaches the mass of the projectile itself [60]. The basis of this analysis is to describe the effects of the flow around the projectile as a global process between the state of the incoming flow and thermally choked exit flow [60]. The model is based on the standard set of one dimensional conservation equations [31]. The flow properties are modified by accounting for the rate of accumulation of mass, momentum, and energy within the control volume.

The conservation equations for the mass, energy, and momentum are solved for a propellant entering and leaving the control volume of length  $L_{CV}$  as shown in figure

(1.1).

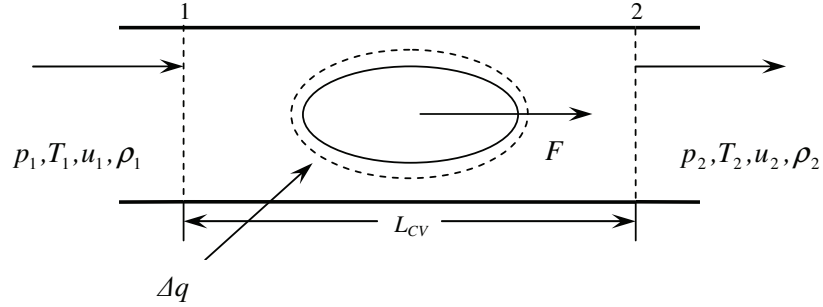


Figure 1.1: Schematic of the one-dimensional control volume

- Continuity:

$$\frac{d}{dt} \int_{CV} \frac{dv}{v} + \frac{u_2}{v_2} A - \frac{u_1}{v_1} A = 0 \quad (1.2.1)$$

- Momentum:

$$\frac{d}{dt} \int_{CV} \frac{dv}{v} + A(p_2 + \frac{u_2^2}{v_2}) - A(p_1 + \frac{u_1^2}{v_1}) - \int_{CV} a_p \frac{dv}{v} - F = 0 \quad (1.2.2)$$

- Energy:

$$\frac{d}{dt} \int_{CV} (e + \frac{u_2}{2}) \frac{dv}{v} + A \frac{u_2}{v_2} (h_{f_2} + h_2 + \frac{u_2^2}{2}) - A \frac{u_1}{v_1} (h_{f_1} + h_1 + \frac{u_1^2}{2}) - \int_{CV} u a_p \frac{dv}{v} = 0 \quad (1.2.3)$$

where  $u$  is the velocity,  $e$  is the specific internal energy,  $v_i$  is specific volume,  $h$  is enthalpy,  $h_f$  is enthalpy of formation at 0K,  $p$  is pressure,  $A$  is tube cross sectional area,  $a_p$  is the acceleration of the projectile and  $t$  is time. A further analysis of all the terms in these equations yields a more readily applicable set of equations in the following form:



- Continuity:

$$\frac{Aa_p L_{CV}}{u_1 v_1} + \frac{u_2}{v_2} A - \frac{u_1}{v_1} A = 0 \quad (1.2.4)$$

- Momentum:

$$Aa_p \frac{L_{CV}}{v_1} + A(p_2 + \frac{u_2^2}{v_2}) - A(p_1 + \frac{u_1^2}{v_1}) - m_p a_p = 0 \quad (1.2.5)$$

- Energy:

$$\frac{7}{2} \frac{u_1}{v_1} Aa_p L_{CV} + A \frac{u_2}{v_2} (h_2 + \frac{u_2^2}{2}) - A \frac{u_1}{v_1} (h_1 + \frac{u_1^2}{2} + \Delta q) = 0 \quad (1.2.6)$$

With:

$$Q = \frac{\Delta q}{cp_1 T_1}; \quad I = \frac{F}{p_1 A}; \quad P = \frac{p_2}{p_1}; \quad V = \frac{v_2}{v_1} \quad (1.2.7)$$

where  $c_p$  is the constant pressure specific heat capacity and  $\Delta q = h_{f1} - h_{f2}$ . These terms denote the non dimensional heat release ( $Q$ ), non-dimensional thrust ( $I$ ), and the ratios of pressure ( $P$ ) and specific volume ( $V$ ) between the final and initial states, respectively. The variable  $m_p$  denotes the mass of the projectile and  $T$  is the temperature. After some algebraic combinations of these relationships, specifying the state to be at the sonic condition introducing a real gas EoS, namely  $pv/RT = \sigma(v, T)$  [60]

$$P = \frac{\sigma_2}{\sigma_1} (M_1 \sqrt{\frac{\gamma_1 R_2}{\gamma_2 R_1}} - \frac{L_{CV} a_p}{R_1 T_1 M_1} \sqrt{\frac{R_2}{\gamma_1 \Gamma_2 R_1}}) \sqrt{\frac{T_2}{T_1}} \quad (1.2.8)$$

with

$$\frac{T_2}{T_1} = \frac{cp_1 (\eta_1 + \frac{M_1 \gamma_1 R_1}{2cp_1} + Q) - \frac{7}{2} \frac{L_{CV} a_p}{2cp_1 T_1}}{cp_2 (\eta_2 + \frac{\Gamma_2 R_2}{2cp_2}) (1 - \frac{L_{CV} a_p}{R_1 T_1 \gamma_1 M_1^2})} \quad (1.2.9)$$

$\Gamma$ ,  $h$ , and  $R$ , are the adiabatic gamma, the caloric imperfection term ( $\eta_1 = h_1/cp_1 T_1$ ), and the gas constant, respectively. The momentum equation becomes:

$$I = \frac{m_p a_p}{Ap_1} = \frac{L_{CV} a_p}{R_1 T_1} + \frac{\sigma_2}{\sigma_1} (M_1 \sqrt{\frac{\gamma_1 R_2}{\Gamma_2 R_1}} - \frac{L_{CV} a_p}{R_1 T_1 M_1} \sqrt{\frac{R_2}{\gamma_1 \Gamma_2 R_1}}) \sqrt{\frac{T_2}{T_1}} (1 + \frac{\Gamma_2}{\sigma_2}) - (1 + M_1^2 \frac{\gamma_1}{\sigma_1}) \quad (1.2.10)$$

for steady state case,  $a_p = 0$ , and  $\sigma_1 = 1$ :

$$I = \sigma_2 M_1 \sqrt{\frac{\gamma_1 R_2}{\Gamma_2 R_1}} \sqrt{\frac{T_2}{T_1}} \left(1 + \frac{\Gamma_2}{\sigma_2}\right) - (1 + M_1^2 \gamma_1) \quad (1.2.11)$$

Equations (1.0.8), (1.0.9) and (1.0.10) can be written in form:

$$P = \frac{\sigma_2}{\sigma_1} \left[ M_1 \sqrt{\frac{\gamma_1 R_2}{\Gamma_2 R_1}} - f_3(\alpha) \right] \sqrt{\frac{T_2}{T_1}} \quad (1.2.12)$$

$$\frac{T_2}{T_1} = \frac{cp_1 (\eta_1 + \frac{M_1 \gamma_1 R_1}{2cp_1} + Q) - f_1(\alpha)}{cp_2 (\eta_2 + \frac{\Gamma_2 R_2}{2cp_2}) [1 - f_2(\alpha)]} \quad (1.2.13)$$

$$I = f_4(\alpha) \frac{\sigma_2}{\sigma_1} \left[ M_1 \sqrt{\frac{\gamma_1 R_2}{\Gamma_2 R_1}} - f_3(\alpha) \right] \sqrt{\frac{T_2}{T_1}} \left(1 + \frac{\Gamma_2}{\sigma_2}\right) - (1 + M_1^2 \frac{\gamma_1}{\sigma_1}) \quad (1.2.14)$$

with

$$\begin{aligned} f_1(\alpha) &= \frac{7}{2} \frac{\alpha}{cp_1 T_1}; \\ f_2(\alpha) &= \frac{\alpha}{R_1 \gamma_1 T_1 M_1^2}; \\ f_3(\alpha) &= \frac{\alpha}{R_1 T_1 M_1} \sqrt{\frac{\alpha}{R_1 \gamma_1 \Gamma_2}}; \\ f_4(\alpha) &= \frac{\alpha}{R_1 T_1}; \end{aligned}$$

with

$$\alpha = L_{CV} a_p.$$

The preceding equations show that the non-dimensional thrust is direct function of the projectile acceleration ( $a_p$ ) and the control volume length ( $L_{CV}$ ). The calculations were based on control volume ( $L_{CV} = 2L_p$ ). The evidence of this value is based on luminosity and pressure records showing that the termination of the combustion zone occurs approximately one projectile length behind the projectile base [5]. This aspect will be discussed more extensively in chapter [6].

The following equation will be used to calculate the projectile acceleration:

$$\frac{m_p a_p}{A p_1} - \frac{L_{CV} a_p}{R_1 T_1} + \frac{\sigma_2}{\sigma_1} \left( M_1 \sqrt{\frac{\gamma_1 R_2}{\Gamma_2 R_1}} - \frac{L_{CV} a_p}{R_1 T_1 M_1} \sqrt{\frac{R_2}{\gamma_1 \Gamma_2 R_1}} \right) \sqrt{\frac{T_2}{T_1}} \left( 1 + \frac{\Gamma_2}{\sigma_2} \right) - \left( 1 + M_1^2 \frac{\gamma_1}{\sigma_1} \right) = 0 \quad (1.2.16)$$

### 1.3 Calculation procedure

A computer program called TARAM was developed to predict the ram accelerator performance in the thermally choked propulsive mode. Quasi-steady and unsteady assumptions are considered in the modeling. figure 1.2 and figure 1.3 presents the general algorithm for the quasi-steady and unsteady assumptions consecutively. First, initial data is required for the Pressure ( $P_1$ ), temperature ( $T_1$ ) and Mach number ( $M_1$ ). From the theory of the thermally choked propulsive mode, the Mach number at the final state is ( $M_2 = 1$ ). The thermodynamic data will be determined at the initial state and at the finale state based on the choice of the EoS, as well as the calculation of the equilibrium composition. Once all the properties of the final state are determined, the ram accelerator performance will be calculated.

The program TARAM calculates the real gas effects for each EoS by changing the way  $\sigma$  is computed and keeping all other calculations consistent [57]. TARAM is capable of using either an ideal gas, Redlich-Kwong Boltzmann, Percus-Yevick, or BKW equation of state [100]. These equations of state were validated with experimental Chapman-Jouguet detonation speeds (CJ speeds) and ram accelerator thrust and velocity profiles.

## 1.4 Comparison with experimental data

The first validation compared computed CJ speeds for various gas mixtures at different fill pressure with experimental values, Bauer et al. [101] [102]. The experiments were performed at the University of Washington for different gas mixtures. The results listed in table (1.1), show that the increased CJ speeds predicted by the inclusion of the real gas effects at high pressures, confirms that the ideal gas solution matches the experimental values at low pressures.

Table 1.1: Computed and experimental Chapman-Jouguet speed

Press	Mixture	Ideal	Boltz	P-Y	Exp
MPa		(m/s)	(m/s)	(m/s)	(m/s)
20	$0.99CH_4 + 2O_2 + 3.9N_2$	2090	2812	2681	2625 <sup>†</sup>
10	$0.99CH_4 + 2O_2 + 3.9N_2$	2077	2415	2358	2346 <sup>†</sup>
5	$2.95CH_4 + 2O_2 + 5.7N_2$	1670	1843	1795	1850 <sup>‡</sup>
2.4	$2.8CH_4 + 2O_2 + 5.7N_2$	1685	1765	1744	1770 <sup>‡</sup>
0.61	$CH_4 + 2O_2 + 7.52N_2$	1831	1849	1846	1835 <sup>‡</sup>

<sup>†</sup> Bauer et al. 1991[101]

<sup>‡</sup> Bauer et al. 1996[102]

These cases were run to ensure that all real gas models produce results similar to the ideal gas values at lower pressure as at high pressure there will be the compressibility effects [59] which will be discussed later in section (1.5). As expected the calculations are nearly identical at lower pressures with only a 0.2% difference among the values for the 0.6 MPa case. The ideal gas equation of state performs adequately for initial fill pressures below 1 MPa, as the initial pressure is raised, the ideal gas speed drops significantly below the experimental values, having a 4, 8% error at 2.4MPa and 9.7% error at 5 MPa.

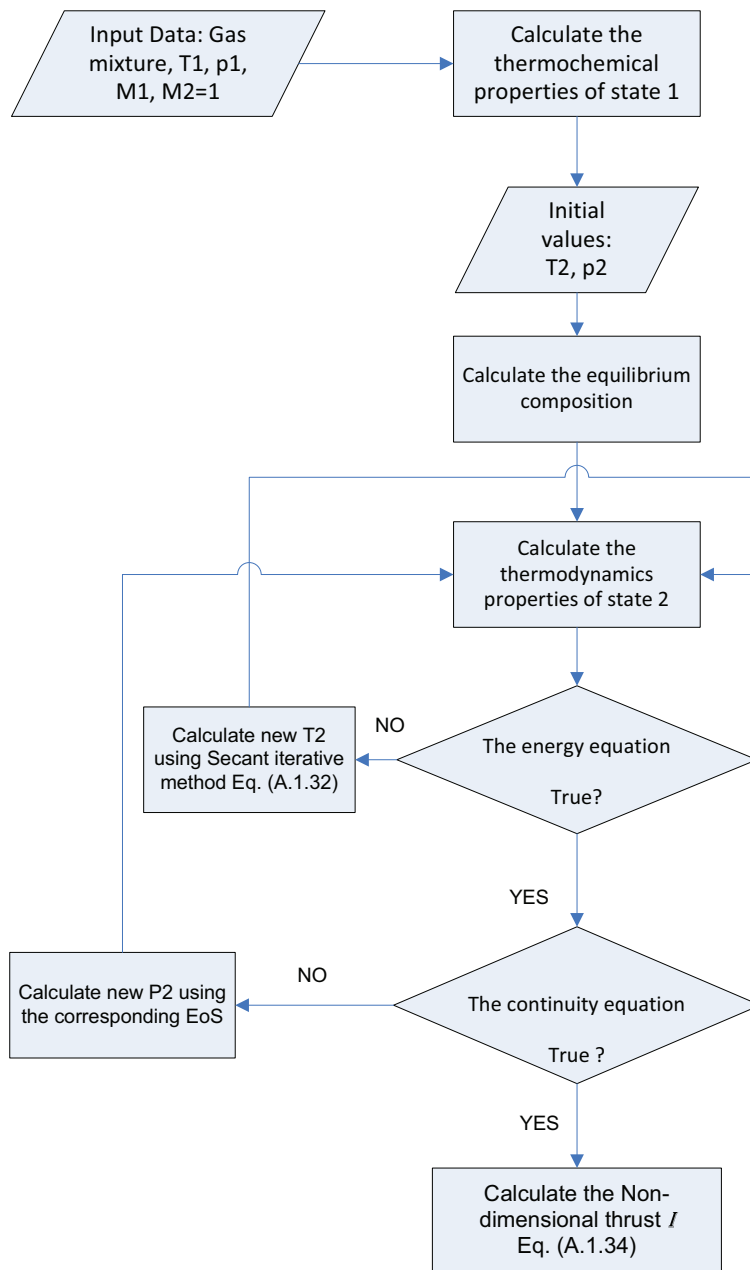


Figure 1.2: Algorithm for quasi-steady calculation

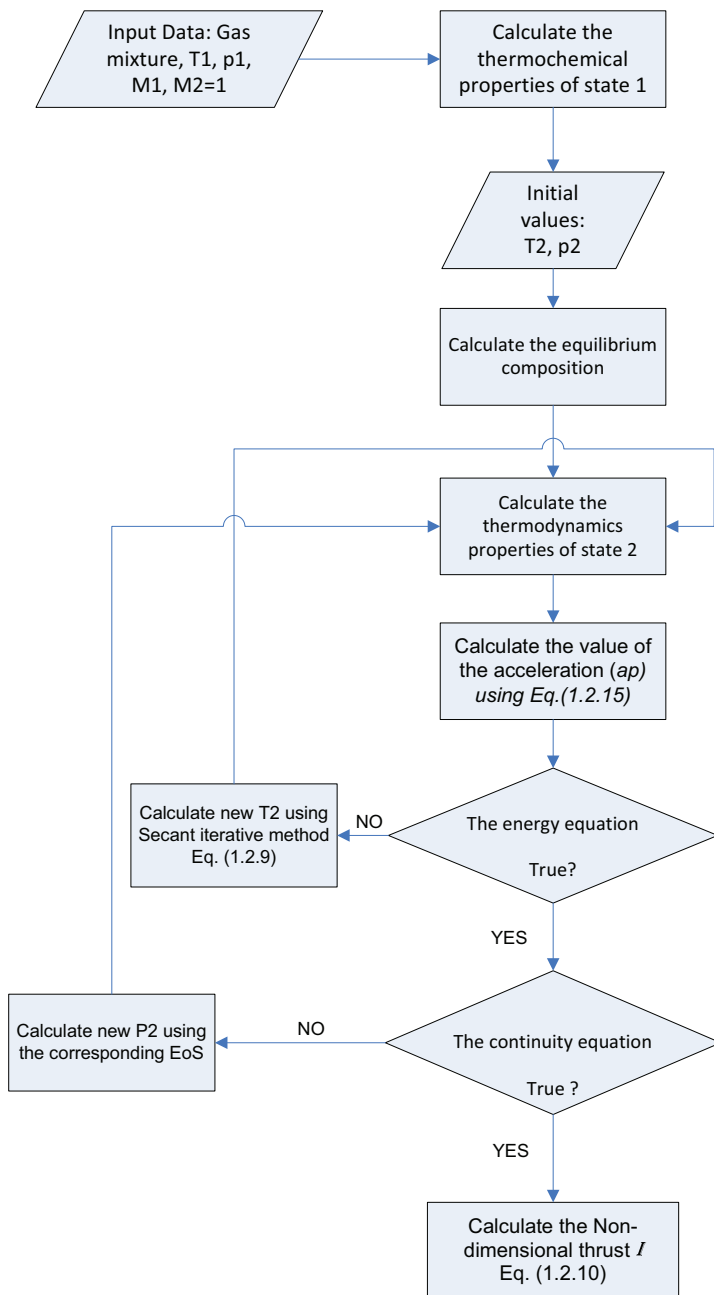


Figure 1.3: Algorithm for unsteady calculation

These errors become even larger at higher fill pressures with errors of 11.5% and 20% at 10 and 20 MPa respectively. The Boltzmann EoS performed well over the entire range of pressure and mixtures, but had an error less than 0.8% for pressures up to 5 MPa, and errors of 2.9% and 7% at 10 and 20 MPa respectively. The Percus-Yevick EoS performed well at high pressures compared to Boltzmann and Ideal gas EoS. It has an error about 2.1% at pressure initial of 20 MPa and 0.5% at 10 MPa, but the CJ speeds are higher at lower pressures, an error of 3% at 5 MPa and 1.5% at 2.4 MPa.

The experimental data used for the following theoretical comparison were those from representative 5 MPa fill pressure experiments conducted at the ram accelerator facility of University of Washington. The second step is to compare the calculated non dimensional thrust and velocity profiles with experimental results. The experimental data used here were from a representative 5.15 MPa fill pressure experiment conducted at the ram accelerator facility of University of Washington. Note that this experimental data is used for the first time here. The selected propellant mixture is  $2.95CH_4 + 2O_2 + 5.7N_2$ . The experiment was conducted with a 109 g projectile. The entrance velocity for this experiment was 1060 m/s; however, starting transients resulted in a brief delay before the thermally choked ram accelerator mode was fully established. Thus the calculations only compared the performance of the ram accelerator after the projectile had attained a velocity of 1240 m/s. The experimental thrust and velocity profiles were determined from time-distance data, the predicted non-dimensional thrust was evaluated by using different equations of state.

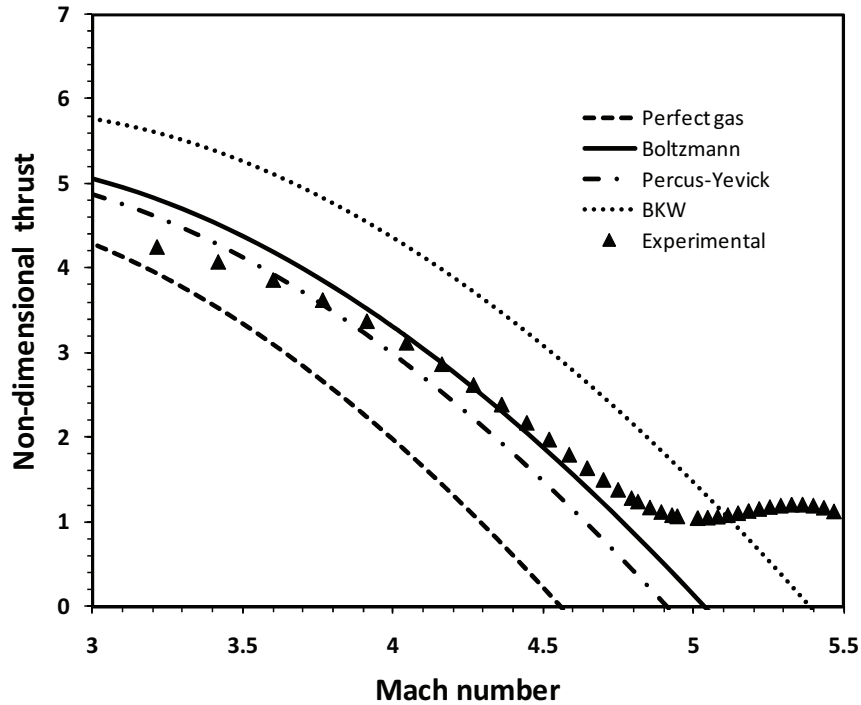


Figure 1.4: Non-dimensional Thrust-Mach plot for  $2.95CH_4 + 2O_2 + 5.7N_2$  propellant with quasi-steady modeling (Ideal gas EoS was used at station 1, and various real gas EoS at station 2.),  $P_1 = 5.15 \text{ MPa}$

figure (1.4) presents the non-dimensional thrust vs Mach number using quasi-steady modeling and figure (1.5) for the unsteady modeling. The non-dimensional thrust was compared against the experiments values. As expected the ideal gas EoS underpredicts the thrust, whereas the Boltzman and PY EoS modeled the thrust behavior within 3% over the Mach range of 3.2 to 4.6. The thrust predictions of the BKW EoS were 35% greater than experiment, implying that this EoS was not appropriate at this relative low fill pressure. figure (1.6) and figure (1.7) presents the predicted projectile thrust and velocity using different EoS. Again calculations using the Boltzman and PY EoS's predict experimental results much better than when applying the ideal gas



or BKW EoS's up to the point where the projectile velocity approaches the CJ speed of the propellant.

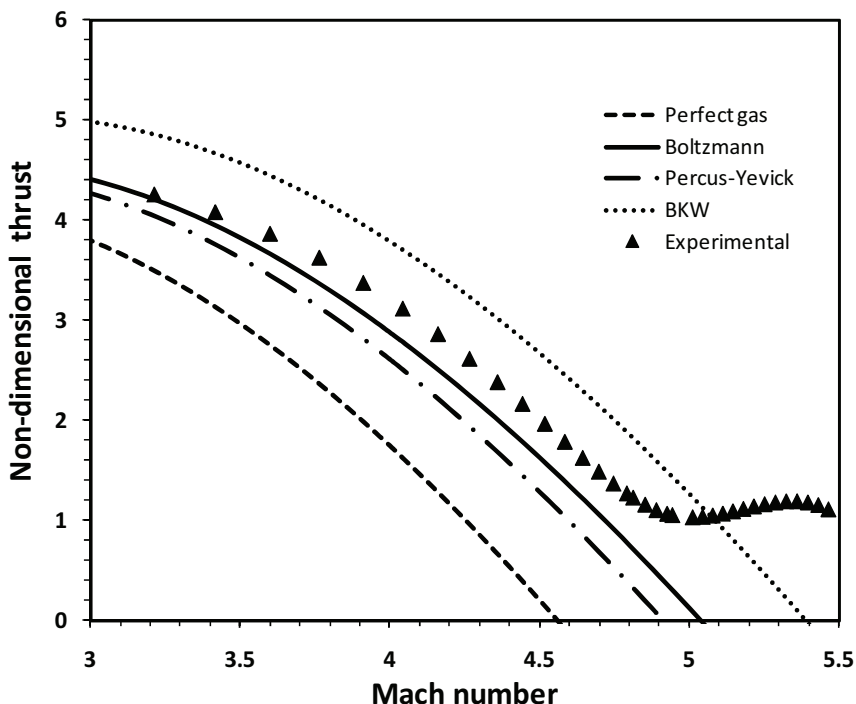


Figure 1.5: Non-dimensional Thrust-Mach plot for  $2.95CH_4 + 2O_2 + 5.7N_2$  propellant with unsteady modeling (Ideal gas EoS was used at station 1, and various real gas EoS at station 2.);  $L_{CV} = 2L_p$ ,  $P_1 = 5.15 MPa$

The experimental velocity in figure (1.6) and (1.7) deviates significantly from the theoretical calculation after about 7 m of travel. This region of enhanced velocity, and consequently thrust seen in figure (1.4) and (1.5), is due to the projectile making a transition from the thermally choked propulsive mode to the transdetonative mode [6]. This transition occurs when the projectile reaches approximately 90% of the Chapman-Jouguet speed. The current calculation attempts to predict the ram accelerator performance in the thermally choked regime, as the condition is  $M_2 = 1$  at station 2.

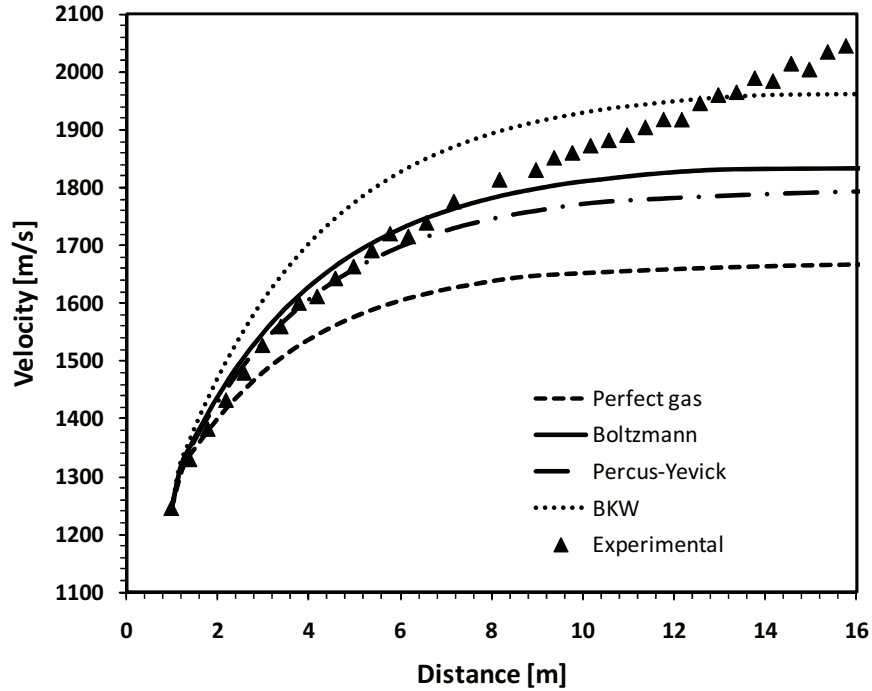


Figure 1.6: Velocity-distance plot for  $2.95CH_4 + 2O_2 + 5.7N_2$  propellant with quasi-steady modeling (Ideal gas EoS was used at station 1, and various real gas EoS at station 2.),  $P_1 = 5.15 \text{ MPa}$

figure (1.8) and figure (1.9) presents the ram accelerator performance using the quasi-steady assumption and unsteady assumption taking into account the real gas effects by using various real gas equations of state for the combustion products. This results show that the unsteady calculation predict an enhanced performance compared to quasi-steady calculation.

As shown in section (1.4) the steady state predict well the Chapman-Jouguet detonation speed (CJ) around 1 MPa, whereas few percent in difference was observed between 1MPa and 5MPa when using unsteady state assumption. Then difference of

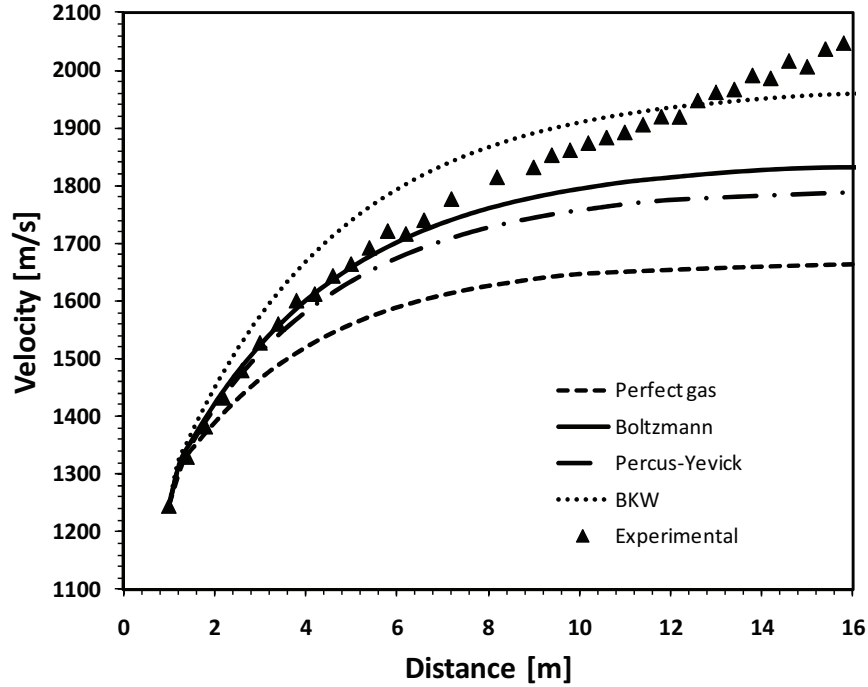


Figure 1.7: Velocity-distance plot for  $2.95CH_4 + 2O_2 + 5.7N_2$  propellant with unsteady modeling (Ideal gas EoS was used at station 1, and various real gas EoS at station 2.),  $L_{CV} = 2L_p$ ,  $P_1 = 5.15 MPa$

order of 16% to 28% was observed at 10MPa and 20MPa consecutively. Previous analysis of the ram accelerator [31], [60] show that the higher the fill pressures, the greater acceleration will increase their effects.

In order to evaluate the effect of the unsteadiness assumption and to investigate the validity of TARAM, different calculations were performed at elevated pressures; i.e., 10 MPa and 20 MPa. The experimental data used for the following theoretical comparison were those from published data given by Bauer [60]. The reactive mixture used for both experiments was:  $2.6CH_4 + 2O_2 + 9.2N_2$ . The control volume length was set to two times the projectile length ( $L_{CV} = 2L_p$ ). Results from the modeling are presented in figure (1.10) and figure (1.11) for 10 and 20 MPa consecutively.

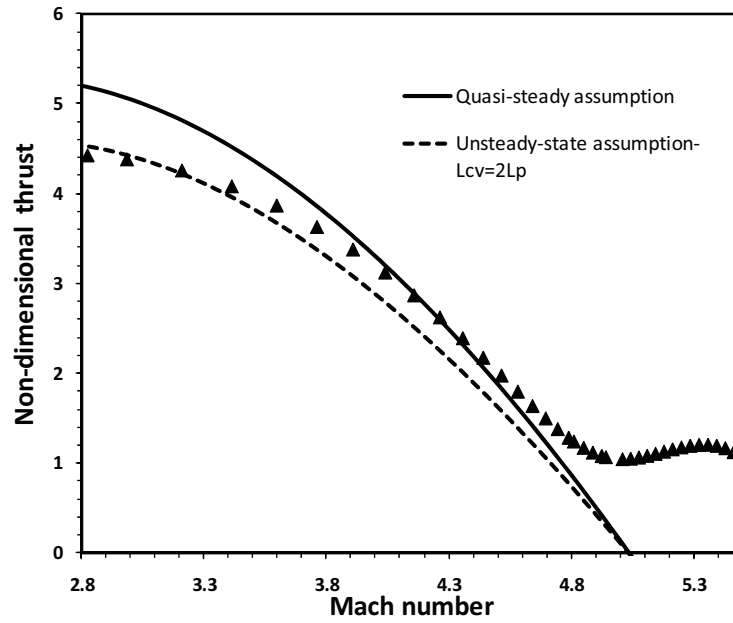


Figure 1.8: Non-dimensional Thrust-Mach plot for  $2.95CH_4 + 2O_2 + 5.7N_2$  propellant at  $p_1 = 5.15$  MPa;  $L_{CV} = 2L_p$  (Ideal gas EoS was used at station 1, and Boltzmann EoS was used for the calculation of properties of combustion products)

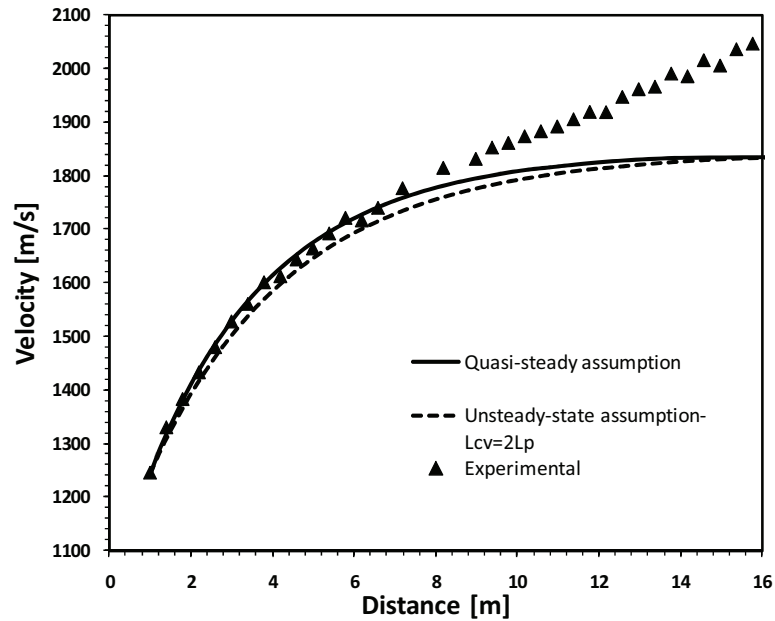


Figure 1.9: Velocity-distance plot for  $2.95CH_4 + 2O_2 + 5.7N_2$  propellant at  $p_1 = 5.15$  MPa;  $L_{CV} = 2L_p$  (Ideal gas EoS was used at station 1, and Boltzmann EoS was used for the calculation of properties of combustion products)

As expected TARAM was able to predict ram accelerator performance at high fill pressures for quasi-steady and unsteady assumption. An average of 41.6% of difference was obtained at 10 MPa, this difference was even higher at 20 MPa, value of 59.62%.

## **1.5 Compressibility effects of unreacted propellant on thermally choked ram accelerator performance**

One dimensional modeling of ram accelerator flow process has been successful in predicting the experimental velocity-distance profile when real gas corrections are applied to the combustion products of propellants at initial fill pressure up to 8 MPa. A further refinement of the modeling takes into account real gas corrections for the initial state at higher fill pressure. It was found that the Redlich-Kwong equation of state accurately determines the thermodynamic properties of the unreacted propellant for fill pressure up to 20 MPa. It was found that thrust could increase by 30 % than that predicted for Ideal gas. The equations to be solved are the same as presented earlier in the real gas section. The main difference is the general form of the thermodynamic parameters of the initial state, Bauer et al.[59] carried out an investigation and showed that a real gas equation of state is required that is appropriate for unreacted gaseous mixtures at initial pressures in range of 10 to 50 MPa.

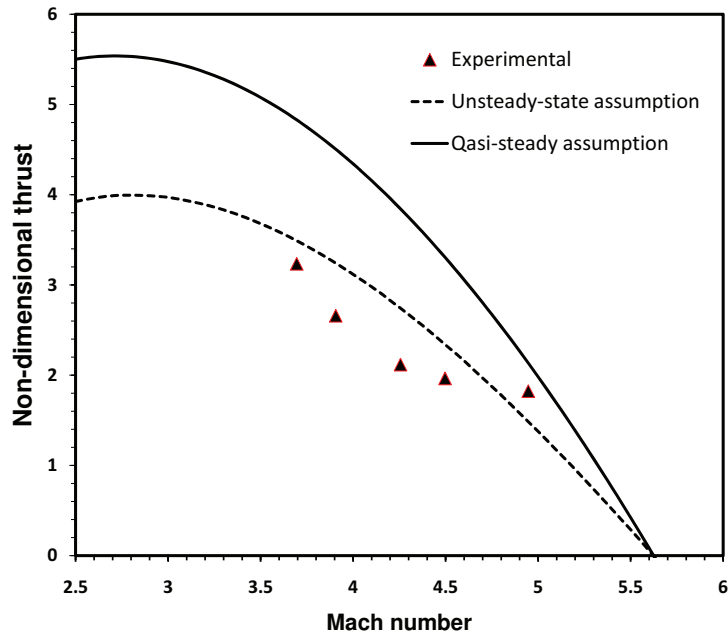


Figure 1.10: Non-dimensional Thrust-Mach plot for  $2.6CH_4 + 2O_2 + 5.92N_2$  propellant,  $p_1 = 15$  MPa;  $L_{CV} = 2L_p$  (Ideal gas EoS was used at station 1, and Boltzmann EoS was used for the calculation of properties of combustion products), Experimental data from [54]

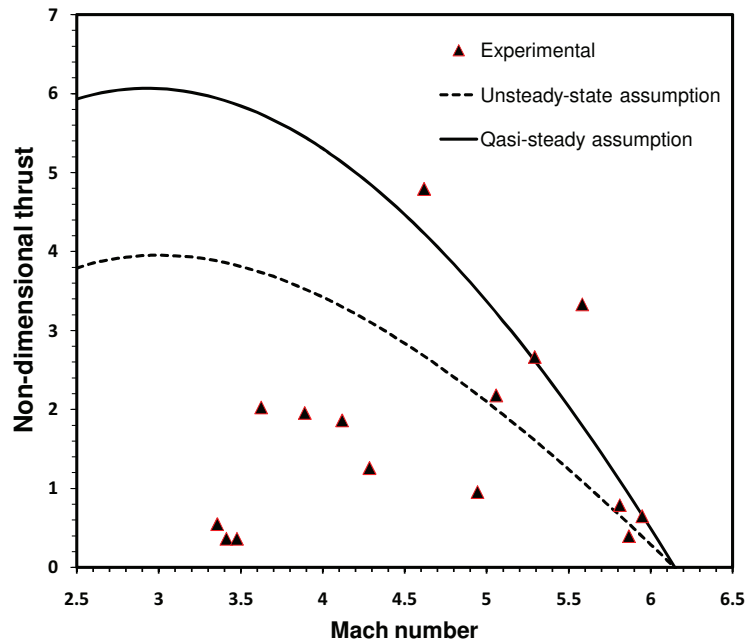


Figure 1.11: Non-dimensional Thrust-Mach plot for  $2.6CH_4 + 2O_2 + 5.92N_2$  propellant,  $p_1 = 20$  MPa;  $L_{CV} = 2L_p$  (Ideal gas EoS was used at station 1, and Boltzmann EoS was used for the calculation of properties of combustion products), Experimental data from [54]

We will present here the form of the Redlich-Kwong equation of state which was included in TARAM computer program.

$$\frac{pv}{RT} = \sigma(v, T) = \frac{v}{v-b} - \frac{aT^{1.5}}{R(v+b)} \quad (1.5.1)$$

where a and b are physical constant depending on the critical pressure and temperature of the mixture.

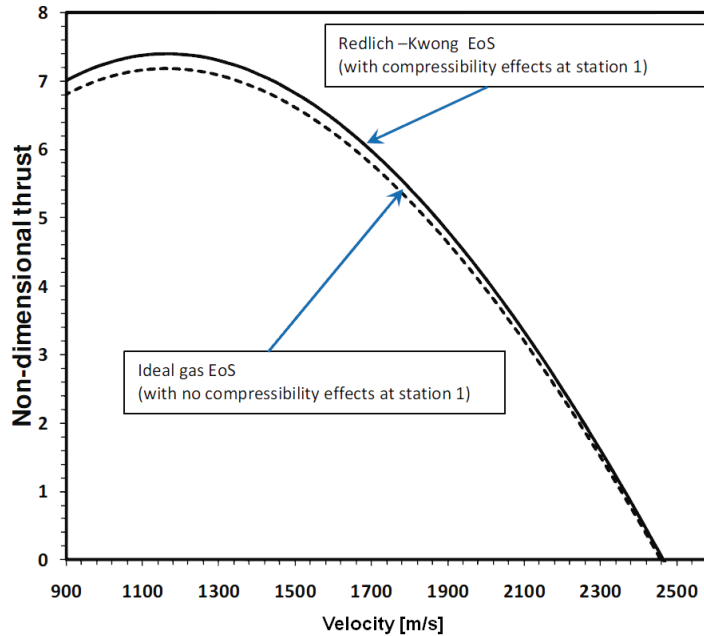


Figure 1.12: Non-dimensional Thrust-Velocity plot for  $2.95CH_4 + 2O_2 + 5.7N_2$  at  $P_1 = 20$  MPa (Boltzmann EoS was used for the calculation of properties of combustion products)

A significant effect of the initial pressure on the non-dimensional thrust was observed figure (1.12), which shows the importance of the correction as the pressure increases. The higher the pressure the greater the correction, thus the non-dimensional thrust is strongly shifted to higher values; *i.e.*, order of 4% observed at  $P_1 = 20$  MPa.

## 1.6 Summary

The predicted acceleration performance, based on the quasi-steady model, of the ram accelerator under conditions where the projectile is experiencing very high accelerations; i.e., greater than 30,000 g, is much greater than that observed in experiments. This discrepancy is attributed to the increase of mass of the propellant accumulating in the control volume, such that it approaches the mass of the projectile itself. The unsteady analysis describes the effects of the flow around the projectile as a global process between the state of the incoming flow and thermally choked exit flow. A computer code program was presented to predict the performance of the ram accelerator in the thermally choked propulsive mode, using both quasi-steady and unsteady flow assumptions. The first version of this program code includes the real gas effect in quasi-steady and unsteady calculations. It also incorporates the following equations of state: ideal gas, Boltzmann, Percus-Yevick, and Becker-Kistiakowsky-Wilson (BKW). The (BKW) EoS is used for the calculation of detonation characteristics at extremely elevated pressures, however, in this specific case, all the adjustable parameters must be set accordingly. We have used BKW EoS in this present ram accelerator modeling as a reference to show the capability of the program at incorporating any equation of state. Another issue raised when using the unsteady assumption is the length of the control volume, the initial results were determined by assuming a value of twice the projectile length, this value was derived from the experimental observation although this value varies with the in-coming Mach number. A further refinement on the unsteady one-dimensional modeling is to investigate the variation of the control volume length as a function of the incoming Mach number. An attempt was made for this matter by modeling the reactive flow around the projectile for different incoming



Mach numbers. Details about influence of ( $L_{CV}$ ) in the modeling will be presented in chapter 6.

# Chapter 2

## Conservation equations for reacting flows

### 2.1 Introduction

The content of this section is based on Refs.[103], [104], [105], [106], but it appears in a virtually identical manner in most textbooks and review articles. The equations governing flows with chemical reactions are the continuity, the species conservation equations and the energy. A solution to these equations provides in principle all the information we seek from a reacting flow, also the main differences between these equations and the usual Navier-Stokes equations for non reacting cases are presented. This chapter presents the conservation equations for reacting flows and highlights.

### 2.2 primitive variables

The Navier-Stokes equations can be applied to multi-reaction gases. First, species are characterized through their mass fraction  $Y_k$  for  $k = 1$  to  $N$  where  $N$  is the number

of species in reacting mixture. The mass fraction  $Y_k$  are defined by:

$$Y_k = \frac{m_k}{m} \quad (2.2.1)$$

where  $m_k$  is the mass of species  $k$  present in given volume  $V$  and  $m$  is the total mass of gas in this volume.

The primitive variables for a three-dimensional compressible reacting flow are: the density  $\rho = m/V$ , the three dimensional velocity field  $u_i$ , one variable for energy (or pressure or enthalpy or temperature  $T$ ), and the mass fraction  $Y_k$  of the  $N$  reacting species. Going from non reacting flow to combustion requires solving for  $N + 5$  variables instead of 5. Knowing that most chemical schemes involve a large number of species ( $N$  is larger than 50 for most simple hydrocarbon fuels), this is the first significant effort needed to compute reacting flows [106].

## 2.3 Thermochemistry

For a mixture of  $N$  ideal gases, total pressure is the sum of partial pressures:

$$p = \sum_{k=1}^N p_k$$

where

$$p_k = \rho_k \frac{R}{W_k} T \quad (2.3.1)$$

where the  $T$  is the Temperature,  $R = 8.314(J/moleK)$  is the ideal gas constant,  $\rho_k = \rho Y_k$  and  $W_k$  are respectively the density and the atomic weight of species  $k$ . Since the density  $\rho$  of the multi-species gas is:

$$\rho = \sum_{k=1}^N \rho_k \quad (2.3.2)$$

the equation of state is

$$p = \rho \frac{R}{W} T \quad (2.3.3)$$

where  $W$  is the mean molecular weight of the mixture given by:

$$\frac{1}{W} = \sum_{k=1}^N \frac{Y_k}{W_k} \quad (2.3.4)$$

The mole fraction  $X_k$  is the ratio of the number of moles of species  $k$  in volume  $V$  to the total number of moles in the volume.

$$X_k = \frac{W}{W_k} Y_k \quad (2.3.5)$$

The molar concentration  $[X_k]$  is the number of moles of species  $k$  per unit volume. It is the quantity used to evaluate kinetics rates of chemical reactions see eq. (2.6.5).

$$[X_k] = \rho \frac{X_k}{W} \quad (2.3.6)$$

For reacting flow, there are multiple possible variables to represent energy or enthalpy:

· ***Sensible:***

Energy

$$e_{sk} = \int_{T_0}^T C_{vk} dT - RT_0/W_k \quad (2.3.7)$$

Enthalpy

$$h_{sk} = \int_{T_0}^T C_{pk} dT \quad (2.3.8)$$

· ***Sensible + Chemical:***

Energy

$$e_k = e_{sk} + \Delta h_{f,k}^0 \quad (2.3.9)$$

Enthalpy

$$h_k = h_{s,k} + \Delta h_{f,k}^0 \quad (2.3.10)$$

The mass enthalpy of formation of species  $k$  at reference temperature  $T_0$  is written  $\Delta h_{f,k}^0$ . The standard reference state used to tabulate formation enthalpies is usually set to  $T_0 = 298.15K$ . In addition to the reference temperature  $T_0$ , a reference enthalpy (or energy) value must also be chosen. This level is set up by assuming that the enthalpy  $h_k$  is such that:

$$h_k = \underbrace{\int_{T_0}^T C_{pk} dT}_{\text{sensible}} + \underbrace{\Delta h_{f,k}^0}_{\text{chemical}} \quad (2.3.11)$$

The sensible enthalpy  $h_{sk}$  is zero at  $T = T_0$  for all substance. The heat capacities at constant pressure of species  $k$  ( $C_{pk}$ ) are mass heat capacities related to molar capacities  $C_{pk}^m$  by :

$$C_{pk} = \frac{C_{pk}^m}{W_k} \quad (2.3.12)$$

The mass heat capacities  $C_{vk}$  at constant Volume are related to the  $C_{pk}$  by :

$$C_{pk} - C_{vk} = \frac{R}{W_k} \quad (2.3.13)$$

The enthalpy  $h$  is defined by

$$h = \sum_{k=1}^N h_k Y_k = \sum_{k=1}^N \left( \int_{T_0}^T C_{pk} dT + \Delta h_{f,k}^0 \right) Y_k = \int_{T_0}^T C_p dT + \sum_{k=1}^N \Delta h_{f,k}^0 Y_k \quad (2.3.14)$$

the energy  $e = h - \frac{p}{\rho}$  is given by, using Eq. (2.3.3), Eq. (2.3.4) and Eq. (2.3.10):

$$\begin{aligned} e &= \sum_{k=1}^N \left( \int_{T_0}^T C_{pk} dT - \frac{RT}{W_k} + \Delta h_{f,k}^0 \right) Y_k = \sum_{k=1}^N \left( \int_{T_0}^T C_{vk} dT - \frac{RT_0}{W_k} + \Delta h_{f,k}^0 \right) Y_k \\ &= \int_{T_0}^T C_v dT - \frac{RT_0}{W} + \sum_{k=1}^N \Delta h_{f,k}^0 Y_k = \sum_{k=1}^N e_k Y_k \end{aligned} \quad (2.3.15)$$

the heat capacity at constant pressure of the mixture,  $C_p$ , is:

$$C_p = \sum_{k=1}^N C_{p,k} Y_k = \sum_{k=1}^N C_{pk}^m \frac{Y_k}{W_k} \quad (2.3.16)$$

the heat capacity of the mixture at constant volume,  $C_v$ , is defined as:

$$C_v = \sum_{k=1}^N C_{v,k} Y_k = \sum_{k=1}^N C_{vk}^m \frac{Y_k}{W_k} \quad (2.3.17)$$

where the heat capacities  $C_{vk}^m = C_{pk} m - \frac{R}{W_k}$  for molar values.

## 2.4 Viscous tensor

The velocity components are called  $u_i$  for  $i = 1$  to 3. The viscous tensor  $\tau_{ij}$  is defined by:

$$\tau_{ij} = -\frac{2}{3}\mu \frac{\partial u_k}{\partial x_k} \delta_{ij} + \mu \left( \frac{\partial u_i}{\partial x_j} + \frac{\partial u_j}{\partial x_i} \right) \quad (2.4.1)$$

where  $\mu$  is the dynamic viscosity. The kinematic viscosity is  $\nu = \mu/\rho$ .  $\delta_{ij}$  is the Kronecker symbol:  $\delta_{ij} = 1$  if  $i = j$ , 0 otherwise. Viscous and pressure tensors are combined into the  $\sigma_{ij}$  tensor:

$$\sigma_{ij} = \tau_{ij} - p\delta_{ij} = -p\delta_{ij} - \frac{2}{3}\mu \frac{\partial u_k}{\partial x_k} \delta_{ij} + \mu \left( \frac{\partial u_i}{\partial x_j} + \frac{\partial u_j}{\partial x_i} \right) \quad (2.4.2)$$

## 2.5 Molecular transport of species and heat

The heat diffusion coefficient is called  $\lambda$ . The diffusion coefficient of species  $k$  in the rest of the mixture is called  $D_k$ . The diffusion process involves binary diffusion coefficient ( $D_i$ ) and require the resolution of system giving diffusion velocities. The  $D_k$  coefficients are characterized in terms of Lewis number defined by:

$$L_{ek} = \frac{\lambda}{\rho C_p D_k} = \frac{D_{th}}{D_k} \quad (2.5.1)$$

where  $D_{th} = \lambda/\rho C_p$  is the heat diffusivity coefficient. The Lewis number  $L_{ek}$  compares the diffusion speeds of heat and species  $k$ , this parameter is important for laminar

flames. The Prandtl number,  $P_r$  compares momentum and heat transport:

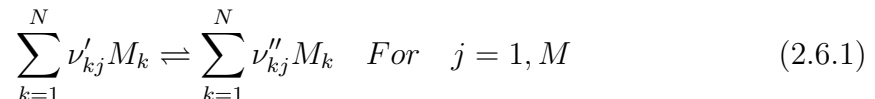
$$P_r = \frac{\nu}{\lambda/(\rho C_p)} = \frac{\rho \nu C_p}{\lambda} = \frac{\mu C_p}{\lambda} \quad (2.5.2)$$

The Schmidt number,  $S_{ck}$ , compares momentum and species  $k$  molecular diffusion

$$S_{ck} = \frac{\nu}{D_k} = P_r L_{ek} \quad (2.5.3)$$

## 2.6 Chemical kinetics

We consider a chemical system of  $N$  species reacting through  $M$  reactions:



where  $M_k$  is a symbol for species  $k$ .  $\nu'_{kj}$  and  $\nu''_{kj}$  are the molar stoichiometric coefficients of species  $k$  in reaction  $j$ . Mass conservation enforces:

$$\sum_{k=1}^N \nu'_{kj} W_k \rightleftharpoons \sum_{k=1}^N \nu''_{kj} W_k, \quad \text{or} \quad \sum_{k=1}^N \nu_{kj} W_k = 0 \quad \text{For } j = 1, M \quad (2.6.2)$$

where

$$\nu_{kj} = \nu''_{kj} - \nu'_{kj}$$

for simplicity, only mass reaction rates are used. For species  $k$ , this rate  $\omega$  is the sum of rates  $\omega_{kj}$  produced by all  $M$  reactions:

$$\dot{\omega}_k = \sum_{j=1}^M \dot{\omega}_{kj} = W_k \sum_{j=1}^M \nu_{kj} Q_j \quad (2.6.3)$$

with

$$\frac{\dot{\omega}_{kj}}{W_k \nu_{kj}} = Q_j$$

where  $Q_i$  is the rate of progress of reaction  $j$ . Summing all reaction rates  $\dot{\omega}_k$ , we obtain:

$$\sum_{k=1}^M \dot{\omega}_k = \sum_{j=1}^M (Q_j \sum_{k=1}^N W_k \nu_{kj}) = 0 \quad (2.6.4)$$

showing that total mass is conserved. the progress rate  $Q_j$  of reaction  $j$  is written :

$$Q_j = K_{fj} \prod_{k=1}^N [X_k]^{\nu'_{kj}} - K_{rj} \prod_{k=1}^N [X_k]^{\nu''_{kj}} \quad (2.6.5)$$

## 2.7 Stoichiometry in premixed flames

The fuel and the oxidizer mass fractions and their ratio is used to characterize the flame. There are different ways to define the equivalence ration depending on the configuration (premixed or non premixed) In a premixed configuration, fuel and oxidizer are mixed before starting the combustion. If  $\nu'_f$  and  $\nu''_f$  are the coefficients corresponding to fuel and oxidizer when considering an overall unique reaction of the type



the mass fraction of fuel and oxidizer correspond to stoichiometric condition when:

$$\left(\frac{Y_O}{Y_F}\right)_{st} = \frac{\nu'_O W_O}{\nu'_F W_F} = s \quad (2.7.2)$$

$s$  is the mass stoichiometric ratio. The equivalence ratio of a given mixture is then :

$$\phi = s \frac{Y_F}{Y_O} = \left(\frac{Y_F}{Y_O}\right) / \left(\frac{Y_F}{Y_O}\right)_{st} \quad (2.7.3)$$

It can also recast as:

$$\phi = s \frac{\dot{m}_F}{\dot{m}_O} \quad (2.7.4)$$

where  $m_F$  and  $m_O$  are respectively the mass flow rates of fuel and oxidizer.



## 2.8 Conservation of momentum

The equation of momentum is the same in reacting and non reacting flows:

$$\frac{\partial}{\partial t}\rho u_j + \frac{\partial}{\partial x_i}\rho u_i u_j = -\frac{\partial p}{\partial x_j} + \frac{\partial \tau_{ij}}{\partial x_i} + \rho \sum_{k=1}^N Y_k f_{k,j} = \frac{\partial \sigma_{ij}}{\partial x_i} + \rho \sum_{k=1}^N Y_k f_{k,j} \quad (2.8.1)$$

where  $f_{k,j}$  is the volume force acting on species  $k$  in direction  $j$ . Even though this equation does not include explicit reaction terms, the flow is modified by combustion: the dynamic viscosity  $\mu$  strongly changes because temperature varies in ratio from 1:8 or 1:10. Density also changes in the same ratio and dilatation through the flame front increases all speeds by the same ratio. As a consequence, the local Reynolds number varies much more than in non reacting flow: even though the momentum equations are the same with and without combustion, the flow behavior is very different. A typical example is found in jets: turbulent non reacting jets become laminar once they are ignited [106].

## 2.9 Conservation of mass and species

Because the the combustion does not generate mass, the total mass conservation equation is unchanged compared to non reacting flows

$$\frac{\partial \rho}{\partial t} + \frac{\partial \rho u_i}{\partial x_i} = 0 \quad (2.9.1)$$

the mass conservation equation for species  $k$  is written:

$$\frac{\partial \rho Y_k}{\partial t} + \frac{\partial}{\partial x_i}(\rho(u_i + V_{k,i})Y_k) = \dot{\omega}_k \quad \text{For } k = 1, N \quad (2.9.2)$$

where  $V_{k,i}$  is the  $i$ -component of the diffusion velocity  $V_k$  of species  $k$  and  $\dot{\omega}_k$  is the reaction rate of species  $k$ . By definition:

$$\sum_{k=1}^N Y_k V_{k,i} = 0 \quad \text{and} \quad \sum_{k=1}^N \dot{\omega}_k = 0 \quad (2.9.3)$$

## 2.10 Conservation of energy

The conservation energy can be written as follows:

$$\rho \frac{Df}{Dt} = \rho \left( \frac{\partial f}{\partial t} + u_i \frac{\partial f}{\partial x_i} \right) = \frac{\partial \rho f}{\partial t} + \frac{\partial (\rho u_i f)}{\partial x_i} \quad (2.10.1)$$

$f$  can hold enthalpy, energy, or temperature. From the conservation energy we write the energy total:

$$\rho \frac{De_t}{Dt} = \frac{\partial \rho e_t}{\partial t} + \frac{\partial}{\partial x_i} (\rho u_i e_t) = \frac{\partial q_i}{\partial x_i} + \frac{\partial}{\partial x_j} (\sigma_{ij} u_i) + \dot{Q} + \rho \sum_{k=1}^N Y_k f_{k,i} (u_i + V_{k,i}) \quad (2.10.2)$$

where  $\dot{Q}$  is the heat source term,  $\rho \sum_{k=1}^N Y_k f_{k,i} (u_i + V_{k,i})$  is the power produce by volume forces  $f_k$  on species  $k$ . The energy flux  $q_i$  is:

$$q_i = -\lambda \frac{\partial T}{\partial x_i} + \rho \sum_{k=1}^N h_k Y_k V_{k,i} \quad (2.10.3)$$

where  $-\lambda \frac{\partial T}{\partial x_i}$  is the diffusion term (Fourier's Law), the second term is the diffusion of species with different enthalpies. Using the relation between energy and enthalpy  $h_t = e_t + p/\rho$  and the continuity equation yields:

$$\rho \frac{De_t}{Dt} = \rho \frac{Dh_t}{Dt} - \frac{Dp}{Dt} - p \frac{\partial u_i}{\partial x_i} \quad (2.10.4)$$

and

$$\rho \frac{De}{Dt} = \rho \frac{Dh}{Dt} - \frac{Dp}{Dt} - p \frac{\partial u_i}{\partial x_i} \quad (2.10.5)$$

using Eq. (2.10.4) and Eq. (2.10.2) gives the conservation equation for  $h_t$ :

$$\begin{aligned} \rho \frac{Dh_t}{Dt} &= \frac{\partial \rho h_t}{\partial t} + \frac{\partial}{\partial x_i} (\rho u_i h_t) = \frac{\partial p}{\partial t} - \frac{\partial q_i}{\partial x_i} + \frac{\partial}{\partial x_j} (\tau_{ij} u_i) \\ &\quad + \dot{Q} + \rho \sum_{k=1}^N Y_k f_{k,i} (u_i + V_{k,i}) \end{aligned} \quad (2.10.6)$$

The equation for the sum of sensible and chemical energy  $e$  is obtained by writing first the kinetic energy equation  $u_i u_j / 2$ . Multiplying the momentum equation (2.6.5) by  $u_j$  :

$$\frac{\partial}{\partial t} \left( \frac{1}{2} \rho u_j u_j \right) + \frac{\partial}{\partial x_i} \left( \frac{1}{2} \rho u_i u_j u_j \right) = u_j \frac{\partial \sigma_{ij}}{\partial x_i} + \rho \sum_{k=1}^N Y_k f_{k,j} u_j \quad (2.10.7)$$

Subtracting this equation from Eq. (2.10.1) gives a balance equation for  $e$ :

$$\begin{aligned} \rho \frac{De}{Dt} &= \frac{\partial \rho e}{\partial t} + \frac{\partial}{\partial x_i} (\rho u_i e) = - \frac{\partial q_i}{\partial x_i} + \sigma_{ij} \frac{\partial u_i}{\partial x_j} \\ &\quad + \dot{Q} + \rho \sum_{k=1}^N Y_k f_{k,i} V_{k,i} \end{aligned} \quad (2.10.8)$$

The conservation equation for the enthalpy  $h$  is then deduced from Eq. (2.10.4) and Eq. (2.10.8)

$$\begin{aligned} \rho \frac{Dh}{Dt} &= \frac{\partial \rho h}{\partial t} + \frac{\partial}{\partial x_i} (\rho u_i h) = \frac{\partial p}{\partial t} - \frac{\partial q_i}{\partial x_i} + \tau_{ij} \frac{\partial u_i}{\partial x_j} \\ &\quad + \dot{Q} + \rho \sum_{k=1}^N Y_k f_{k,i} V_{k,i} \end{aligned} \quad (2.10.9)$$

where the term  $\tau_{ij} \frac{\partial u_i}{\partial x_j}$  is the viscous heating source term. The above expressions are not always to implement in computational fluid dynamics because they use expressions for energy and enthalpy including chemical terms  $\sum_{k=1}^N \Delta h_{f,k}^0 Y_k$  in addition to sensible energy or enthalpy and because the heat flux includes new transport terms  $(\rho \sum_{k=1}^N h_k Y_k Y_{k,i})$ .

From the definition of  $h_s$  ( $h_s = h - \sum_{k=1}^N \Delta h_{f,k}^0 Y_k$ ), substituting  $h_s$  for  $h$  in Eq. (2.10.9) and using the species equation (2.9.2) leads to:

$$\rho \frac{Dh_s}{Dt} = \dot{\omega}_T + \frac{Dp}{Dt} + \frac{\partial}{\partial x_i} \left( \lambda \frac{\partial T}{\partial x_i} \right) - \frac{\partial}{\partial x_i} \left( \rho \sum_{k=1}^N h_{s,k} Y_k V_{k,i} \right) + \tau_{i,j} \frac{\partial u_i}{\partial x_j} + \dot{Q} + \rho \sum_{k=1}^N Y_k f_{k,i} V_{k,i} \quad (2.10.10)$$

where  $\dot{\omega}_T$  is the heat release due to combustion:

$$\dot{\omega}_T = - \sum_{k=1}^N \Delta h_{f,k}^0 \dot{\omega}_k \quad (2.10.11)$$

the term  $\frac{\partial}{\partial x_i} (\rho \sum_{k=1}^N h_{s,k} Y_k V_{k,i})$  is sometimes set to zero because it is usually negligible compared to  $\dot{\omega}_T$  the equation for sensible energy  $e_s$  may deduced from Eq. (2.10.10) and (2.6.8):

$$\rho \frac{De_s}{Dt} = \frac{\partial \rho e_s}{\partial t} + \frac{\partial (\rho u_i e_s)}{\partial x_i} = \dot{\omega}_T + \frac{\partial}{\partial x_i} \left( \lambda \frac{\partial T}{\partial x_i} \right) - \frac{\partial}{\partial x_i} \left( \rho \sum_{k=1}^N h_{s,k} Y_k V_{k,i} \right) + \sigma_{i,j} \frac{\partial u_i}{\partial x_j} + \dot{Q} + \rho \sum_{k=1}^N Y_k f_{k,i} V_{k,i} \quad (2.10.12)$$

Another way is to work with the sum of sensible and kinetic energy by adding Eq. (2.10.12) and (2.10.6) leads to the equation for  $E = e_s + \frac{1}{2} u_i u_i$ :

$$\rho \frac{DE}{Dt} = \frac{\partial \rho E}{\partial t} + \frac{\partial (\rho u_i E)}{\partial x_i} = \dot{\omega}_T + \frac{\partial}{\partial x_i} \left( \lambda \frac{\partial T}{\partial x_i} \right) - \frac{\partial}{\partial x_i} \left( \rho \sum_{k=1}^N h_{s,k} Y_k V_{k,i} \right) + \frac{\partial}{\partial x_j} (\sigma_{ij} u_i) + \dot{Q} + \rho \sum_{k=1}^N Y_k f_{k,i} (u_i + V_{k,i}) \quad (2.10.13)$$

in the same way the equation for  $H = h_s + \frac{1}{2} u_i u_i$  is obtained by adding Eq.(2.10.10) and (2.10.7):

$$\rho \frac{DH}{Dt} = \frac{\partial \rho H}{\partial t} + \frac{\partial (\rho u_i H)}{\partial x_i} = \dot{\omega}_T + \frac{\partial}{\partial x_i} \left( \lambda \frac{\partial T}{\partial x_i} \right) + \frac{\partial p}{\partial t} - \frac{\partial}{\partial x_i} \left( \rho \sum_{k=1}^N h_{s,k} Y_k V_{k,i} \right) + \frac{\partial}{\partial x_j} (\tau_{ij} u_i)$$

$$+\dot{Q} + \rho \sum_{k=1}^N Y_k f_{k,i}(u_i + V_{k,i}) \quad (2.10.14)$$

## 2.11 Summary

The conservation equations needed for reacting flows have been presented. The equations governing flows with chemical reactions are the continuity, the species conservation equations and the energy. A solution to these equations provides in principle all the information we seek from a reacting flow, also the main differences between these equations and the usual Navier-Stokes equations for non reacting cases were presented.

# Chapter 3

## Turbulent combustion modeling

### 3.1 Introduction

Turbulent combustion results from the interaction of chemistry and turbulence. When a flame interacts with a turbulent flow, turbulence is modified by combustion because of the strong flow accelerations through the flame induced by heat release, and because of the large changes in kinematic viscosity associated with temperature changes. This mechanism may generate turbulence, called "flame-generated turbulence" or damp it (re-laminarization due to combustion). On the other hand, turbulence alters the flame structure which may enhance the chemical reaction, but also, (in extreme cases) completely inhibits it, leading to flame quenching [107].

In this chapter, the elementary concept about turbulence relevant to turbulent combustion approaches is briefly recalled in section (3.2). Next, the balance equations describing mean flow field in Reynolds Averaged Navier-Stokes (RANS) approach are described briefly in section (3.3). The most relevant of two equations turbulence models are also presented. Details about the Eddy Dissipation Model (EDM) for

combustion modeling are presented in section(3.5).

## 3.2 Elementary notion of turbulence

The turbulent motion is highly random, unsteady and three dimensional, which makes it difficult to describe and predict. The prediction of turbulent flow is based on the time averaged partial equations, which have introduced statical correlations involving fluctuating velocities, temperature and scalar quantities whose magnitudes are not known. Further differential equations could be added for this turbulent correlation. The process of approximating these unknown correlations in terms of know quantities is known as Turbulence modeling.

This section describes some basic concepts of turbulence relevant to turbulent combustion approaches. Turbulence may be characterized by fluctuations of all local properties and occurs for large Reynolds number depending on the system geometry. Any property  $f$  is usually split into  $(\bar{f})$  and fluctuating ( $f'$ ) contributions.

$$f = \bar{f} + f' \quad (3.2.1)$$

The turbulence strength is generally characterized by the turbulence intensity  $I$  which is the ratio between the root mean square of the fluctuations  $f'$  and the mean value  $\bar{f}$ :

$$I = \frac{\sqrt{\overline{f'^2}}}{\bar{f}} \quad (3.2.2)$$

In some situations, the local value  $\bar{f}$  may be replaced by a relevant reference value  $\bar{f}_0$ . For example in boundary layers, the turbulence intensity is usually determined as the ratio of velocity fluctuations divided by the mean free stream velocity. Typical

values of the turbulence intensity  $I$  go from 0 (laminar flow) to tens of percent in typical wall-bounded flows: the local velocity in a turbulence flow may deviate from its mean value by tens of percent. Turbulence intensity is not a sufficient parameter to describe turbulent combustion. An important issue is how the turbulence energy is distributed over the different length scales present in the flow field and which length scales carry enough energy to interact with the flame front. Turbulence fluctuations are associated with different scales ranging from the largest, the integral length scale  $l_t$ , to the smallest one, the Kolmogorov length scale  $\eta_k$ . The integral scale is usually close to the characteristic size of the flow. For example, in a ducted flow, the integral scale is of the order of the duct size. A Reynolds number  $Re(r)$  is introduced for each turbulent scale:

$$Re(r) = \frac{u'(r)r}{\nu} \quad (3.2.3)$$

where  $u'(r)$  is the characteristic velocity of motion of size  $r$  and  $\nu$  is the flow kinematic viscosity. When  $r$  corresponds to the integral scale  $l_t$ , the corresponding Reynolds number is the integral Reynolds number:

$$Re(r) = Re(l_t) = \frac{u'l_t}{\nu} \quad (3.2.4)$$

Since the Reynolds number represents the ratio of inertia to viscous forces, the largest scales in turbulent flow are mainly controlled by inertia and are not affected by viscous dissipation. For homogeneous isotropic turbulence, the energy of large scales flows to the smaller scales through the Kolmogorov cascade. The energy flux from one to another (due to non-linear term  $u_i u_j$ ) is constant along scales and is given by the dissipation  $\varepsilon$  of the kinetic energy  $k$ . This dissipation  $\varepsilon$  is estimated as the ratio of



the kinetic energy,  $u'^2(r)$  divided by the time scale  $r/u'(r)$ :

$$\varepsilon = \frac{u'^2(r)}{\frac{r}{u'(r)}} \quad (3.2.5)$$

Along the cascade, the Reynolds number  $Re(r)$  goes down from  $Re_t$  to value close to unity, where inertia and viscous forces balance. This limit determines the smallest scale found in the turbulent flow; i.e, the Kolmogorov scale  $\eta_k$ , controlled by viscosity and by the dissipation rate  $\varepsilon$  of the turbulent kinetic energy  $k$

$$\eta_k = \left(\frac{\nu^3}{\varepsilon}\right)^{1/4} \quad (3.2.6)$$

Corresponding to unity Reynolds number:

$$Re_k = Re_{(\eta_k)} = \frac{u'_k \eta_k}{\nu} = \frac{\varepsilon^{1/3} \eta_k^{4/3}}{\nu} = 1 \quad (3.2.7)$$

The ratio of the integral length scale,  $l_t$ , to the Kolmogorov length scale,  $\eta_k$ , comparing the largest and smallest turbulence eddies, is then expressed from Eq.(3.10), (3.11), and (3.12)

$$\frac{l_t}{\eta_k} = \frac{u'^3/\varepsilon}{(\frac{\nu^3}{\varepsilon})^{1/4}} = Re_t^{3/4} \quad (3.2.8)$$

The strain  $\kappa(r)$  induced on a flame front by an eddy of size  $r$  maybe assumed to scale with  $u'(r)/r$ , which is the simplest estimate for the velocity gradients created by this eddy. Then:

$$\kappa(r) = \frac{u'(r)}{r} = \left(\frac{\varepsilon}{r^2}\right)^{1/3} \quad (3.2.9)$$

In the same way, the characteristic time scale of an eddy of size  $r$  is:

$$\tau_m(r) = \frac{r}{u'(r)} = \left(\frac{r^2}{\varepsilon}\right)^{1/3} = \frac{1}{\kappa(r)} \quad (3.2.10)$$

The Kolmogorov ( $\eta_k$ ) and integral ( $l_t$ ) length scales induce strain values given by:

$$\kappa(\eta_k) = \sqrt{\frac{\varepsilon}{\nu}} \quad ; \quad k(l_t) = \frac{\varepsilon}{u'^2} \approx \frac{\varepsilon}{k} \quad (3.2.11)$$

where  $u'^2$  measures the turbulence kinetic energy  $k$ . Although the scale close to Kolmogorov length have smallest sizes and velocities, they generate the highest stretch.

$$\frac{\kappa(\eta_k)}{k(l_t)} = \sqrt{\frac{l_t u'}{\nu}} = \sqrt{Re_t} \quad (3.2.12)$$

### 3.3 RANS simulation for turbulent combustion

Balance equations for the mean quantities in RANS simulations are obtained by averaging the instantaneous balance equations. This averaging procedure introduces unclosed quantities that have to be modeled, using turbulent combustion models.

#### 3.3.1 Averaging the balance equations

The natural starting point for averaging is the instantaneous balance equation for mass, species, momentum, and enthalpy from chapter 2.

$$\frac{\partial \rho}{\partial t} + \frac{\partial}{\partial x_i}(\rho u_i) = 0 \quad (3.3.1)$$

$$\frac{\partial \rho u_j}{\partial t} + \frac{\partial}{\partial x_i}(\rho u_i u_j) + \frac{\partial p}{\partial x_j} = \frac{\partial \tau_{i,j}}{\partial x_i} \quad (3.3.2)$$

$$\frac{\partial(\rho Y_k)}{\partial t} + \frac{\partial}{\partial x_i}(\rho u_i Y_k) = -\frac{\partial}{\partial x_i}(V_{k,i} Y_k) + \dot{\omega}_k \quad \text{For } k = 1, N \quad (3.3.3)$$

$$\frac{\partial \rho h_s}{\partial t} + \frac{\partial}{\partial x_i}(\rho u_i h_s) = \dot{\omega}_T + \frac{Dp}{Dt} + \frac{\partial}{\partial x_i}(\lambda \frac{\partial T}{\partial x_i}) - \frac{\partial}{\partial x_i}(\rho \sum_{k=1}^N h_{s,k} Y_k V_{k,i}) + \tau_{i,j} \frac{\partial u_i}{\partial x_j} \quad (3.3.4)$$

in constant density flows, Reynolds averaging consist in splitting any quantity  $f$  into a mean,  $\bar{f}$ , and a fluctuating,  $f'$  component ( $f = \bar{f} + f'$ ). Using this procedure with

the mass conservation equation (3.3.1) leads to :

$$\begin{aligned} \frac{\partial \bar{\rho}}{\partial t} + \frac{\partial}{\partial x_i}(\bar{\rho} u_i) &= \frac{\partial \bar{\rho}}{\partial t} + \frac{\partial}{\partial x_i}(\bar{\rho} \bar{u}_i + \overline{\rho' u'_i}) = 0 \\ \text{or } \frac{\partial \bar{\rho}}{\partial t} + \frac{\partial}{\partial x_i}(\bar{\rho} \bar{u}_i) &= -\frac{\partial}{\partial x_i}(\overline{\rho' u'_i}) \end{aligned} \quad (3.3.5)$$

where an unclosed quantity  $\overline{\rho' u'_i}$  corresponding to the correlation between density and velocity fluctuation. This term also acts as a mass source term for the mean flow field  $(\bar{\rho}, \bar{u}_i)$ .

Reynolds averaging for variable density flows introduces many other unclosed correlations between any quantity  $f$  and density fluctuations  $\overline{\rho' f'}$  to avoid this difficulty, mass-weighted averages (Favre averages) are usually preferred:

$$\tilde{f} = \frac{\overline{\rho f}}{\bar{\rho}} \quad (3.3.6)$$

Any quantity  $f$  may be split into mean and fluctuating components as:

$$f = \tilde{f} + f'' \quad \text{with} \quad \overline{f''} = 0 \quad (3.3.7)$$

using this formalism, the average balance equations become:

- Mass

$$\frac{\partial \bar{\rho}}{\partial t} + \frac{\partial}{\partial x_i}(\bar{\rho} \tilde{u}_i) = 0 \quad (3.3.8)$$

- Momentum

$$\frac{\partial \bar{\rho} \tilde{u}_i}{\partial t} + \frac{\partial}{\partial x_i}(\bar{\rho} \tilde{u}_i \tilde{u}_j) + \frac{\partial \bar{p}}{\partial x_i} = \frac{\partial}{\partial x_i}(\bar{\tau}_{i,j} - \overline{\rho u''_i u''_j}) \quad (3.3.9)$$

- Chemical species

$$\frac{\partial(\bar{\rho} \tilde{Y}_k)}{\partial t} + \frac{\partial}{\partial x_i}(\bar{\rho} \tilde{u}_i \tilde{Y}_k) = -\frac{\partial}{\partial x_i}(\overline{V_{k,i} Y_k} + \overline{\rho u''_i Y''_k}) + \bar{\omega}_k \quad \text{For } k = 1, N \quad (3.3.10)$$

- Enthalpy

$$\begin{aligned} \frac{\partial \bar{\rho} \tilde{h}_s}{\partial t} + \frac{\partial}{\partial x_i} (\bar{\rho} \tilde{u}_i \tilde{h}_s) &= \bar{\dot{\omega}}_T + \frac{\overline{Dp}}{Dt} + \frac{\partial}{\partial x_i} \left( \lambda \frac{\overline{\partial T}}{\partial x_i} - \overline{\rho u_i'' h_s''} \right) \\ &+ \tau_{i,j} \frac{\overline{\partial u_i}}{\partial x_j} - \frac{\partial}{\partial x_i} \left( \rho \sum_{k=1}^N h_{s,k} Y_k V_{k,i} \right) \end{aligned} \quad (3.3.11)$$

where

$$\frac{\overline{DP}}{Dt} = \frac{\partial \bar{p}}{\partial t} + u_i \frac{\overline{\partial p}}{\partial x_i} = \frac{\partial p}{\partial t} + \tilde{u}_i \frac{\partial p}{\partial t} + u'' \frac{\partial p}{\partial x_i} \quad (3.3.12)$$

These equations are identical to classical Reynolds averaged equations for constant density flows.

There is no simple relation between Favre ( $\tilde{f}$ ) and Reynolds ( $\bar{f}$ ) averages. A relation between these two quantities requires modeling of density fluctuation,  $\overline{\rho' f'}$  which remain hidden in Favre average quantities:

$$\bar{\rho} \tilde{f} = \bar{\rho} \bar{f} + \overline{\rho' f'} \quad (3.3.13)$$

### 3.3.2 Unclosed terms in Favre averages balance equations

The objective of turbulent combustion modeling is to propose closure for the unknown quantities found in Eq.(3.3.8) to (3.3.11):

#### Reynolds stresses ( $u_i'' u_j''$ )

These terms are closed by turbulence model. The closure may be done directly or by deriving the balance equations for Reynolds stresses. Most combustion works are based on the classical turbulence models developed for non-reacting flows, such as the  $k - \varepsilon$  model, simply rewritten in terms of Favre averaging. Heat release effects on Reynolds stresses are generally not explicitly taken into account.

**Species  $(\widetilde{u''_i Y_k''})$  and enthalpy  $(\widetilde{u''_i h''_s})$  turbulent fluxes.**

These fluxes are generally closed using a classical gradient assumption:

$$\widetilde{\rho u''_i Y_k''} = -\frac{\mu_t}{Sc_{kt}} \frac{\partial \widetilde{Y}_k}{\partial x_i} \quad (3.3.14)$$

where  $\mu_t$  is the turbulent viscosity, estimated from the turbulence model, and  $Sc_{kt}$  a turbulent Schmidt number for species  $k$ .

**Laminar diffusive fluxes for species or enthalpy**

These molecular terms are generally neglected against turbulent transport, assuming a sufficiently large turbulence level (large Reynolds number limit). They may also be retained by adding a laminar diffusivity to the turbulent viscosity  $\mu_t$  in Eq.(3.3.14).

$$\overline{V_{k,i} Y_k} = -\overline{\rho D_k \frac{\partial Y_k}{\partial x_i}} \approx -\overline{\rho} \overline{D}_k \frac{\partial \widetilde{Y}_k}{\partial x_i} \quad (3.3.15)$$

where  $\overline{D}$  is mean species molecular diffusion coefficient. The laminar heat diffusion flux in the enthalpy equation is generally rewritten as:

$$\overline{\lambda \frac{\partial T}{\partial x_i}} = \overline{\lambda} \frac{\partial \widetilde{T}}{\partial x_i} \quad (3.3.16)$$

where  $\overline{\lambda}$  is the mean thermal diffusivity.

**Species chemical reaction rates  $\overline{\dot{\omega}_k}$**

Modeling these mean reaction rates is the objective of most studies on turbulent flames: (these will be discussed in Eddy dissipation combustion model part)

**Pressure-velocity correlation  $\overline{u''_i \partial p / \partial x_i}$ .**

This term, found in Eq ( 3.3.12), is simply neglected in most RANS calculations. These equations, coupled to ad-hoc models, allows only the determination of mean quantities that may be quite different from instantaneous quantities

## 3.4 Classical turbulence models

In this section only two equation models will be presented here  $k - \varepsilon$  and  $k - \omega$ . The reader will find in the literature more about the turbulence models.

### 3.4.1 The Two-equation model $k - \varepsilon$

In this approach the turbulent viscosity is estimated as:

$$\mu_t = \bar{\rho} C_\mu \frac{k^2}{\varepsilon} \quad (3.4.1)$$

where the turbulent kinetic energy  $k$  and its dissipation rate  $\varepsilon$  are described by closure of two balance equations:

$k$ -equation:

$$\frac{\partial}{\partial t}(\bar{\rho}k) + \frac{\partial}{\partial x_i}(\bar{\rho}\tilde{u}_i k) = \frac{\partial}{\partial x_i}[(\mu + \frac{\mu_t}{\sigma_k})\frac{\partial k}{\partial x_i}] + P_k - \bar{\rho}\varepsilon \quad (3.4.2)$$

$\varepsilon$ -equation:

$$\frac{\partial}{\partial t}(\bar{\rho}\varepsilon) + \frac{\partial}{\partial x_i}(\bar{\rho}\tilde{u}_i \varepsilon) = \frac{\partial}{\partial x_i}[(\mu + \frac{\mu_t}{\sigma_\varepsilon})\frac{\partial \varepsilon}{\partial x_i}] + C_{\varepsilon 1} \frac{\varepsilon}{k} P_k - C_{\varepsilon 2} \bar{\rho} \frac{\varepsilon^2}{k} \quad (3.4.3)$$

The production term  $P_k$  is given by

$$P_k = -\bar{\rho} \widetilde{u_i'' u_j''} \frac{\partial \tilde{u}_i}{\partial x_j} \quad (3.4.4)$$

where the Reynolds stresses  $\widetilde{\rho u_i'' u_j''}$  are determined using Boussinesq expression:

$$\widetilde{\rho u_i'' u_j''} = \bar{\rho} \widetilde{u_i'' u_j''} = -\mu_t \left( \frac{\partial \tilde{u}_i}{\partial x_j} + \frac{\partial \tilde{u}_j}{\partial x_i} - \frac{2}{3} \frac{\delta_{ij} \tilde{u}_k}{\partial x_k} \right) + \frac{2}{3} \bar{\rho} k \quad (3.4.5)$$

The model constant are  $C_\mu = 0.09$   $\sigma_k = 1.0$   $\sigma_\varepsilon = 1.3$   $C_{\varepsilon 1} = 1.44$   $C_{\varepsilon 2} = 1.92$

### 3.4.2 The Two-equation model $k - \omega$

One of the advantages of the  $k - \omega$  formulation is the near wall treatment for low-Reynolds number computations. The model does not involve the complex non-linear damping functions required for the  $k - \varepsilon$  model and is therefore more accurate and more robust. A low-Reynolds  $k - \varepsilon$  model would typically require a near wall resolution of  $y^+ < 0.2$ , while a low-Reynolds number  $k - \omega$  model would require at least  $y^+ < 2$ . In industrial flows, even  $y^+ < 2$  cannot be guaranteed in most applications and for this reason, a new near wall treatment was developed for the  $k - \omega$  models. It allows for smooth shift from a low-Reynolds number form to a wall function formulation. The starting point of the present formulation is the  $k - \omega$  model developed by [108]. It solves two transport equations, one for the turbulent kinetic energy,  $k$ , and one for the turbulent frequency,  $\omega$ . The stress tensor is computed from the eddy-viscosity concept.

$k$ -equation:

$$\frac{\partial}{\partial t}(\bar{\rho}k) + \frac{\partial}{\partial x_i}(\bar{\rho}\tilde{u}_i k) = \frac{\partial}{\partial x_i}[\Gamma_k \frac{\partial k}{\partial x_i}] + P_k - Y_k \quad (3.4.6)$$

$\omega$ -equation :

$$\frac{\partial}{\partial t}(\bar{\rho}\omega) + \frac{\partial}{\partial x_i}(\bar{\rho}\tilde{u}_i \omega) = \frac{\partial}{\partial x_i}[\Gamma_\omega \frac{\partial \omega}{\partial x_i}] + P_\omega - Y_\omega \quad (3.4.7)$$

$P_k$  represent the generation of turbulence kinetic energy due to mean velocity gradients.  $P_\omega$  represents the generation of  $\omega$ .  $\Gamma_k$  and  $\Gamma_\omega$  represent the effective diffusivity of  $k$  and  $\omega$ , respectively.  $Y_k$  and  $Y_\omega$  represent the dissipation of  $k$  and  $\omega$  due to turbulence.

### Effective diffusivity

The effective diffusivity for the  $k - \omega$

$$\Gamma_k = \mu + \frac{\mu_t}{\sigma_k}$$

$$\Gamma_\omega = \mu + \frac{\mu_t}{\sigma_\omega}$$

Where  $\sigma_k$  and  $\sigma_\omega$  are the turbulent Prandtl number for  $k$  and  $\omega$  respectively, the turbulent viscosity is computed by combining  $k$  and  $\omega$  as follows:

$$\mu_t = \alpha^* \bar{\rho} \frac{k}{\omega} \quad (3.4.8)$$

### Low-Reynolds number correction

The coefficient  $\alpha^*$  damps the turbulent viscosity causing the low-Reynolds number correction given as:

$$\alpha^* = \alpha_\infty^* \left( \frac{\alpha_0^* + Re_t / R_k}{1 + Re_t / R_k} \right) \quad (3.4.9)$$

where

$$Re_t = \frac{\bar{\rho} k}{\mu \omega}$$

$$R_k = 6$$

$$\alpha_0^* = \frac{\beta_i}{3}$$

$$\beta_i = 0.072$$

for high Reynolds number from the  $k - \omega$  model,  $\alpha^* = \alpha_\infty^* = 1$

### Turbulence production

- Production of  $k$

$$P_k = -\overline{\rho u_i'' u_j''} \frac{\partial \tilde{u}_i}{\partial x_j} \quad (3.4.10)$$



To evaluate  $G_k$  in a manner consistent with the Boussinesq hypothesis,

$$P_k = \mu_t S^2$$

where  $S$  is the modulus of the mean rate-of-strain tensor, defined as:

$$S \equiv \sqrt{2S_{ij}S_{ij}}$$

- Production of  $\omega$  The production of  $\omega$  is given by :

$$P_\omega = \alpha \frac{\omega}{k} \overline{\rho u_i'' u_j''} \frac{\partial \tilde{u}_i}{\partial x_j} = \alpha \frac{\omega}{k} P_k \quad (3.4.11)$$

The coefficient  $\alpha$  defined as:

$$\alpha = \frac{\alpha_\infty}{\alpha^*} \left( \frac{\alpha_0 + Re_t/R_\omega}{1 + Re_t/R_\omega} \right) \quad (3.4.12)$$

where  $R_\omega = 2.95$ . At high Reynolds number  $\alpha = \alpha_\infty = 1$ .

### Turbulence dissipation

The dissipation of  $k$  is given by:

$$Y_k = \rho \beta' f_{\beta'} k \omega \quad (3.4.13)$$

where

$$f_{\beta'} = \begin{cases} 1 & \chi_k \leq 0 \\ \frac{1+680\chi_k^2}{1+400\chi_k^2} & \chi_k > 0 \end{cases}$$

where

$$\chi_k \equiv \frac{1}{\omega^3} \frac{\partial k}{\partial x_j} \frac{\partial \omega}{\partial x_j}$$

and

$$\beta' = \beta'_i [1 + \zeta^* F(M_t)]$$

$$\beta'_i = \beta'_\infty \left( \frac{4/15 + (Re_t/R_\beta)^4}{1 + (Re_t/R_\beta)^4} \right)$$

where  $\zeta^* = 1.5$ ,  $R_\beta = 8$ , and  $\beta'_\infty = 0.09$

The dissipation of  $\omega$  is given by:

$$Y_\omega = \rho\beta f_\beta\omega^2$$

where

$$f_\beta = \frac{1 + 70\zeta_\omega}{1 + 80\zeta_\omega}$$

$$\zeta_\omega = \left| \frac{\Omega_{ij}\Omega_{jk}S_{ki}}{(\beta_\infty^*\omega)^3} \right|$$

$$\Omega_{ij} = \frac{1}{2} \left( \frac{\partial u_i}{\partial x_j} - \frac{\partial u_j}{\partial x_i} \right)$$

$$S_{ij} = \frac{1}{2} \left( \frac{\partial u_j}{\partial x_i} + \frac{\partial u_i}{\partial x_j} \right)$$

and

$$\beta = \beta_i \left[ 1 - \frac{\beta_i^*}{\beta_i} \zeta^* F(M_t) \right]$$

$$F(M_t) = \begin{cases} 0 & M_t \leq M_{t0} \\ M_t^2 - M_{t0}^2 & M_t > M_{t0} \end{cases}$$

where

$$M_t^2 = \frac{2k}{a^2}$$

$$M_{t0} = 0.25$$

$$a = \sqrt{\gamma RT}$$

for the compressible flow the  $k - \omega$  can be written as follows:

$$\frac{\partial}{\partial t}(\bar{\rho}k) + \frac{\partial}{\partial x_i}(\bar{\rho}\tilde{u}_i k) = \frac{\partial}{\partial x_i} \left[ \left( \mu + \frac{\mu_t}{\sigma_k} \right) \frac{\partial k}{\partial x_i} \right] + P_k - \beta' \bar{\rho} k \omega \quad (3.4.14)$$

$$\frac{\partial}{\partial t}(\bar{\rho}\omega) + \frac{\partial}{\partial x_i}(\bar{\rho}\tilde{u}_i \omega) = \frac{\partial}{\partial x_i} \left[ \left( \mu + \frac{\mu_t}{\sigma_\omega} \right) \frac{\partial \omega}{\partial x_i} \right] + \alpha \frac{\omega}{k} P_k - \beta \bar{\rho} \omega^2 \quad (3.4.15)$$

### 3.4.3 The Base Line model (*BSL*)

The main problem with the Wilcox model is its well known strong sensitivity to free-stream conditions [109]. Depending on the value specified for  $\omega$  at the inlet, a significant variation in the results of the model can be obtained. This is undesirable and in order to solve the problem, a blending between the  $k-\omega$  model near the surface and the  $k-\varepsilon$  model in the outer region was developed by Menter [109]. It consists of a transformation of the  $k-\varepsilon$  model to a  $k-\omega$  formulation and a subsequent addition of the corresponding equations. The Wilcox model [108] is thereby multiplied by a blending function  $F_1$  and the transformed  $k-\varepsilon$  model by a function  $1-F_1$ .  $F_1$  is equal to one near the surface and switches over to zero inside the boundary layer (i.e., a function of the wall distance). At the boundary layer edge and outside the boundary layer, the standard  $k-\varepsilon$  model is therefore recovered.

Wilcox model:

$$\frac{\partial}{\partial t}(\bar{\rho}k) + \frac{\partial}{\partial x_i}(\bar{\rho}\tilde{u}_i k) = \frac{\partial}{\partial x_i}[(\mu + \frac{\mu_t}{\sigma_{k1}})\frac{\partial k}{\partial x_i}] + P_k - \beta'\bar{\rho}k\omega \quad (3.4.16)$$

$$\frac{\partial}{\partial t}(\bar{\rho}\omega) + \frac{\partial}{\partial x_i}(\bar{\rho}\tilde{u}_i\omega) = \frac{\partial}{\partial x_i}[(\mu + \frac{\mu_t}{\sigma_\omega})\frac{\partial \omega}{\partial x_i}] + \alpha_1\frac{\omega}{k}P_k - \beta_1\bar{\rho}\omega^2 \quad (3.4.17)$$

Transformed  $k-\varepsilon$ :

$$\frac{\partial}{\partial t}(\bar{\rho}k) + \frac{\partial}{\partial x_i}(\bar{\rho}\tilde{u}_i k) = \frac{\partial}{\partial x_i}[(\mu + \frac{\mu_t}{\sigma_{k2}})\frac{\partial k}{\partial x_i}] + P_k - \beta'\bar{\rho}k\omega \quad (3.4.18)$$

$$\frac{\partial}{\partial t}(\bar{\rho}\omega) + \frac{\partial}{\partial x_i}(\bar{\rho}\tilde{u}_i\omega) = (\frac{\partial}{\partial x_i}[(\mu + \frac{\mu_t}{\sigma_{\omega 2}})\frac{\partial \omega}{\partial x_i}] + 2\bar{\rho}\frac{1}{\sigma_{\omega 2}\omega}\frac{\partial k}{\partial x_i}\frac{\partial \omega}{\partial x_i} + \alpha_2\frac{\omega}{k}P_k - \beta_2\bar{\rho}\omega^2) \quad (3.4.19)$$

The equation of wilcox model are multiplied by function  $F_1$ , the transformed  $k-\varepsilon$  equations by  $1-F_1$  and the corresponding  $k$  and  $\omega$  equations are added to give the

BSL model

$$\frac{\partial}{\partial t}(\bar{\rho}k) + \frac{\partial}{\partial x_i}(\bar{\rho}\tilde{u}_i k) = \frac{\partial}{\partial x_i}[(\mu + \frac{\mu_t}{\sigma_{k3}})\frac{\partial k}{\partial x_i}] + P_k - \beta'\bar{\rho}k\omega \quad (3.4.20)$$

$$\frac{\partial}{\partial t}(\bar{\rho}\omega) + \frac{\partial}{\partial x_i}(\bar{\rho}\tilde{u}_i\omega) = \frac{\partial}{\partial x_i}[(\mu + \frac{\mu_t}{\sigma_{\omega 3}})\frac{\partial \omega}{\partial x_i}] + (1 - F_1)2\bar{\rho}\frac{1}{\sigma_{\omega 2}\omega}\frac{\partial k}{\partial x_i}\frac{\partial \omega}{\partial x_i} + \alpha_3\frac{\omega}{k}P_k - \beta_3\bar{\rho}\omega^2 \quad (3.4.21)$$

The model constants are given by:  $\beta' = 0.09$   $\alpha_1 = 5/9$   $\beta_1 = 0.075$   $\sigma_{k1} = 2$   $\sigma_{\omega 1} = 2$ ;  
 $\alpha_2 = 0.44$ ;  $\beta = 0.0828$ ;  $\sigma_{k2} = 1$   $\sigma_{\omega 2} = 1/0.856$

The subscript  $i = 1$  refer

to  $k - \varepsilon$  equation, and  $i = 2$  refers to  $k - \omega$  equation

### 3.4.4 The Shear Stress Transport model (*SST*)

The  $k - \omega$  based SST model [109] accounts for the transport of the turbulent shear stress and gives highly accurate predictions of the onset and the amount of flow separation under adverse pressure gradients. The BSL model combines the advantages of the Wilcox and the  $k - \varepsilon$  model, but still fails to properly predict the onset and amount of flow separation from smooth surfaces. The reasons for this deficiency are given in detail in [109]. The main reason is that both models do not account for the transport of the turbulent shear stress. This results in an over prediction of the eddy-viscosity. The proper transport behavior can be obtained by a limiter to the formulation of the eddy-viscosity:

$$\mu_t = \frac{a_1 k}{\max(a_1 w, SF_2)} \quad (3.4.22)$$

where

$$\nu_t = \frac{\mu_t}{\rho}$$

and  $F_2$  is blending function similar to  $F_1$ , which restricts the limiter to the wall boundary layer.

The blending functions are critical to the success of the method. Their formulation is based on the distance to the nearest surface and on the flow variables.

$$F_1 = \tanh(\arg_1^4) \quad (3.4.23)$$

with

$$\arg_1 = \min\left(\max\left(\frac{\sqrt{k}}{\beta'\omega y}, \frac{500\nu}{y^2\omega}\right), \frac{4\bar{\rho}k}{CD_{k\omega}\sigma_{\omega}2y^2}\right) \quad (3.4.24)$$

where  $y$  is the distance to the nearest wall,  $\nu$  is the kinematic viscosity and:

$$CD_{k,\omega} = \max\left(2\bar{\rho}\frac{1}{\sigma_{\omega}2\omega}\frac{\partial k}{\partial x_i}\frac{\partial \omega}{\partial x_i}, 1.0 * 10^{-10}\right) \quad (3.4.25)$$

$$F_2 = \tanh(\arg_2^2) \quad (3.4.26)$$

with

$$\arg_2 = \max\left(\frac{2\sqrt{k}}{\beta'\omega y}, \frac{500\nu}{y^2\omega}\right) \quad (3.4.27)$$

A disadvantage of standard two-equation turbulence models is the excessive generation of turbulence energy,  $P_k$ , in the vicinity of stagnation points. In order to avoid the build-up of turbulent kinetic energy in stagnation regions, a formulation of limiters for the production term in the turbulence equations is introduced by [109].

$$P_k = \mu_t \frac{\partial \tilde{u}_i}{\partial x_j} \left( \frac{\partial \tilde{u}_i}{\partial x_j} + \frac{\partial \tilde{u}_j}{\partial x_i} \right) \rightarrow \widetilde{P}_k = (P_k, 10\rho\beta k\omega) \quad (3.4.28)$$

## 3.5 Turbulent premixed flames

### 3.5.1 Introduction

Premixed combustion requires that fuel and oxidizer is completely mixed before combustion is allowed to take place, because the rate  $\dot{\omega}$  cannot be found from an averaging

of Arrhenius laws, a physical approach is required to derive models for turbulent combustion. Turbulent combustion involves various lengths, velocity and time scales describing turbulent flow field and chemical reactions. The physical analysis is mainly based on comparison between these scales. The turbulent flow is characterized by Reynolds number comparing turbulent transport to viscous forces:

$$Re_t = \frac{u' l_t}{\nu} \quad (3.5.1)$$

where  $u'$  is the velocity rms,  $l_t$  is the turbulence integral length scale and  $\nu$  the kinematic viscous of the flow. The Damköhler number compares the turbulent ( $\tau_t$ ) and the chemical ( $\tau_c$ ) time scales:

$$D_a = \frac{\tau_t}{\tau_c} \quad (3.5.2)$$

In the limit of high Damköhler numbers ( $D_a \gg 1$ ) [110], the chemical time is short compared to the turbulent one, corresponding to thin reaction zone distorted and convected by the flow field. The internal structure of the flame is not strongly affected by turbulence and may be described as a laminar flame element called a flamelet. The turbulence structures wrinkle and strain the flame surface. On the other hand, a low Damköhler number ( $D_a \ll 1$ ) corresponds to slow chemical reaction. The turbulent time scale is typically in the order of one-tenth of a second. Thus, the Damköhler number, typically, has a very broad spectrum in a reacting flow situation. It is important to note here that  $D_a$  is actually a result that evolves out of solving a reactive flow problem, rather than being a parameter, because neither  $\tau_t$  nor  $\tau_c$  are known a priori. From a physical standpoint, this implies that  $D_a$  cannot be controlled experimentally with any degree of certainty. It can only be qualitatively controlled by varying the inlet turbulent fluctuations, so that the turbulent time scale

changes. However, since the fluid-mechanical problem is intimately coupled to the chemical rate equations through the density and pressure, it is impossible to quantify the exact change in the Damköhler number in an experimental situation.

### **3.5.2 Interaction between turbulence and chemical kinetics**

The interaction of turbulence and chemical reactions occurs in turbulent reacting flows over a wide range of flow conditions [111], [112]. Various degrees of interaction between turbulence and chemical reactions can lead to different phenomena. Weak interactions between turbulence and chemical reactions may simply modify the flame slightly causing wrinkles of flame surface [105]. Strong interactions could cause a significant modification in both the chemical reactions and the turbulence. The interaction of turbulence and chemical reactions is a complex phenomenon that can cause significant modification in both the turbulence and chemical reactions. For chemical reactions with negligible heat release, this interaction has only one direction, that is, turbulence will modify the chemical rates, but the reactions have no influence on the flow field. The purpose of combustion is generating heat; therefore, one expects large density variations which can alter the fluid dynamics. Hence, the turbulence will experience strong influence by the chemical processes and vice versa [105]. It has been observed experimentally that the entrainment process in mixing layers has been significantly altered by the heat release leading for different growth rates than those expected in constant density flows [106]. On the other hand, strong turbulence can strain the flames to a point that chemical reactions can no longer keep up with mixing process causing the flame to extinguish [106]. The characteristics of

the interactions between turbulence and chemical reactions can be obtained by plotting the Damkohler number (i.e., the ratio of flow time scale and reaction time scale) versus the Reynolds number over the whole range of length scales [105].

Based on the length scales of flames and turbulence, two extreme regimes are identified. One extreme with the flame thickness much smaller than the smallest length of turbulence is identified as the flamelet regime. The other opposite extreme with thick flames compared to the smallest turbulence length is identified as the distributed reaction regime. The nature of the intermediate regimes between these two extremes is rather complex, and is yet to be explored. Unfortunately, many practical combustion systems involve a wide range of operation conditions including the intermediate regimes [106].

### 3.5.3 The Arrhenius approach

It is simple approach where the effect of the turbulence is neglected. This model is relevant only when the chemical time scales are larger than turbulent time scales low Damköhler number ( $\tau_c \gg \tau_t$ ) The reaction rate is expressed as:

$$\dot{\omega}_{Arrhenius} = A \text{Exp}(-E/RT)[fuel]^a[oxygen]^b \quad (3.5.3)$$

where  $A$  is the Pre exponential factor,  $E$  the activation energy, the constant  $a$  and  $b$ , are the degrees of reaction given by Westbrook and Dryer[72], and Jones and Lindstedt [113] .



### 3.5.4 The Eddy Break Up (EBU) model

The Eddy-Break-Up (EBU) model was introduced by Spalding in 1971 [114]. It is based on the assumption of "fast" chemistry. Under this assumption, the chemical reaction are assumed to occur infinitely fast. Hence the rate of reaction does not depend on the chemistry rate, but on the rate at which the fuel and oxidizer are mixed. The time required to break up a turbulent eddy is taken as the characteristic mixing time-scale. This time scale is proportional to the ratio of turbulent kinetic energy over its dissipation rate ( $k/\varepsilon$ ). Based on these considerations, the mean rate, can be then given in the form of an algebraic expression in terms of a typical turbulence time-scale and the local mean square fluctuation of the fuel concentration:

$$\dot{\omega} = C_{EBU} \frac{\varepsilon}{k} (\widetilde{C_{fuel}^{\prime 2}})^{1/2} \quad (3.5.4)$$

Where  $\widetilde{C_{fuel}^{\prime 2}}$  is the Favre variance of the product mass fraction, and  $C_{EBU}$  is assumed to be a universal constant, and a value of 0.53 was suggested for it by Mason and Spalding in 1973) [115]. Further details on the development of this model can found in [104]). Spalding argued that the model was equally applicable to both premixed and non-premixed flames.

### 3.5.5 The Eddy Dissipation Model (EDM)

Magnussen and Hjertager proposed their version of the EBU model in 1975 [116]. It was based on the same fundamental grounds as Spalding's model. For non-premixed flames [114], fuel and oxygen occur in separate eddies. Since chemical reactions occur very fast, the rate of combustion can be assumed to redetermined by the rate of intermixing of the fuel and oxygen eddies on molecular scale [117], which is given

by the rate of dissipation of the the eddies. Since there is a correlation between the fluctuation in the concentration of fuel and oxygen and their respective mean values, the rate of reaction can be expressed by the mean concentration of the reacting species [118]. Accordingly, for non-premixed flames, depending on whether the flame is locally fuel-starving or oxygen-starving.

The rate of combustion of fuel can be expressed as [117]:

$$\dot{\omega}_{fuel} = A \tilde{C}_{fuel} \frac{\varepsilon}{k} \quad (3.5.5)$$

$$\dot{\omega}_{fuel} = A \frac{\tilde{C}_{ox}}{(O/F)_{stoic}} \frac{\varepsilon}{k} \quad (3.5.6)$$

where A is a constant which depends on the structure of the flame and the rate of reaction between the fuel and oxygen,  $\tilde{C}_{fuel}$  is the local mean fuel concentration ( $kg/m^3$ ),  $\tilde{C}_{ox}$  is the local mean oxygen concentration ( $kg/m^3$ ), and  $(O/F)_{stoic}$  is the stoichiometric oxygen to fuel ratio. For premixed flames, fuel and oxygen occur in the same eddies. These eddies are separated by eddies containing hot combustion products [117]. The rate of combustion can be assumed to be determined by the rate of separated of these hot eddies, which is given by the same mechanism as outlined above. However, an extra equation needs to be written that accounts for the dissipation of hot eddies in cases where the concentrations of hot combustion products is low. Hence, for premixed flames,

$$\dot{\omega}_{fuel} = AB \frac{\tilde{C}_{prod}}{1 + (O/F)_{stoic}} \frac{\varepsilon}{k} \quad (3.5.7)$$

where B is a constant,  $\tilde{C}_{prod}$  is the local mean concentration of the combustion products. The three equations (3.5.5), (3.5.6), and (3.5.7) are assumed to be generally

applicable to both non-premixed and premixed turbulent flames [118]. The equation that yields the minimum reaction rate is the one that determines the local rate of combustion. The main advantage of this model over Spalding's model is that it is applicable for both non-premixed and premixed flames. This makes it more suitable for combustion in applications such as direct injection engines, where combustion occurs in both premixed and non premixed regimes. Also important is the fact that the combustion rate is proportional to the mean concentration of the intermittent quantities instead of the concentration fluctuations, which are more difficult to estimate than the mean quantities.

For non premixed flames, Magnussen and Hjertager [117] suggested values of  $A=4$  and  $B=0.5$  for the model constants. Gosman and harvey in 1982[119] proposed values of  $A=2$  and  $b=2.5$  for combustion in diesel engines. Pichon in 1989 [120] modified these values to  $A=16$  and  $B=2$ , while Varnavas and Assanis (1991) [121] got best results with values of  $A=0.5$  and  $B=0.5$ . In recent paper, Dillies et al(1997) [122] found that they could get agreement with measurements of burned mass fraction and combustion speed in direct injection diesel engine only by considering an arbitrary high value of the constant  $B$ . This wide range of values for the constant shows that there is degree of empiricism in the model, which to be expected, as we are seeking to describe the complicated interactions between flow and chemistry by simplified algebraic approach. Despite the empiricism in the model, there is much theoretical and experimental evidence to support the dependence of combustion on the rate of turbulent mixing.

The global reaction will be calculated from the minimum of the  $\dot{\omega}_{EDM}$  and minimum of  $\dot{\omega}_{arrhenius}$ :

$$\dot{\omega} = \min(\dot{\omega}_{EDM}, \dot{\omega}_{arrhenius}) \quad (3.5.8)$$

this means that if the turbulence is weak the reaction rate will be calculated from the Arrhenius law, and when the flow is fully turbulent the EDM will be utilized. The EDM relies on the idea that chemical reactions occur in the smallest turbulent eddies. The characteristic length scale of these eddies is represented by  $l_t = k^{3/2}/\varepsilon$  and the typical eddy life time is  $\tau_t = k/\varepsilon$  [118]. The chemical reaction is characterized by its induction time  $\tau_c$ . This depends on fluid pressure and temperature [105]

It is The Damköhler number which classifies whether Arrhenius approach or Eddy dissipation model will be utilized. If  $D_a$  is small compared to unity, the chemical induction time is limiting and Equation Arrhenius law is used. If  $D_a$  exceeds unity, the reaction rate is predominately influenced by turbulence and Equation Eddy dissipation model is selected.

### 3.6 Summary

Elementary concept about turbulence relevant to turbulent combustion was briefly recalled. Next, the balance equations describing mean flow field in Reynolds Averaged Navier-Stokes (RANS) approach were described. The most relevant of two equations turbulence models And details about the Eddy Dissipation Model (EDM) for combustion modeling were presented.

Details about the two equations turbulence model  $k - \varepsilon$  and  $k - \omega$  have been presented as they both will be used by the SST turbulence model, also the Eddy

break Up (EBU) for the turbulent combustion has been presented to give a brief history for the development of the Eddy Dissipation Model. This chapter presents some of the theories that have been put in place to address these issues.

# Chapter 4

## Numerical modeling

### 4.1 Introduction

Computational fluid dynamics solutions of the Reynolds Averaged Navier-Stokes (RANS) equations will be used to numerically predict the ram accelerator performance in the thermally choked combustion mode. Simulations will focus on a four-finned projectile operating in a 38-mm-diameter ram accelerator tube loaded with pre-mixed propellant gas; methane/oxygen/nitrogen at 5.15 MPa fill pressure. Simulations will be carried out for a series of in-coming velocities. The shear-stress transport turbulence model (SST) and the eddy dissipation combustion model(EDM), with detailed reaction mechanism will be used to simulate the fully turbulent reactive flow field in the ram accelerator. Simulations will take into account the effect of the radiation/turbulence interactions. The spherical harmonic P1 method is used, the gray medium assumption is employed and the Planck-mean absorption coefficients are used to determine the radiative properties of the gas-phase species.

The numerical simulation code used for this research effort is the ANSYS-CFX CFD code. It is a finite-volume CFD code that solves a system of coupled nonlinear partial differential equations (pde's) for a compressible multi-component turbulent flow. Principle pde's correspond to conservation of mass (continuity), momentum, absolute enthalpy and species mass fractions. CFX employs an iterative time-implicit pressure-based sequential procedure for the solution of the coupled pde's. Favre-averaged dependent variables are calculated and a standard two equation SST model is used for turbulent closure. The conservation equations are solved on an structured mesh, the discretization accuracy is first-order in time and second-order in space. CFX was designed for chemically reacting flows, with ports for incorporation of additional sub-models. In this research, we incorporate detail chemistry sub-routines.

In this chapter we will present in details the domain setup and the computational procedure.

## 4.2 Geometry

The projectile body has a bi-conical shape with the nose cone having a half-angle of 10 and length of 82 mm, whereas the after body is represented as a truncated cone having a convergence angle of 4.493 and length of 71 mm, as shown in figure 4.1. The projectile throat has a maximum diameter of 29 mm, situated at the joint of the two cones. The overall length of the projectile is 153 mm. More details about the projectile geometry is given in Appendix (B).

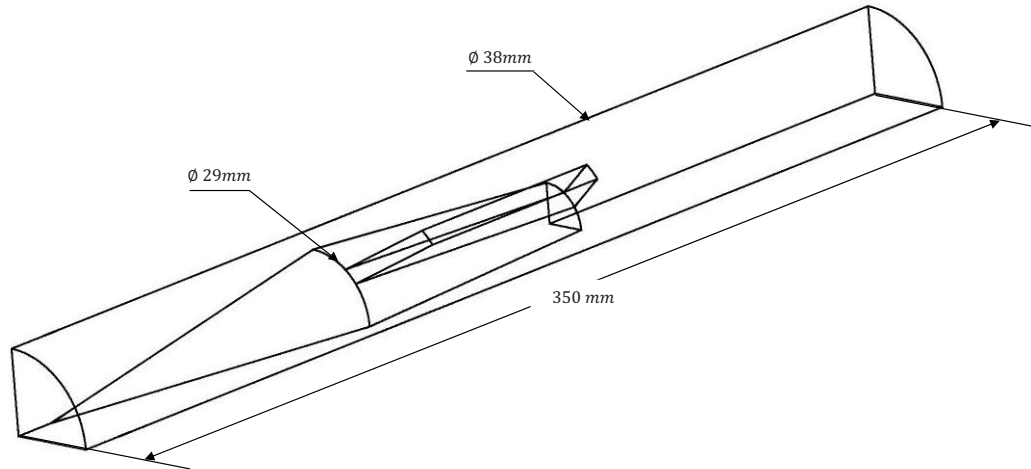


Figure 4.1: 3D geometry to be considered in the simulation

### 4.3 Two-dimensional simulations

For instance, due to the complexity of the modeling (combustion/turbulence, boundary layer/ shock waves interactions), simulations will be carried out for two dimensional axi-symmetric.

### 4.4 Computational procedure

The simulation solves two dimensional axis-symmetric compressible Reynolds-averaged Navier-Stokes (RANS) equations along with the SST turbulence model for turbulent viscous effect, the EDM model for turbulent combustion, and the P-1 radiation model for the heat losses. Simulations were carried out for a series of Mach number to investigate the effects of the chemical kinetics mechanism, i.e. one-step, two-step and five-step reaction, details about the chemical kinetics mechanism are presented in section(4.7.1). The solution starts with a precursor non-reactive computation until a steady-state convergence status, followed by the main reactive computation. Note



that the SST turbulence model constants are used as was introduced by Menter [109], and the two constant A, and B for the eddy dissipation combustion model are taken 4, and -1 consecutively.

Due to high accuracy required for capturing the shock waves, second order Total Variation Diminishing (TVD) scheme is used. This numerical scheme is broadly documented in the literature; see [123], [124].

#### 4.4.1 Mesh guidelines

The goal is to determine the required near wall mesh spacing,  $\Delta y$ , in terms of Reynolds number, running length, and a  $\Delta y^+$  target value. Using the wall-function described in (4.4.2), require a minimum a value of  $\Delta y^+ < 200$  to be valid.

The estimates will be based on the following correlations for flat plate:

$$\Delta y = L\Delta y^+ \sqrt{80} Re_L^{-0.9285} \quad (4.4.1)$$

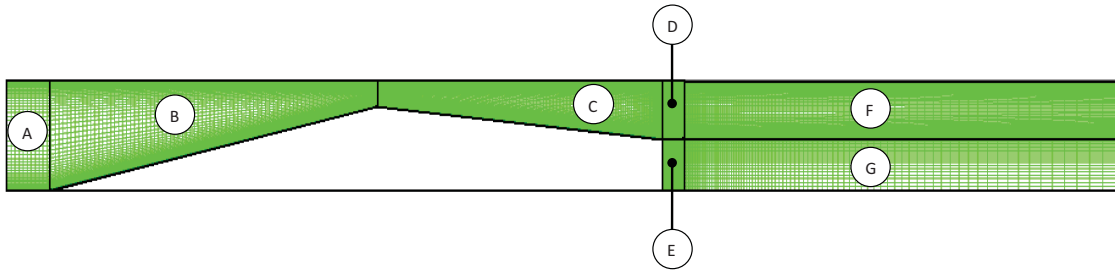


Figure 4.2: Multi-bloc structured mesh topology for 2-D flow

Considering the in-coming velocity of  $V_0 = 1091$  m/s, the corresponding Reynolds is  $1.20 \times 10^8$ . Setting the target is  $\Delta y^+ = 1$  as we are in sublayer. the resulting near wall mesh spacing  $\Delta y$  is  $0.14\mu m$ . Considering  $V_0 = 2027$  m/s, the corresponding

Reynolds number is  $1.83 \times 10^8$  The resulting near wall mesh spacing  $\Delta y$  is  $0.095\mu m$  for the same target  $\Delta y^+$

The boundary layer thickness  $\delta$  can be computed from the correlation:

$$\delta = 0.035 L Re_L^{-0.142} \quad (4.4.2)$$

We can estimate that the thickness of the boundary layer at  $V_0 = 1091 \text{ m/s}$  is  $1.35 \text{ mm}$ , and  $1.298 \text{ mm}$  for  $V_0 = 2027 \text{ m/s}$ . The mesh should have a minimum number of 10 mesh points inside the boundary layer in order the turbulence model work properly.

We note here that these estimations are based on flat plate correlations, where the presence of the shock waves may lead to  $y^+$  to exceed 1000.

A series of structured mesh have been generated, which has the same topology

Table 4.1: Mesh size near the wall

Mesh	A	B	C	D	E	F
$\Delta y$	( $\mu m$ )	( $\mu m$ )	( $\mu m$ )	( $\mu m$ )	( $\mu m$ )	( $\mu m$ )
1	0.14	0.1	0.1	0.3	0.1	0.4
2	0.095	0.09	0.095	0.095	0.1	0.54
3	19	5	10	10	6	10
4	28	6.6	15	15	6	15

as shown in figure (4.2), with near size wall given in table (4.1). The total elements per bloc are given in table (4.2)

Simulations were carried out to determine the adequate mesh for the present study.

From the four mesh presented in table (4.1), it was found that using mesh 1, 2 and

Table 4.2: Mesh size

Mesh	A	B	C	D	E	F	G
1	10000	100000	200000	10000	10000	50000	50000
2	20000	200000	400000	40000	30000	200000	100000
3	5600	33600	67200	11200	5000	56000	25000
4	5000	30000	60000	10000	5000	50000	25000

3 does not offer any numerical solution. Mesh 4 was the only successful one, which will be used for all the simulations.

#### 4.4.2 Wall function

The wall functions are based on the assumption that the first grid point off the wall (or the first integration point) is located in the universal law-of-the-wall or logarithmic region [108]. This allows to avoid the resolution of the very thin viscous sublayer, leading to a reduction of the number of cells and to a more moderate (and desirable) aspect ratio of the cells (ratio of the longest to the smallest side in a structured grid). High aspect ratios can result in numerical problems due to round-off errors. On the other hand, using standard wall function formulations (equation 4.1) are difficult to handle, because it has to be ensured that the grid resolution near the wall satisfies the wall function requirements. If the grid becomes too coarse, the resolution of the boundary layer is no longer ensured. If the resolution becomes too fine, the first grid spacing can be too small to bridge the viscous sublayer. In this case, the logarithmic profile assumptions are no longer satisfied. Therefore we have to ensure that both limits are not overstepped in the grid generation phase. The lower limit on the grid resolution for standard wall functions is a severe detriment to a systematic grid

refinement process, as they are based on physical assumptions which are problematic, especially in flows at lower Reynolds numbers ( $Re < 10^5$ ), as the sublayer portion of the boundary layer is neglected in the mass and momentum balance. For flows at low Reynolds numbers, this can cause an error in the displacement thickness of up to 25%. The standard wall function can be written as follows [125]:

$$u^+ = \frac{U_t}{u_\tau} = \frac{1}{\kappa} \ln(y^+) + C \quad (4.4.3)$$

where

$$y^+ = \frac{\rho \Delta y u_\tau}{\mu} \quad (4.4.4)$$

$$u_\tau = \left(\frac{\tau_w}{\rho}\right)^{1/2} \quad (4.4.5)$$

$u^+$  is the near wall velocity,  $U_t$  is the friction velocity,  $U_t$  is the known velocity tangent to the wall at distance of  $\Delta y$  from the wall,  $y^+$  is the dimensionless distance from the wall,  $\tau_w$  is the wall shear stress,  $\kappa$  is the von Karman constant and  $C$  is a log-layer constant depending on wall roughness.

A hybrid method is developed by Menter [109] for the SST turbulence model which automatically switches from a low-Re formulation to wall functions based on the grid spacing. The SST has the advantage that an analytical expression is known for  $\omega$  in the viscous sublayer, which can be exploited to achieve this goal. The main idea behind the present formulation is to blend the wall value for  $\omega$  between the logarithmic and the near wall formulation. The flux for the k-equation is artificially kept to be zero and the flux in the momentum equation is computed from the velocity profile. The equations are as follows:

- Flux for the momentum equation,  $F_U$ :

$$F_U = -\rho u_\tau u^* \quad (4.4.6)$$

with

$$u_\tau = \sqrt{\nu \left| \frac{\Delta U}{\Delta y} \right|} \quad (4.4.7)$$

and

$$u^* = \max(\sqrt{a_1 k}, u_\tau) \quad (4.4.8)$$

- Flux for the k-equation:

$$F_k = 0 \quad (4.4.9)$$

In the  $\omega$ -equation, an algebraic expression is specified instead of an added flux. It is blend between the analytical expression for  $\omega$  in the logarithmic region:

$$\omega_l = \frac{u^*}{a_1 \kappa y} = \frac{1}{a_1 \kappa y} \frac{u^{*2}}{y^+} \quad (4.4.10)$$

and the corresponding expression in the sublayer:

$$\omega_s = \frac{6\nu}{\beta(\Delta y)^2} \quad (4.4.11)$$

with  $\Delta y$  being the distance between the first and the second mesh point. In order to achieve a smooth blending and avoid cyclic convergence behavior, the following formulation is selected:

$$\omega_\omega = \omega_s \sqrt{1 + \left(\frac{\omega_l}{\omega_s}\right)^2} \quad (4.4.12)$$

while in the wall-function formulation, the first point is treated as being outside the edge of the viscous sublayer, the location of the first mesh point is now virtually

moved down through the viscous sublayer as the mesh is refined in the low- $Re$  mode. It is emphasized, that the physical location of the first mesh point is always at the wall ( $y = 0$ ). The error in the wall-function formulation results from this virtual shift, which amount to a reduction in displacement thickness. This error is always present in the wall-function mode, but is reduced to zero as the method shifts to low- $Re$  model. The shift is based on the distance between the first and the second mesh point  $\Delta y = y_2 - y_1$  with  $y$  being the wall normal distance. This formulation provides the optimal boundary condition for a given grid. This method is the most desirable, as it allow for an accurate near-wall treatment over a wide range of grid spacings. It should however be remembered that the accurate boundary layer simulations do not only depend on the near-wall spacing, but also on the grid nodes inside the boundary layer, for high  $Re$  number  $10^9$  the value of  $y^+$  can safely exceed 1000 [108].

## 4.5 Determining turbulence parameters

### 4.5.1 Turbulence intensity

Turbulence Intensity,  $I$ , is defined as the ratio of the root-mean square of the velocity fluctuations,  $u'$ , to the mean flow velocity,  $u_{avg}$ . as described in section (3.3.2). A turbulence intensity of 1% or less is generally considered low and turbulence intensities greater than 10% are considered high.

Ideally, we can have a good estimate of the turbulence intensity at the inlet boundary from external, measured data. For example, if simulating a wind tunnel experiment, the turbulence intensity in the free stream is usually available from the tunnel characteristics. In modern low-turbulence wind tunnels, the free-stream turbulence intensity

may be as low as 5%. For internal flows, the turbulence intensity at the inlets is totally dependent on the upstream history of the flow.

The turbulence intensity at the core of a fully developed duct flow can be estimated from the following formula derived from an empirical correlation for pipe flows:

$$I \equiv \frac{u'}{u_{avg}} = 0.16(Re_d)^{-1/8} \quad (4.5.1)$$

where,  $d$  is the tube diameter.

According to this formula.

- At  $V_\infty = 1091 \text{ m/s}$ : Reynolds number of  $2.7 \times 10^6$ , the turbulence intensity will be 2.5%
- At  $V_\infty = 1829 \text{ m/s}$ : Reynolds number of  $4.65 \times 10^6$ , the turbulence intensity will be 2.34%
- At  $V_\infty = 2035 \text{ m/s}$ : Reynolds number of  $5.17 \times 10^6$ , the turbulence intensity will be 2.31%

### 4.5.2 Turbulence length scale

The turbulence length scale,  $\ell$ , is a physical quantity related to the size of the large eddies that contain the energy in turbulent flows. In fully-developed duct flows,  $\ell$  is restricted by the size of the duct, since the turbulent eddies cannot be larger than the duct. An approximation can be made using the following formula:

$$\ell = C_\mu \frac{k^{3/2}}{\varepsilon} \quad (4.5.2)$$

This correlation is not necessarily applicable to all situations, however, it is a suitable approximation.

### 4.5.3 Boundary conditions

#### Supersonic inflow condition

In the case of supersonic inflow, there are no outgoing characteristics from the computational domain to the boundary point. Therefore all flow quantities at the boundary are prescribed. Table (4.3) presents the quantity required at the inlet for the corresponding incoming velocity.

#### Supersonic outflow condition

At supersonic outflow, all characteristics from a boundary point leave the computational domain. Therefore, a linear extrapolation is made from the interior cells to the boundaries. Another condition regarding the radiation will be discussed in radiation section.

#### Wall boundary

The flow in the ram accelerator is considered as viscous flow, a no-slip boundary condition is applied on all the walls, and the tube wall has same flow velocity. In the present study, the tube wall is treated as isothermal  $T = T_{wall} = 300K$ , and the projectile walls as adiabatic, and catalytic. Taking into account the radiation effect, the walls were treated as a grey heat sink of emissivity 1. Wall scattering coefficient is taken zero.



Table 4.3: Turbulent intensity and turbulent length scale

V	P	T	I	$\ell$
<i>(m/s)</i>	<i>MPa</i>	<i>K</i>	<i>(%)</i>	<i>(m)</i>
1091	5.15	300	2.5044	$10^{-5}$
1173	5.15	300	2.4818	$10^{-5}$
1247	5.15	300	2.4628	$10^{-5}$
1374	5.15	300	2.4332	$10^{-5}$
1476	5.15	300	2.4116	$10^{-5}$
1519	5.15	300	2.4029	$10^{-5}$
1622	5.15	300	2.3833	$10^{-5}$
1733	5.15	300	2.3636	$10^{-5}$
1829	5.15	300	2.3477	$10^{-5}$
1842	5.15	300	2.3457	$10^{-5}$
1891	5.15	300	2.3379	$10^{-5}$
1917	5.15	300	2.3340	$10^{-5}$
1930	5.15	300	2.3320	$10^{-5}$
1943	5.15	300	2.3300	$10^{-5}$
1957	5.15	300	2.3280	$10^{-5}$
1970	5.15	300	2.3261	$10^{-5}$
1983	5.15	300	2.3242	$10^{-5}$
1995	5.15	300	2.3224	$10^{-5}$
2017	5.15	300	2.3191	$10^{-5}$
2027	5.15	300	2.3177	$10^{-5}$
2035	5.15	300	2.3165	$10^{-5}$

## 4.6 Radiation

Thermal radiation is an important heat transfer mode in most combustion systems. By nature, the rate of radiative heat transfer generally depends on the temperature to the fourth power or higher. This makes thermal radiation dominant over convection in most flames, especially when soot particles are present. In addition, radiation exerts its effects at a distance and allows energy to travel directly from the hot product regions to cold regions such as the reactant mixture and the surroundings. Accurate descriptions of radiative heat transfer is a crucial element in simulations of turbulent combustion systems. The same reasons that make thermal radiation important in flames also make its calculation complicated. Since radiation is a long-range phenomenon, conservation of energy must be applied over the entire domain under consideration instead of an infinitesimal volume as for mass and momentum conservation. This leads to an integral equation containing up to seven independent variables: the frequency of radiation, three space coordinates, two coordinates describing the direction of radiation, and time. Furthermore, radiative properties of combustion products are usually difficult to measure and often display erratic behavior with wavelength and temperature. Because of these difficulties, most combustion simulations ignore the effect of radiative heat loss, or treat it in an ad hoc or overly simplistic manner.

Inadequate treatment of radiation can cause large errors in determining flame structure and pollutant emission. For example, the prediction of NO<sub>x</sub> emission is very

sensitive to the predicted flame temperature distribution, which is influenced significantly by the radiation model. Soot and radiation are highly coupled processes. Errors in temperature predictions will over- or under-predict soot formation and oxidation rates and therefore soot yields, which will in turn result in erroneous radiative heat losses. Detailed description of radiative energy transfer is therefore essential to a successful comprehensive modeling of turbulent combustion processes. Radiative heat transfer from a flame can be predicted in principle if the radiative properties and temperature distributions in the flame are available. However, flame temperature is an unknown variable that is solved for in flame simulations. As a result, the calculation of radiative heat transfer is coupled to the energy equation through a heat source term. This radiative heat source can be expressed as the divergence of the radiative heat flux,  $q_r$ .

The radiative transfer equation is an integro-differential equation for spectral radiative intensity in five independent variables: three space coordinates and two directional coordinates with local origin. The problem becomes even more complicated if the medium is nongray, which introduces the additional spectral variable, and if the geometry of the participating medium enclosure is irregular. Consequently, exact analytical solutions exist for only a few extremely simple situations: for example, a one-dimensional plane-parallel gray medium that is either at radiative equilibrium (radiation is the only mode of heat transfer) or whose temperature field is known. Even for these simplest cases, the exact solution can only be written implicitly in the form of an integral equation [126]. For most combustion systems, the problems are multi-dimensional and nonhomogeneous, and the spectral variations of the radiative

properties frequently have to be accounted for. Therefore simplifying approximations are necessary in the solution of the radiative transfer equation (RTE). There is no single model or approximation that is universal and can be applied to all different types of practical problems. Depending on the nature of the combustion system, characteristics of the flame, the solution techniques used for other governing equations, the degree of accuracy required, and the available computer facilities, solution methods of varying degrees of approximation have been devised. The majority of the methods that have been used in combustion simulations fall into one of the five groups: (1) optically thin approximations; (2) spherical harmonic methods; (3) discrete ordinate methods; (4) zonal methods; and (5) statistical methods. There are also hybrid methods that combine the features of several different methods. Detailed discussions and references can be found in, e.g. [126], [127].

Although there are several radiative transfer models available, it is difficult to choose a "best" model for different applications. For a given physical situation, one of the several models can be used according to the applicability of the model, desired accuracy and computational costs. In order to decide whether a model is appropriate for a given problem, one has to compare its predictions against the benchmark results obtained from either experiments or exact solutions. Spherical Harmonic Method method is extensively used as the benchmark for comparisons as they generally yield accurate predictions of radiation heat transfer even for complicated geometries, and the CPU demand is relatively low.

### 4.6.1 Spherical harmonic method

The spherical harmonic method, also known as the P-N method or differential method, is based on the idea that the solution of the RTE can be simplified by expressing the radiative intensity as a series of products of angular (directional) and spatial functions [126]. The angular dependence is represented using spherical harmonics, which satisfy Laplace's equation in spherical coordinates, and the spatial functions then are solved.

The solution is facilitated by the orthogonality of spherical harmonics. The number of terms retained in the series expansion gives the method its order and its name: for example, the P1 or the P3 approximation. It is known from neutron transport theory that approximations of odd order are more accurate than approximations of the next higher even order, so that the P2 approximation is never used. The spherical harmonic method is mathematically elegant. It transforms the RTE into a set of simultaneous partial differential equations that are similar in structure to the other pde's that must be solved for a chemically reacting flow. The drawback of the method is that the accuracy improves slowly for higher-order approximations while mathematical complexity increases extremely rapidly, and the low-order approximations are only accurate in media with near-isotropic radiative intensity. Still, the P1 approximation is used widely in combustion simulations.

#### **The P-1 Radiation Model**

The P-1 radiation model is the simplest case of the more general P-N model, which is based on the expansion of the radiation intensity  $I$  into an orthogonal series of

spherical harmonics [126]. The following equation is used for the radiation flux  $q_r$ :

$$q_r = -\frac{1}{3(a + \sigma_s) - C\sigma_s} \nabla G \quad (4.6.1)$$

where  $a$  is the absorption coefficient,  $\sigma_s$  is the scattering coefficient,  $G$  is the incident radiation, and  $C$  is the linear-anisotropic phase function coefficient, described below.

After introducing the parameter

$$\Gamma = \frac{1}{3(a + \sigma_s) - C\sigma_s} \quad (4.6.2)$$

Equation (4.6.1) simplifies to:

$$q_r = \Gamma \nabla G \quad (4.6.3)$$

the transport equation for  $G$  is:

$$\nabla(\Gamma \nabla G) - aG + 4a\sigma T^4 = S_G \quad (4.6.4)$$

where  $\sigma$  is the Stefan-Boltzmann constant and  $S_G$  is a source term. This equation determines the local radiation intensity when the P1 model is active, combining equations (4.6.3) and (4.6.4) we obtain the following equation:

$$-\nabla q_r = aG - 4a\sigma T^4 \quad (4.6.5)$$

The expression for  $-\nabla q_r$  can be directly substituted into the energy equation to account for heat source ( or sinks) due radiation.

## 4.6.2 Boundary condition treatment for the P-1 model at walls

To get the boundary condition for the incident radiation equation, the dot product of the outward normal vector  $\vec{n}$  and equation (4.6.3) becomes:

$$q_r \cdot \vec{n} = -\Gamma \nabla G \cdot \vec{n} \quad (4.6.6)$$

$$q_{r,w} = -\Gamma \frac{\partial G}{\partial n} \quad (4.6.7)$$

Thus the flux of the incident radiation,  $G$ , at a wall is  $-q_{r,w}$ . The wall radiative heat flux is computed using the following boundary condition:

$$I_w(\vec{r}, \vec{s}) = f_w(\vec{r}, \vec{s}) \quad (4.6.8)$$

$$f_w(\vec{r}, \vec{s}) = \epsilon_w \frac{\sigma T_w^4}{\pi} + \rho_w I(\vec{r}, \vec{s}) \quad (4.6.9)$$

where  $\rho_w$  is the wall reflectivity. The Marshak boundary condition [128] is then used to eliminate the angular dependence:

$$\int_0^{2\pi} I_w(\vec{r}, \vec{s}) \vec{n} \cdot \vec{s} d\Omega = \int_0^{2\pi} f_w(\vec{r}, \vec{s}) \vec{n} \cdot \vec{s} d\Omega \quad (4.6.10)$$

Substituting equations (4.6.8)(4.6.9) in (4.6.10), and performing the integration yields

$$q_{r,w} = -\frac{4\pi\epsilon_w \frac{\sigma T_w^4}{\pi} - (1 - \rho_w)G_w}{2(1 + \rho_w)} \quad (4.6.11)$$

If it is assumed that the wall are diffuse gray surface, then  $\rho_w = 1 - \epsilon_w$ , and equation (4.6.11) becomes

$$q_{r,w} = -\frac{\epsilon_w}{2(2 - \epsilon_w)} (4\sigma T_w^4 - G_w) \quad (4.6.12)$$

Equation (4.6.12) is used to compute  $q_{r,w}$  for the energy equation and for the incident radiation equation boundary conditions.

### Boundary Condition Treatment for the P-1 Model at Flow Inlets and Exits

The net radiative heat flux at flow inlet and outlet is compared in the same manner as at walls. It is assumed that the emissivity of the inlet and outlet is 1.0 (black body absorption) [129].

## 4.7 Combustion setup

The implementation of a detailed chemical kinetics mechanism in the flow calculations is very demanding in terms of computational resources, as the memory and the CPU time consumption depend primarily on the number of chemical species included in the reaction system [72]. So far, there is no universal kinetics mechanism, especially at high pressure (i.e., greater than 1MPa), and the implementation of the mechanism is largely affected by uncertainties in the thermodynamic, transport, and chemical kinetic properties of these species. The propellant being considered here is  $2.95CH_4 + 2O_2 + 5.7N_2$  at 5.15MPa fill pressure. Because there is a lack of specific data for chemical kinetics rates for this propellant at combustion pressures greater than 5.0MPa, modifications to ideal gas mechanisms have been developed, including intermediate reactions steps for ram accelerator applications. The global reaction mechanism for methane-air chemistry (neglecting some intermediate reaction steps) proposed by Westbrook [72], and Peterson [87], [130] has previously been used for ram accelerator combustion calculations carried out by Nusca and others [131],[90], [88]. [87], [130]

### 4.7.1 Reaction mechanism

#### One step reaction

The one-step reaction can be written as:

$$\dot{\omega}_{arrhenius} = AT^\beta \text{Exp}\left(\frac{-E_a}{\Re T}\right) \sigma_{CH_4}^a \sigma_{O_2}^b \sigma_{CO_2}^c \sigma_{H_2O}^d \quad (4.7.1)$$





where the  $AT^\beta$  is the collision frequency,  $T$  is the temperature, the exponent  $\beta$  is the Boltzmann factor,  $E_a$  is the activation energy with unit of Kcal/mole,  $A$  is in  $(cm^3.mole.s - 1)$  and gas constant  $R = 1.987$  cal/mole-K, the  $\sigma$  is the species mass fraction, and the coefficients  $a, b, c, d, e, f$  are the degrees of reaction for each species. Note that the exponent  $\beta = 0$  for this mechanism.

Table 4.4: Reaction rate equation data, one step

Reaction	$E_a$	A	a	b	c	d
Eq.(4.7.2)	30	$8.3 \times 10^6$	-0.3	1.3	1	1

### Two steps reaction

$$\dot{\omega}_{arrhenius} = AT^\beta \text{Exp}\left(\frac{-E_a}{\mathfrak{R}T}\right) \sigma_{CH_4}^a \sigma_{O_2}^b \sigma_{CO}^c \sigma_{CO_2}^d \sigma_{H_2O}^e \quad (4.7.3)$$

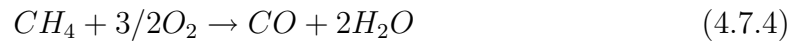


Table 4.5: Reaction rate equation data, two steps

Reaction	$E_a$	A	a	b	c	d	e
Eq.(4.7.4)	30	$1.5 \times 10^7$	-0.3	1.3	1	0	1
Eq.(4.7.5)	40	$3.9 \times 10^{14}$	0	0.25	1	1	0

### Five steps reaction

$$\dot{\omega}_{arrhenius} = AT^\beta \text{Exp}\left(\frac{-E_a}{\mathfrak{R}T}\right) \sigma_{CH_4}^a \sigma_{O_2}^b \sigma_{CO}^c \sigma_{H_2}^d \sigma_{CO_2}^e \sigma_{H_2O}^f \quad (4.7.6)$$

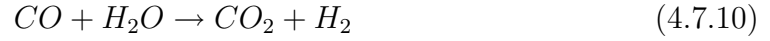
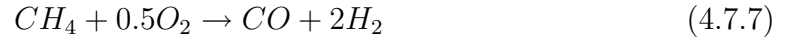


Table 4.6: Reaction rate equation data, five steps

Reaction	$E_a$	A	a	b	c	d	e	f
Eq.(4.7.7)	30	$2.3 \times 10^7$	-0.3	1.3	1	1	0	0
Eq.(4.7.8)	37.6	$1 \times 10^5$	0	0.5	0	1	0	1
Eq.(4.7.9)	40	$3.5 \times 10^{14}$	0	0.25	1	0	1	0
Eq.(4.7.10)	$\dot{\omega}_4$	-	0	0	1	1	1	1
Eq.(4.7.11)	$\dot{\omega}_5$	-	0	0	1	1	1	1

$$\dot{\omega}_4 = \frac{X_{CO}}{W_{CO}} \times X_{H_2O} \times P_{abs}^2 \times 8.1 \cdot 10^{-9} \times \exp\left(\frac{-10926.5}{T}\right) \quad (4.7.12)$$

$$\dot{\omega}_5 = \frac{X_{CO_2}}{W_{CO}} \times X_{H_2} \times P_{abs}^2 \times 3.3 \cdot 10^{-7} \times \exp\left(\frac{-15144}{T}\right) \quad (4.7.13)$$

## 4.8 Flame radiation losses

The determination of the Planck-mean absorption coefficient takes into account the effect of the gas band radiation. For gas band radiation,  $CO_2$  and  $H_2O$  are the most important radiating species in hydrocarbon flames.  $CO$  and  $CH_4$  contribute much less to the flame temperature reduction than do  $CO_2$  and  $H_2O$ . However, considering all four species in a radiation model is suggested [132]. The Planck coefficients for methane ( $CH_4$ ), water ( $H_2O$ ), carbon monoxide ( $CO$ ) and carbon dioxide ( $CO_2$ ) were taken from the RADCAL program of Grosshandler [133].

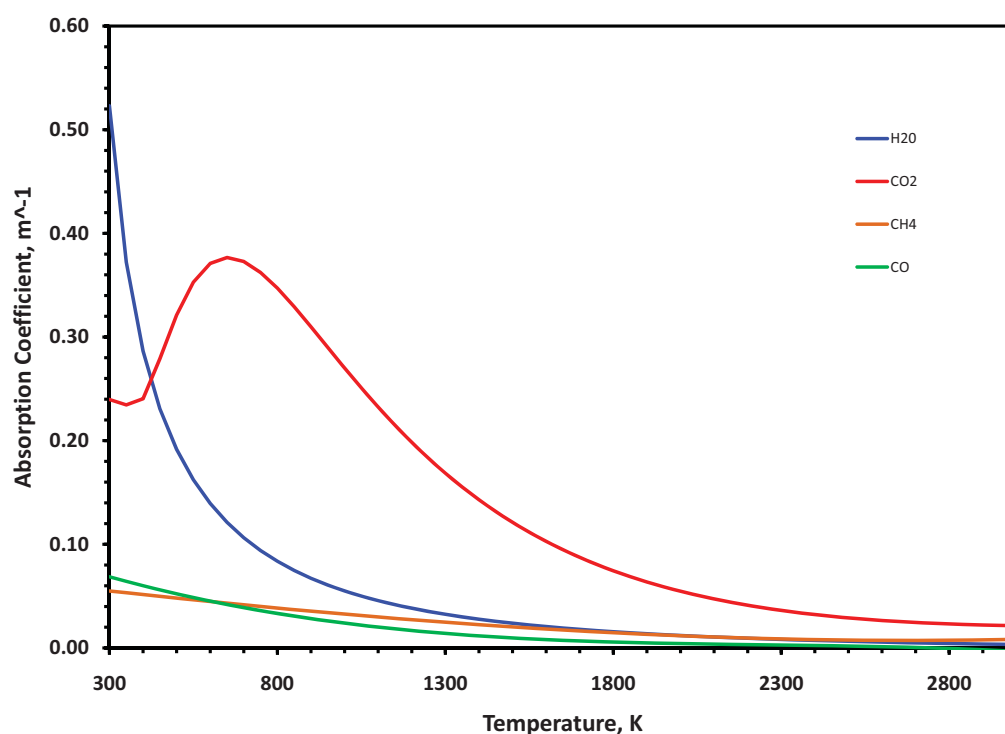


Figure 4.3: Planck mean absorption coefficient for  $CO_2$ ,  $H_2O$ ,  $CH_4$  and  $CO$  as function of gas temperature [133]

## 4.9 Initialization

The initial guess values for the turbulent kinematic Energy, turbulent eddy dissipation, and turbulent eddy frequency will be calculated by using the following formulas [108]:

$$k = \frac{3}{2}(U_{ave}.I)^2 \quad (4.9.1)$$

$$\varepsilon = C_{\mu}^{3/4} \cdot \left(\frac{k^{3/2}}{\ell}\right) \quad (4.9.2)$$

$$\omega = \frac{k^{1/2}}{C_{\mu}^{1/4} \cdot \ell} \quad (4.9.3)$$

## 4.10 Summary

Details about the modeling and the computational procedure have been presented. The simulation solves two dimensional axis-symmetric compressible Reynolds-averaged Navier-Stokes (RANS) equations along with the SST turbulence model for turbulent viscous effect, the EDM model for turbulent combustion, and the P-1 radiation model for the heat losses. Due to high accuracy required for capturing the shock waves, second order Total Variation Diminishing (TVD) scheme is used. Simulations will be carried out for a series of incoming Mach number between  $M = 2.98$  to  $M = 5.5$ . Different chemical kinetic mechanisms have been presented; i.e., one-step, two-step and five-step reaction, the approach for including thermal radiation was also presented and the choice of the radiation model was discussed. The solution will be started with a precursor non-reactive computation until a steady-state convergence status, followed by the main reactive computation. Results from the modeling will be validated against the experimental data derived from the University of Washington facility.

# Chapter 5

## Results and discussion

### 5.1 Introduction

Computational fluid dynamics solutions of the Reynolds Averaged Navier-Stokes (RANS) equations have been used to numerically predict the ram accelerator performance in the thermally choked propulsive mode. Simulations were carried out for a series of incoming velocities. The shear-stress transport turbulence model (SST) and the eddy dissipation combustion model (EDM) have been used. Different chemical kinetics mechanism were investigated and it turns out that the five steps reaction mechanism with 6 species predicted the thrust in good agreement with the experimental data. The effect of the thermal radiation on the flame temperature has been investigated. The spherical harmonic P-1 model was used and the Planck-mean absorption coefficients were used to determine the radiative properties of the species as a function of the temperature. The solution starts with a precursor non-reactive computation until a steady-state convergence status, the results will then be used as initial values for the main reactive computation. The SST turbulence model constants were used as originally introduced by Menter [109], and the two constants A and B for

the eddy dissipation combustion model are taken 4 and -1 consecutively. Second order Total Variation Diminishing (TVD) scheme is used due to high accuracy required for capturing the shock waves [123], [124]. Results from the simulation were compared against the experimental data for the pressure and thrust derived from the University of Washington 38-mm-bore facility. Note that the experimental data is used for the first time here. The pressure profile agreed very well with the experimental data in the thermally choked propulsive mode, between Mach number ( $M_0 = 2.98$ ) and ( $M_0 = 4.4$ ). The predicted thrust in the thermally choked propulsive mode agreed well with the experimental data and the velocity for which the thrust is zero was obtained from the CFD modeling. Pressure, Temperature and Mach number contours will be plotted for all the simulations.

## 5.2 The influence of the reactional mechanism

Simulations for Mach number  $M_0 = 4.98$  ( $V_0 = 1829 \text{ m/s}$ ) were carried out to investigate the chemical reaction mechanism on the simulation. The results show that by using one global step reaction and two steps reaction mechanism, the flame temperature is much higher than those derived from simulations using five steps reaction mechanism. Similar results have been found when using one global step reaction and two steps reaction mechanism for the methane/oxygen mixture by Westbrook [72].

figure (5.1) presents the temperature profiles on the projectile body and the center line up to the exit domain. It also shows that all the reaction systems predict the same temperature around the projectile up to 0.16 m. The temperature solution

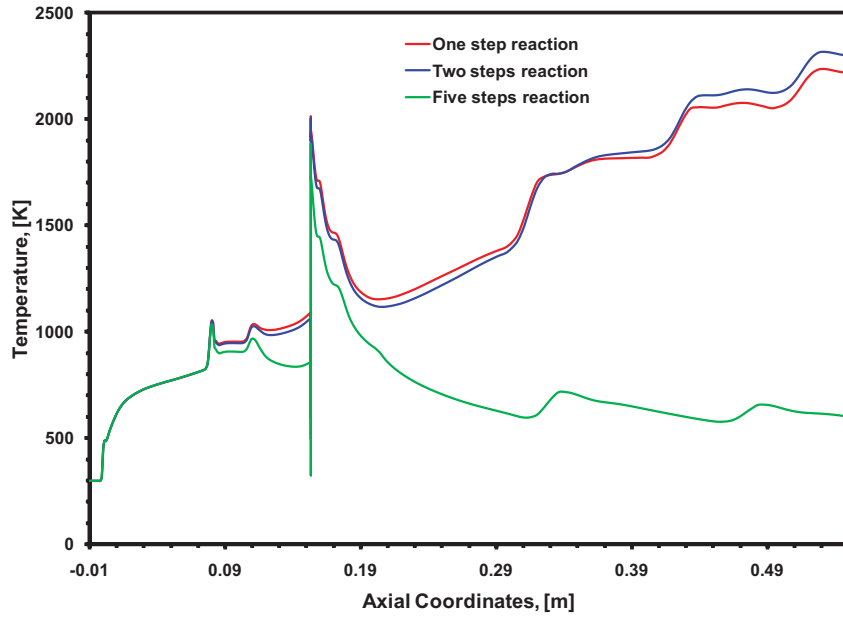


Figure 5.1: Temperature profiles on the projectile body and the center line, using one, two, and five steps reaction mechanism, in-coming velocity  $V_0 = 1829 \text{ m/s}$

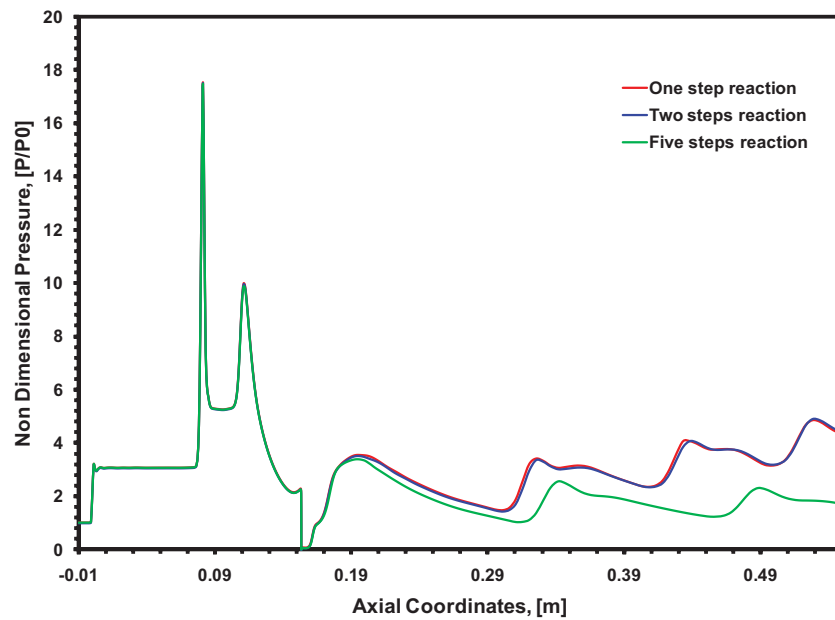


Figure 5.2: Pressure profiles on the projectile body and the center line, using one, two, and five steps reaction mechanism, in-coming velocity  $V_0 = 1829 \text{ m/s}$

derived from one and two steps reaction starts to increase up to the exit of the flow, whereas the results from five steps reaction mechanism decrease from 1900K at the base of the projectile to about 700K at the exit of the domain. This means that the reaction zone is at the base of the projectile and the results match the experimental data, where the reaction zone length was observed to be about the size of the diameter of the ram accelerator. Similar results were obtained for the pressure as seen in figure 5.2. It is shown that the pressure results in the far field of the domain from one and two steps reaction mechanism are 80% higher than the results obtained from using five steps reaction mechanism.

Table (5.1) presents the maximum pressure and temperature recorded in the domain, for the in-coming velocity  $V_0 = 1829 \text{ m/s}$  using one global step reaction, two, and five steps chemical reaction mechanism, including the thermal radiation in the modeling. The results show that using five steps reaction mechanism enhances the results for the temperature, where the temperature decreased by 337K compared to one step, and 418K compared to two steps.

Table 5.1: Maximum Pressure & Temperature, in-coming velocity  $V_0 = 1829 \text{ m/s}$

Reaction mechanism	Temperature (T)	Non-Dimensional Pressure
1 step	2234	17.52
2 steps	2315	17.51
5 steps	1898	17.48
1 Dimensional	1722	15.30



The results from five steps reaction mechanism have been compared to one-dimensional model Temperature and pressure using TARAM program for the same conditions. The results show a difference of 175K and 11MPa in temperature and pressure consecutively. The influence of the radiation on the combustion in the ram accelerator was investigated. The results show that including the radiation in the modeling will decrease the maximum temperature as seen in Table (5.2), where the maximum temperature dropped by 29K, and no variation in the maximum pressure was observed.

Table 5.2: Radiation effects, in-coming velocity  $V_0 = 1829 \text{ m/s}$

Reaction mechanism	Temperature (K)	Non-Dimensional Pressure
5 steps without radiation	1927	17.48
5 steps with radiation	1898	17.48

Table (5.3) presents the calculated thrust at in-coming velocity  $V_0 = 1829 \text{ m/s}$  using one global step reaction, two and five steps chemical reaction mechanism. The results were compared against the experimental data and show that the calculated thrust using one global steps reaction is high at about 80% compared to the experimental measurement. The same results was obtained by using two steps chemical reaction mechanism. The best agreement with the experimental data was obtained by using five steps reaction mechanism including the thermal radiation model in the calculations. Based on the results and the validation with the experimental data, we decided to use the five steps reaction mechanism, taking into account the effects of radiation on the modeling.

Table 5.3: Thrust, in-coming velocity  $V_0 = 1829 \text{ m/s}$ 

Reaction mechanism	Thrust (KN)
1 step	10.85
2 steps	10.30
5 steps without radiation	4.39
5 steps with radiation	4.93
Experimental	6.07

### 5.3 Comparison with the experimental data

Non-reactive simulations were performed for a range of in-coming velocities: 1091, 1173, 1247, 1374, 1476, 1519, 1622, 1733, 1829, 1842, 1891, 1901, 1904, 1917, 1930, 1947, 1957, 1970, 1983, 1995, 2007, 2017, 2027, and 2035  $m/s$ . The converged solutions were then used as initial solutions for the main reactive computations. The predicted tube wall pressure for different in-coming Mach numbers were compared to the experimental data recorded at different position, P3, P5, P11, P6, P8, P10, P15, P18, P21, P23, P26, P30, P34, P36, P38, P40. Table (5.4) shows the position and the recorded projectile velocity at these points. The recorded pressure at these locations presents the successful operation of the thermally choked combustion mode, where the high pressure is located at the base of the projectile. For the pressure comparison, the reference  $x = 0$ , was taken at the nose tip of the projectile.

figure (5.3) and figure (5.4), presents the pressure profiles on the tube wall for the for in-coming velocities  $V_0$  of: 1091, 1120, 1150, 1173, 1200, and 1247  $m/s$ . The predicted pressure peaks are observed in similar locations in comparison with data

Table 5.4: Pressure tracers position

Station	X (mm)	V(m/s)
P1	200	1091
P2	600	1173
P3	1000	1240
P4	1400	1314
P5	1800	1380
P6	2198	1430
P7	2598	1476
P8	2998	1520
P9	3398	1557
P10	3798	1590
P11	4196	1630
P12	4596	1649
P13	4996	1673
P14	5396	1695
P15	5796	1720
P16	6194	1740
P17	6594	1749
P18	6994	1760
P19	7394	1771
P20	7794	1785
P21	8192	1798
P22	8592	1805
P23	8992	1829
P24	9392	1842
P25	9792	1854
P26	10190	1866
P27	10590	1878
P28	10990	1891
P29	11390	1904
P30	11790	1917
P31	12188	1930
P32	12588	1943
P33	12988	1957
P34	13388	1970
P35	13788	1983
P36	14186	1995
P37	14586	2007
P38	14986	2020
P39	15386	2027
P40	15786	2035

measured at P3, projectile velocity of  $V = 1240 \text{ m/s}$ . Good comparison was observed in the far field behind the projectile base.

The normal shock position on the projectile after-body changes position as function of the incoming velocity; i.e,  $x \approx 0.16 \text{ m}$  at in-coming velocity of  $V_0 = 1091 \text{ m/s}$  to  $x \approx 0.15 \text{ m}$  at  $V_0 = 1150 \text{ m/s}$ , then recede back to almost  $x = 0.16 \text{ m}$  at  $V_0 = 1200 \text{ m/s}$ . These positions will be more accurate when including the guiding fins in the modeling, where previous works [98] attempted to predict the performance of the ram accelerator in the sub-detonative propulsion mode. Results showed that the position of the normal shock is strongly affected by the presence of the guiding fins.

figure (5.5) presents the pressure profiles on the tube wall for in-coming velocity  $V_0$  of: 1374, and 1400  $\text{m/s}$ . The trend in pressure magnitude is similar for computation and experimental data for P5. The fluctuation observed in the experiments between  $x = 0.1 \text{ m}$  and  $x = 0.16 \text{ m}$  does not appear in our modeling. This maybe due to the three nature of the flow around the projectile, which is not considered in this modeling.

figure (5.6) presents the pressure profiles on the tube wall for in-coming velocity  $V_0$  of: 1476  $\text{m/s}$ . The pressure magnitude in the far field behind the projectile base ( $x = 0.153 \text{ m}$ ) agreed well with measurements for the recorded data at P6, P8. The location and position of the normal shock is in better agreement with P6.

figure (5.7) presents the pressure profiles on the tube wall for in-coming velocity  $V_0$  of: 1520  $m/s$ . The simulation accurately predicts the magnitude of the peak pressures behind the projectile base ( $x = 0.19 m$ ). Overall, the pressure from the CFD in the far field have the same magnitude compared to P8 and P10.

figure (5.8) presents the pressure profiles on the tube wall for in-coming velocity  $V_0$  of: 1622  $m/s$ . At this in-coming velocity, the best comparison experimental data is P10, where the positions of the pressures peaks are similar, and the decay in the magnitude behind the projectile is similar as in the experiment.

figure (5.9) and (5.10) presents the pressure profiles on the tube wall for in-coming velocity  $V_0$  of: 1733, 2017, and 2035  $m/s$ . The pressure from the simulations were compared to the experimental data recorded at projectile having velocities  $V = 1720$ , 1740, and 2020  $m/s$ . In general, the CFD modeling failed to predict the pressure in the trans-detonative propulsion regime. This discrepancy may due to the fact that our modeling did not consider the 3D nature of the flow in the ram accelerator, where the shocks interaction resulting from the fins are neglected here.

figure 5.11 (*top*) presents the pressure field map obtained from from the CFD modeling, the results for pressure form all the simulations have been plotted in 3D format. The results have been compared to experimental data figure 5.11 (*bottom*). Results show good agreement with the experimental data when the projectile remains in thermally choked propulsive mode up to the point where the projectile velocity approaches the CJ velocity. The maximum recorded pressures seen in red have been

predicted at the exact position and magnitude. Overall, the far field pressure has the same magnitude as seen in the experiments. At a velocity of  $1622\text{ m/s}$  the CFD calculation predicts the exact pressure and magnitude.

Simulation at a velocity of  $1733\text{ m/s}$  under-predicts the pressure, where the projectile is making a transition from subdetonative to superdetonative propulsion regime. Our modeling did not perform in transdetonative propulsive mode, this may be due to the turbulence parameters settings at  $M \approx 5$ , also, the actual simulation does not account for the three nature of the flow, due to the missing of the fins in the modeling. More details about the flow field in the combustion region can be seen in figure (5.12). It can be seen that the normal shock from the numerical simulation tends to move back on the projectile body by increasing the velocity.

figure (5.13) presents pressure contours for in-coming velocity  $V_0 = 1091\text{ m/s}$ . High pressure resulting from combustion is observed at the base of the projectile and it tends to decrease away from the base of the projectile. This shows the successful prediction of the thermally choked combustion. At  $V_0 = 1173\text{ m/s}$  the normal shock at the tube wall moves back towards the base of the projectile, and keeps moving until it becomes a oblique shock at  $V_0 = 1519\text{ m/s}$ , see figures; (5.14) to (5.18). At  $V_0 = 1622\text{ m/s}$  high pressure is located at  $x = 300\text{ mm}$  behind the projectile, figure (5.19). Same pressure pattern is observed at incoming velocities from  $V_0 = 1829\text{ m/s}$  to  $V_0 = 2035\text{ m/s}$  where the maximum pressure is at the throat area. See figure (5.21) to (5.32), the scale has been changed for better presentation.

figure (5.33) shows the temperature contours for in-coming velocity  $V_0 = 1091 m/s$ . Fully turbulent structures are observed in the combustion zone. It can be seen that the combustion ignited at the shock wave/boundary layer interaction at the end of the projectile afterbody. Previous works by Choi showed [97] that the shock wave/boundary layer interaction is considered as an ignition mechanism in the ram accelerator and the separation regions located behind the oblique shock are considered as flame holder [95]. The maximum flame temperature varies with the in-coming velocities, at  $V_0 = 1091 m/s$  the flame temperature was  $T_f = 1950K$ , see figure (5.33). It then keeps increasing up to  $T_f = 2308K$  at  $V_0 = 1622 m/s$  ( $M_0 = 4.4$ ), see figure (5.39), then it becomes almost constant around at  $T_f = 1900K$  between  $V_0 = 1829 m/s$  and  $V_0 = 2035 m/s$  figure (5.41) to figure (5.52).

figure (5.53) to figure (5.72) presents the Mach number contours for all the simulations. The supersonic flow upstream was decelerated by train of shocks around the projectile body. The flow field becomes subsonic at the base of the projectile and tends to accelerate in the far field of the domain to become supersonic again. The subsonic flow region seems to decrease as the Mach number increases. At in-coming velocities  $V_0=1829 m/s$  to  $V_0=2035 m/s$ , the same flow pattern was observed in the far field region and the subsonic flow region is located at the base of the projectile and , see figure (5.61) to figure (5.72)

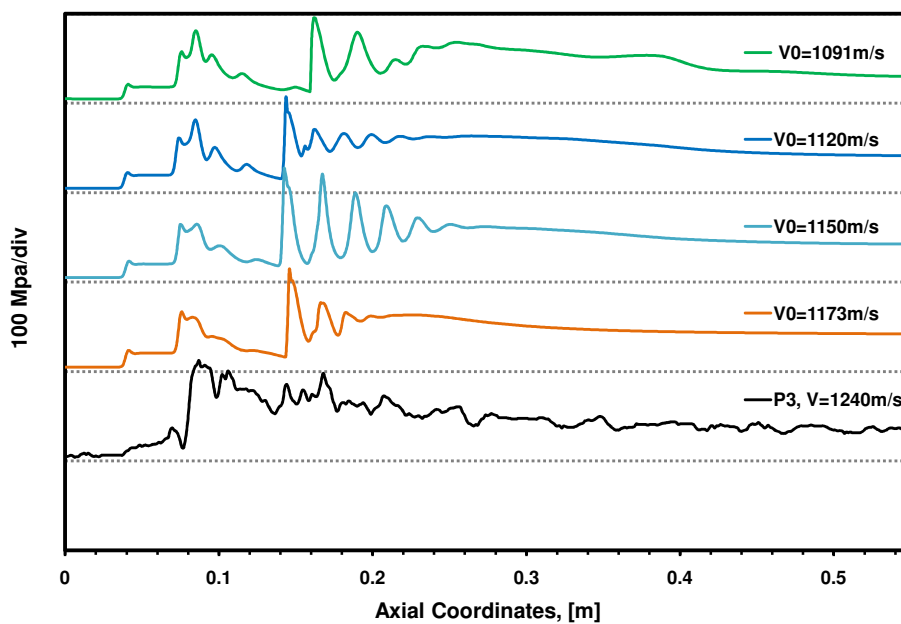


Figure 5.3: Pressure profiles on the tube wall, Experimental velocity= $1240$  m/s

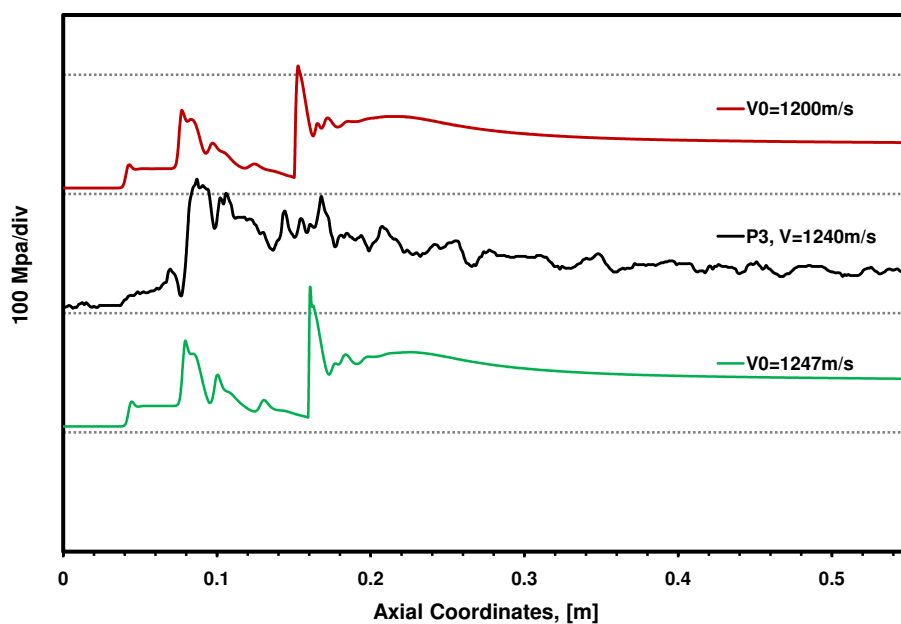


Figure 5.4: Pressure profiles on the tube wall, Experimental velocity= $1240$  m/s



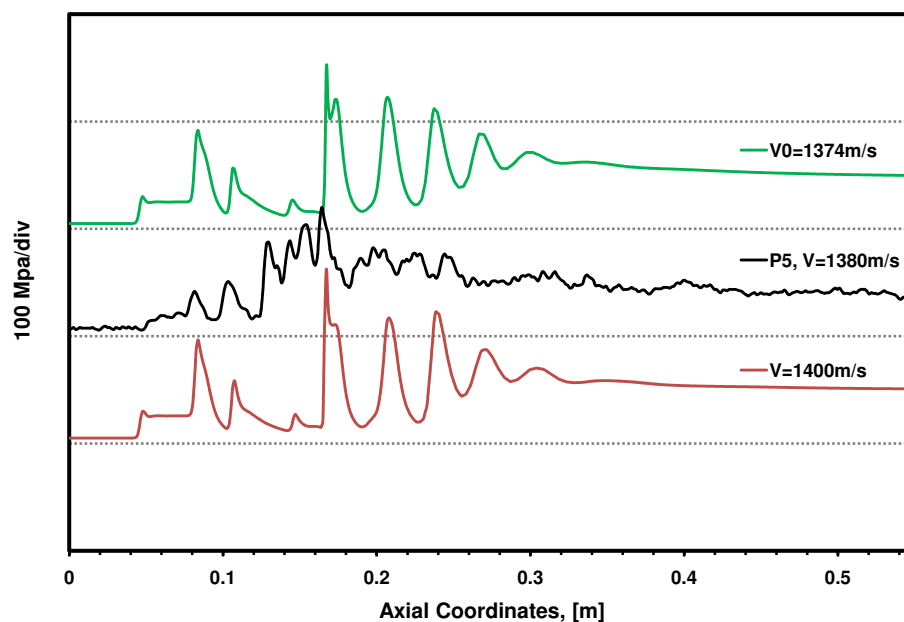


Figure 5.5: Pressure profiles on the tube wall, Experimental velocity= $1370\text{m/s}$

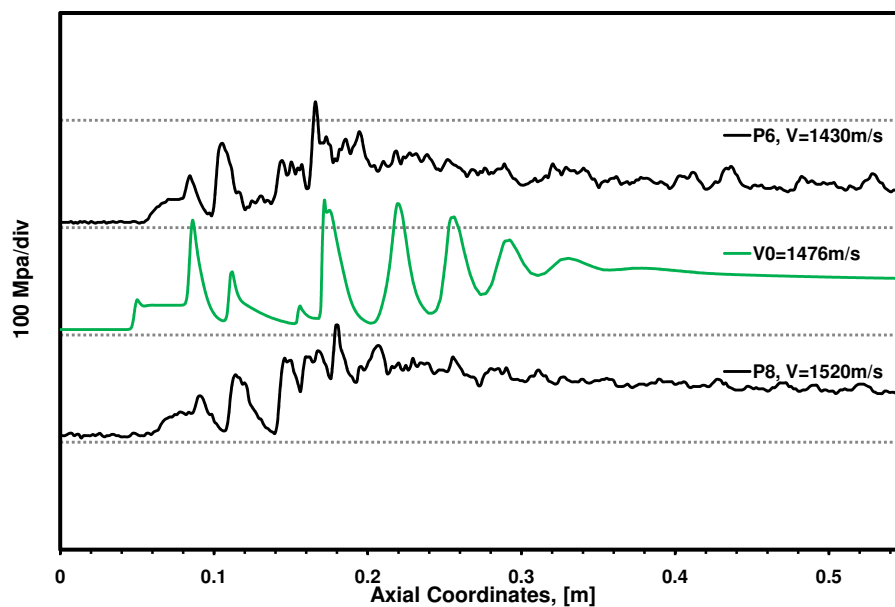


Figure 5.6: Pressure profiles on the tube wall, Experimental velocity;  $P6=1470\text{m/s}$ ,  $P8=1520\text{m/s}$

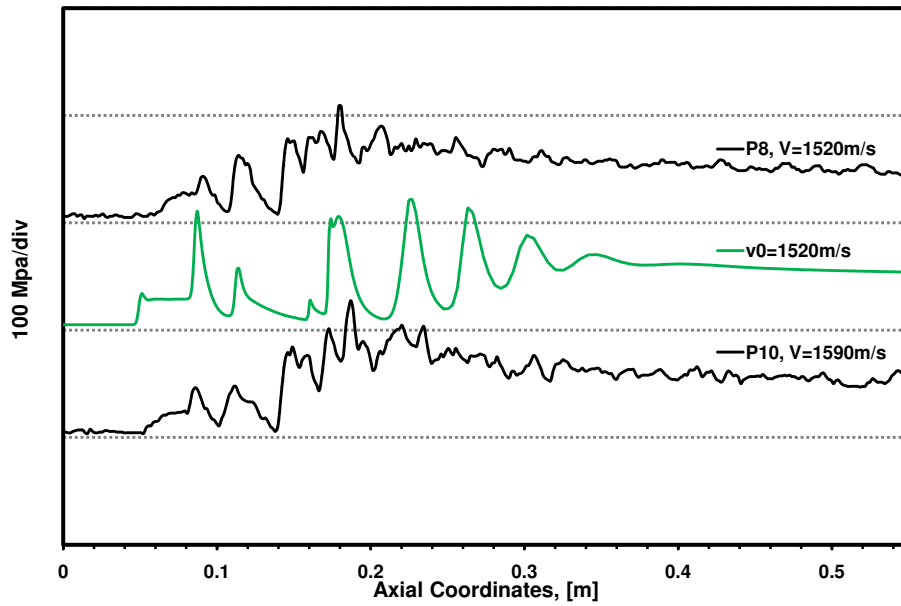


Figure 5.7: Pressure profiles on the tube wall, Experimental velocity; P8=1520m/s, P10=1590m/s

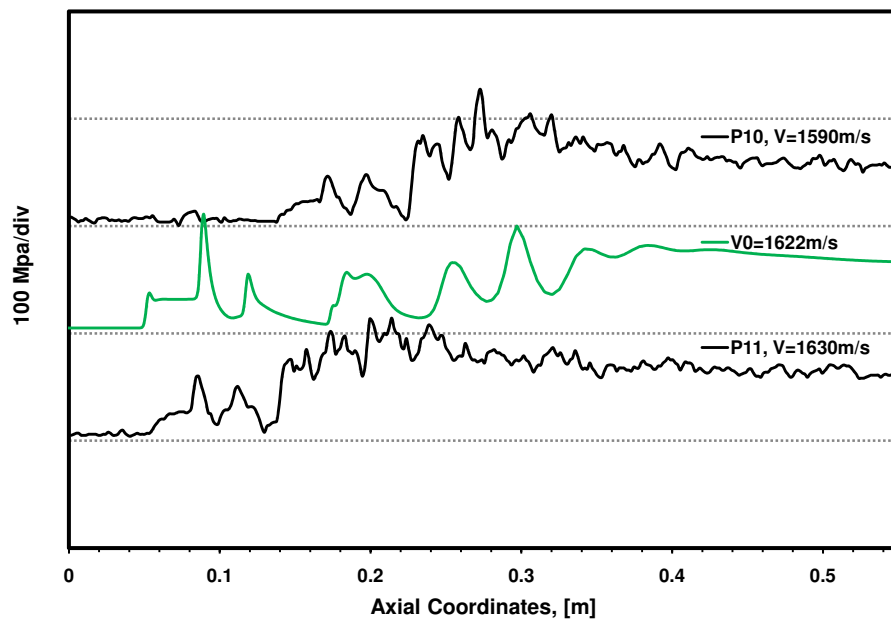


Figure 5.8: Pressure profiles on the tube wall, Experimental velocity; P10=1590m/s, P11=1620m/s

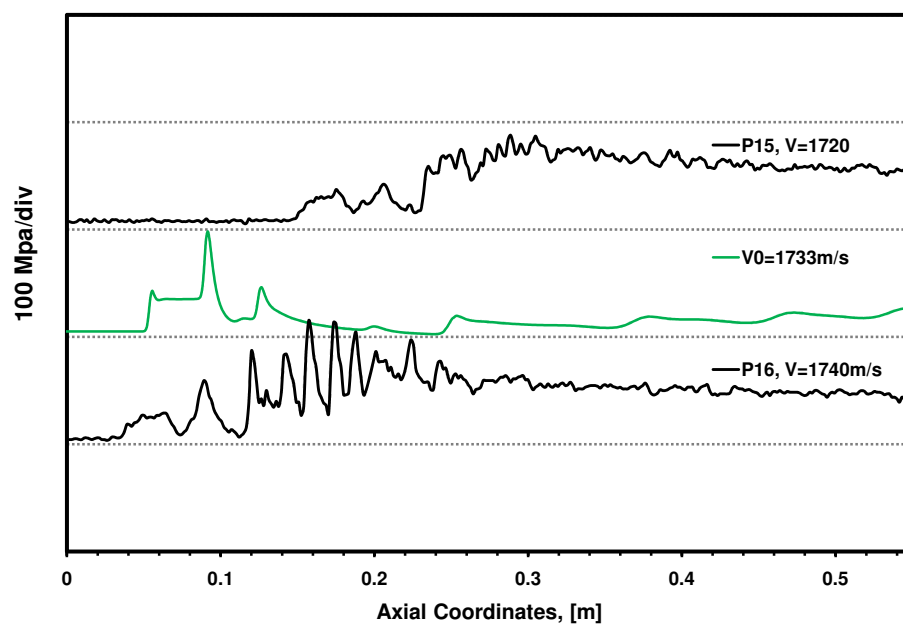


Figure 5.9: Pressure profiles on the tube wall, Experimental velocity; P15=1710m/s, P16=1740m/s

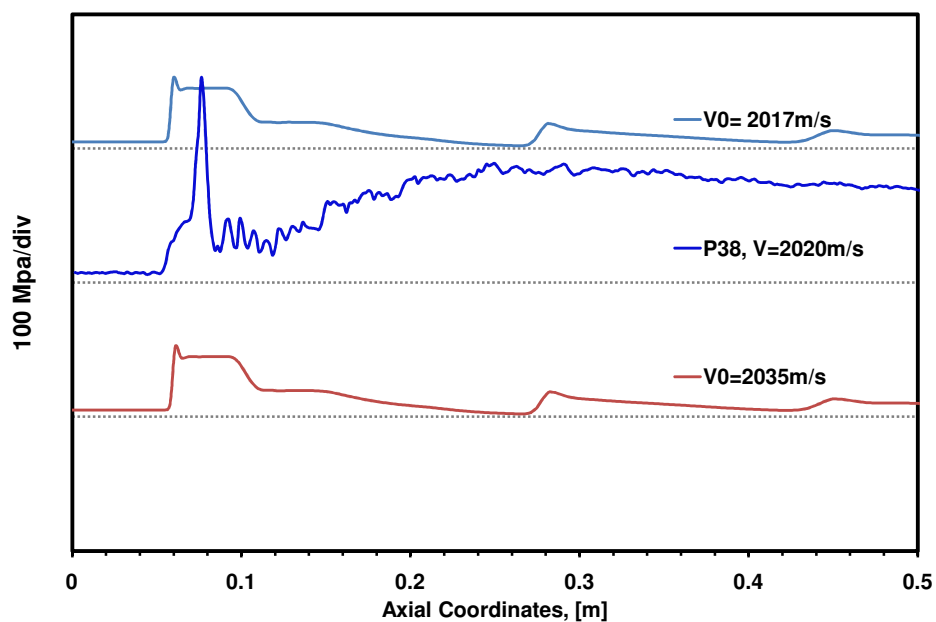


Figure 5.10: Pressure profiles on the tube wall, Experimental velocity; P16=1740m/s, P

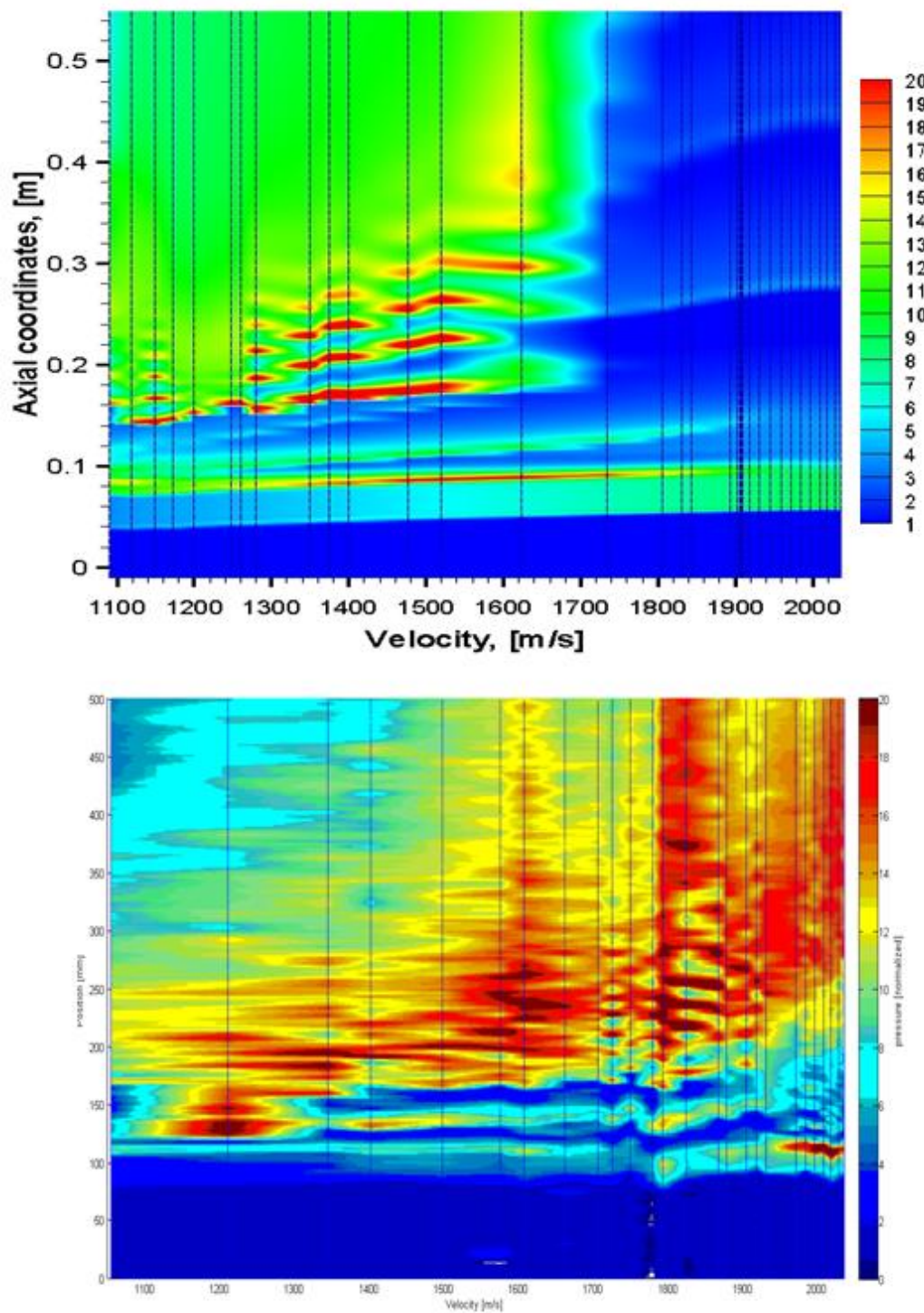


Figure 5.11: Pressure field map of the ram accelerator, CFD calculations (*Top*), Experimental data (*bottom*), velocity=1091 - 2035m/s

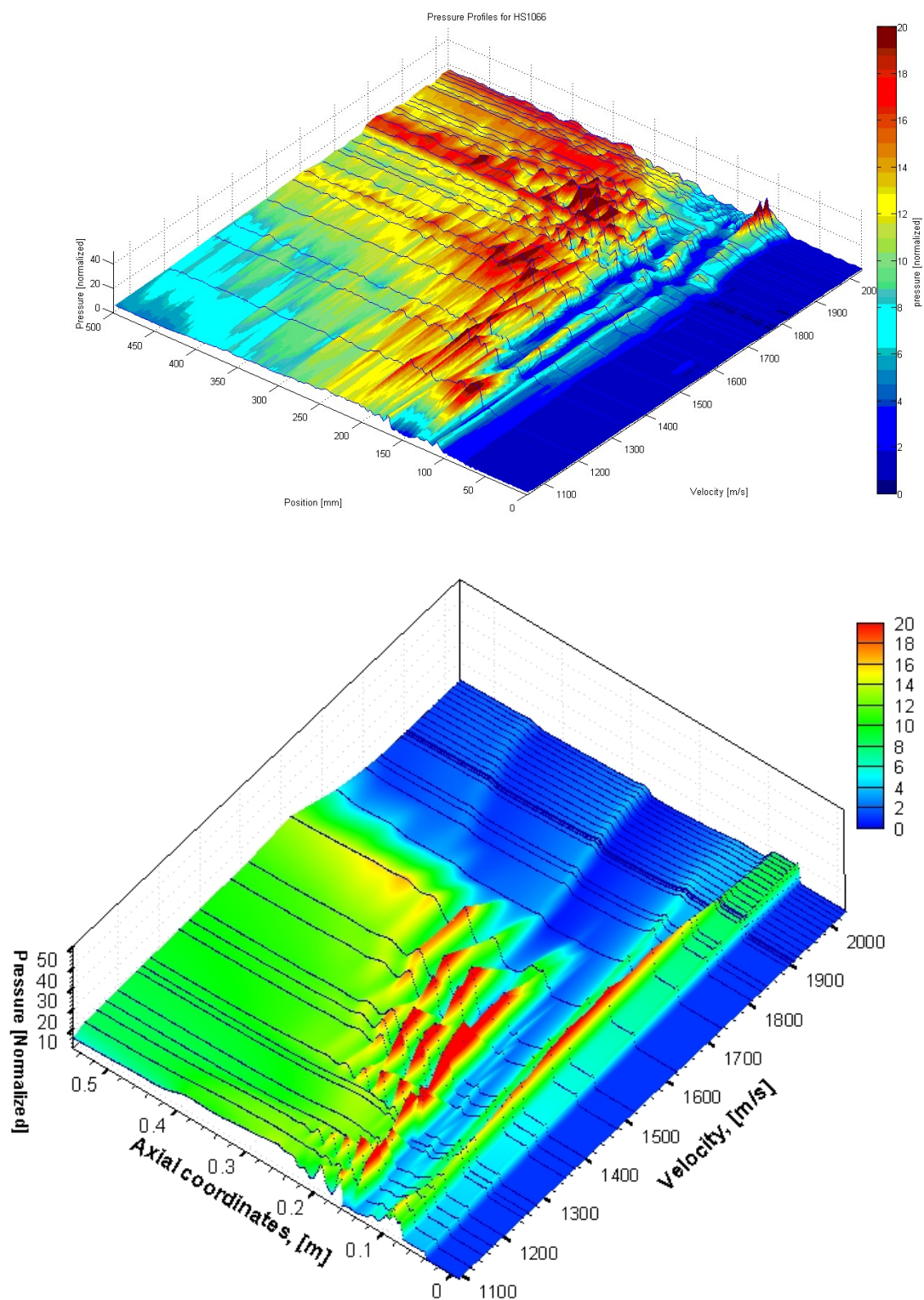


Figure 5.12: Pressure field map of the ram accelerator, Experimental data (*Top*), CFD calculations (*bottom*), velocity=1091 - 2035m/s

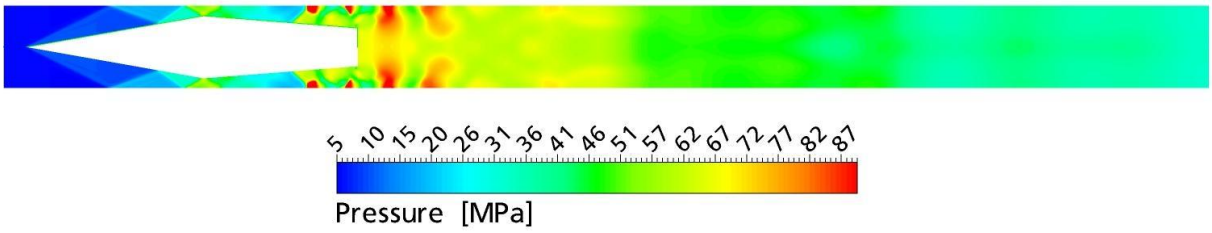


Figure 5.13: Pressure contours, in-coming velocity= $1091\text{m/s}$

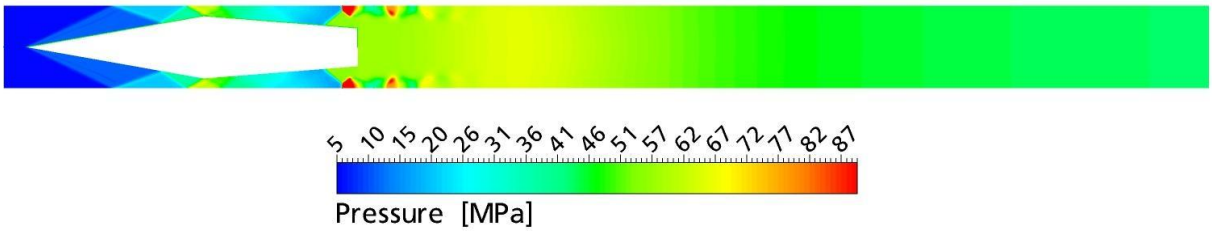


Figure 5.14: Pressure contours, in-coming velocity= $1173\text{m/s}$

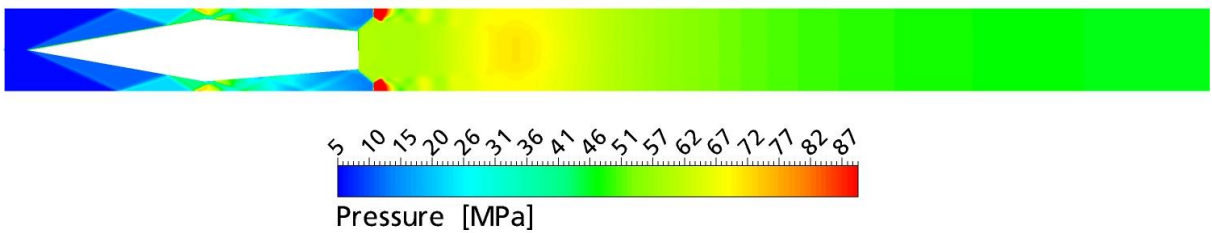


Figure 5.15: Pressure contours, in-coming velocity= $1247\text{m/s}$

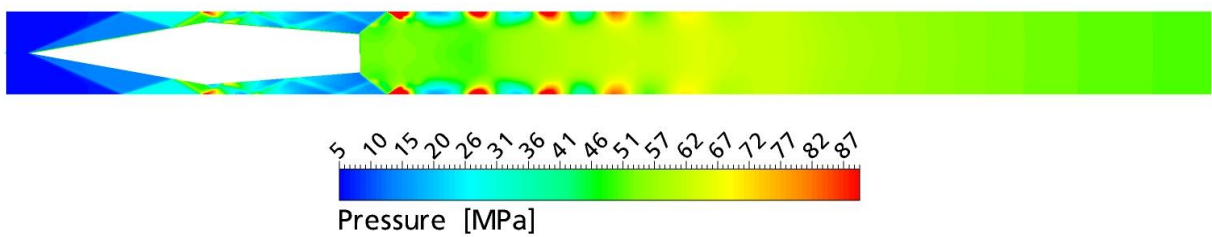


Figure 5.16: Pressure contours, in-coming velocity= $1374\text{m/s}$

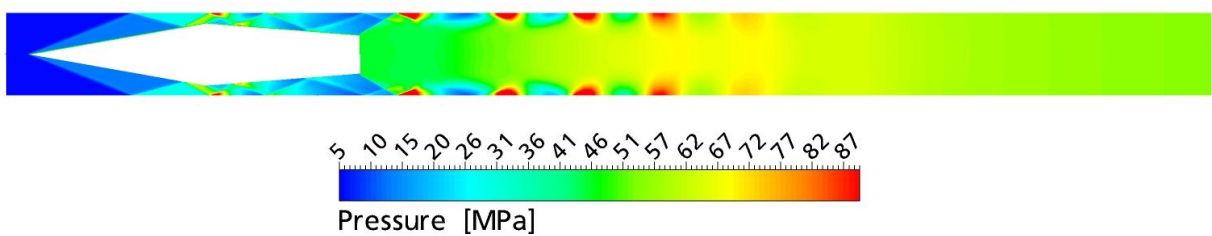


Figure 5.17: Pressure contours, in-coming velocity= $1476\text{m/s}$

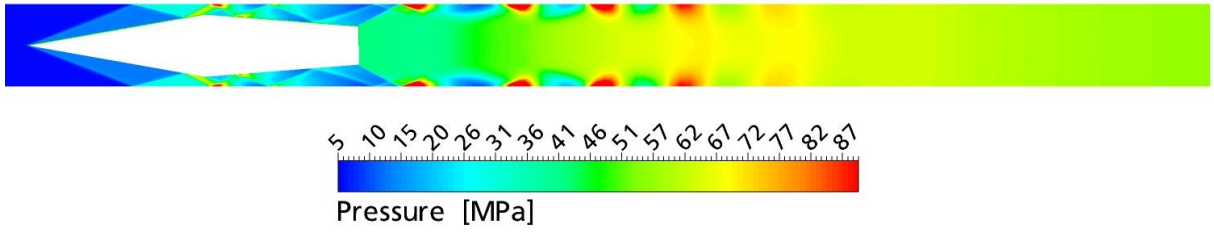


Figure 5.18: Pressure contours, in-coming velocity= $1519m/s$

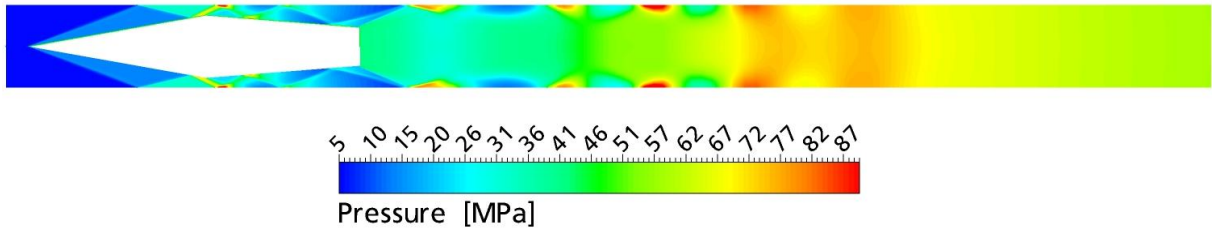


Figure 5.19: Pressure contours, in-coming velocity= $1622m/s$

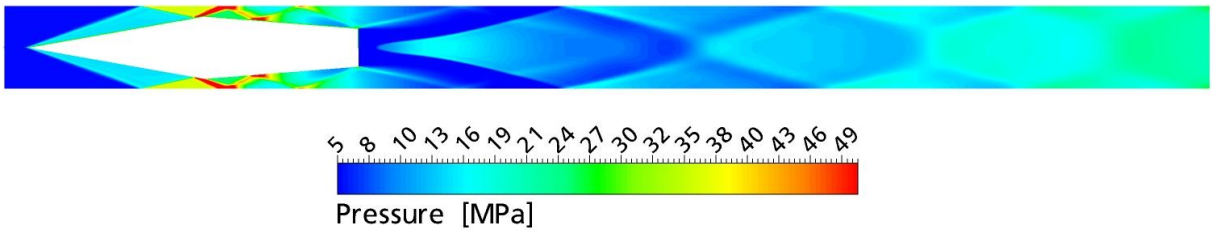


Figure 5.20: Pressure contours, in-coming velocity= $1733m/s$

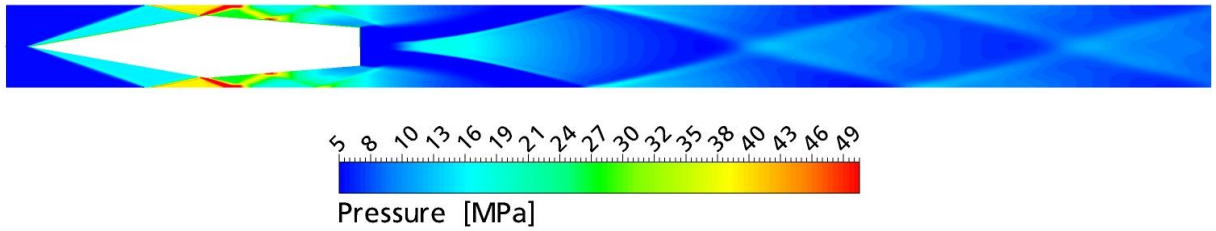


Figure 5.21: Pressure contours, in-coming velocity= $1829m/s$

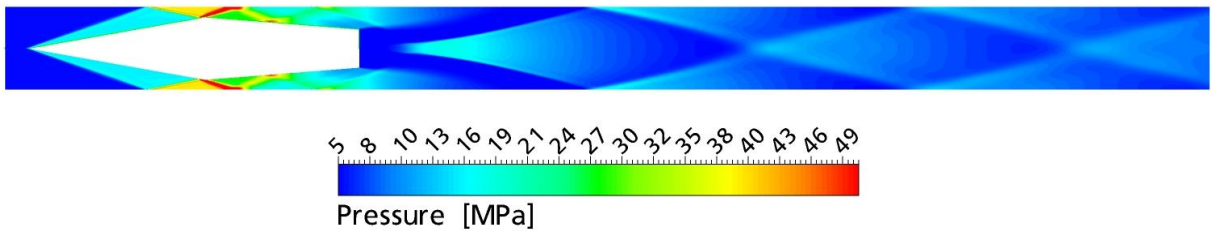


Figure 5.22: Pressure contours, in-coming velocity= $1842m/s$

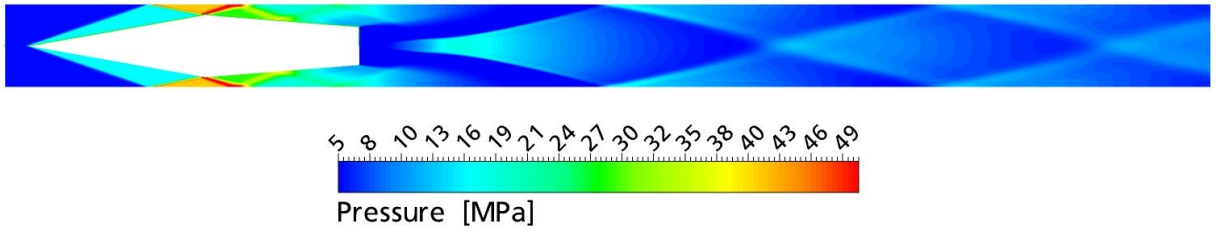


Figure 5.23: Pressure contours, in-coming velocity= $1891m/s$

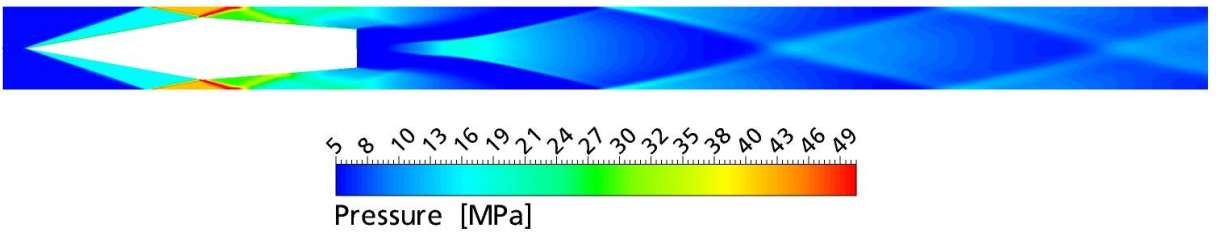


Figure 5.24: Pressure contours, in-coming velocity= $1900m/s$

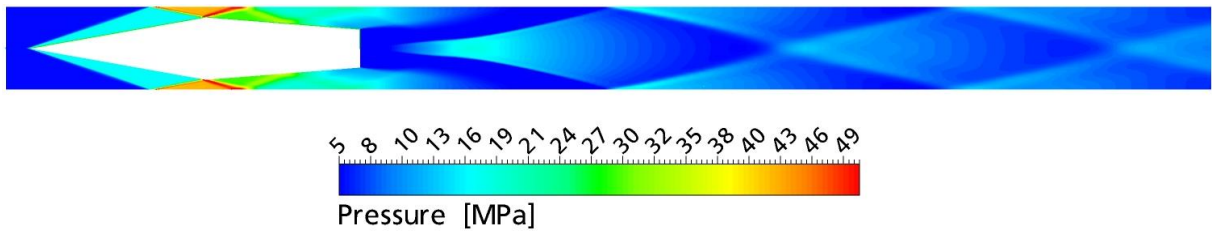


Figure 5.25: Pressure contours, in-coming velocity= $1917m/s$

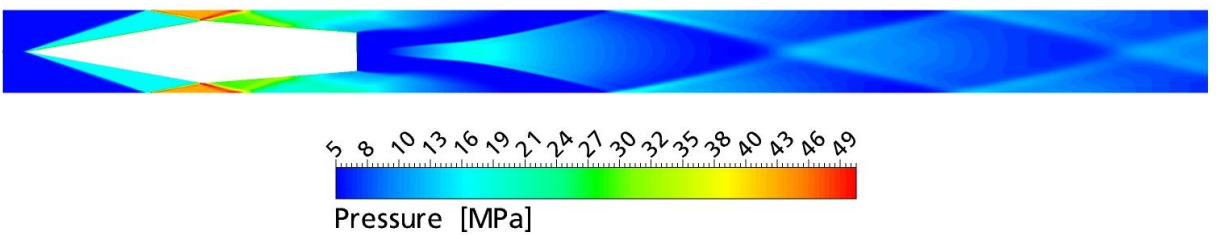


Figure 5.26: Pressure contours, in-coming velocity= $1930m/s$

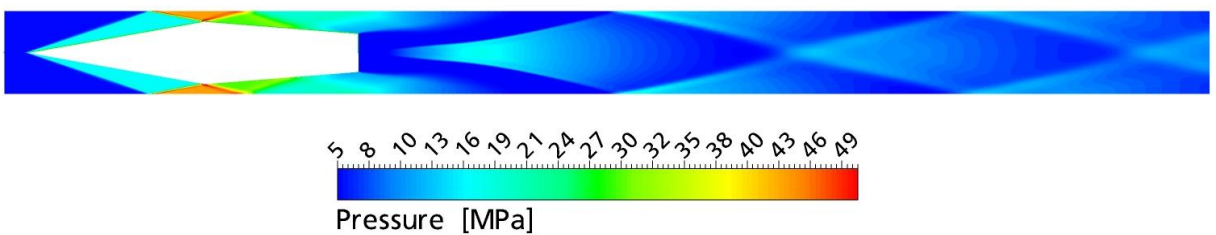


Figure 5.27: Pressure contours, in-coming velocity= $1943m/s$



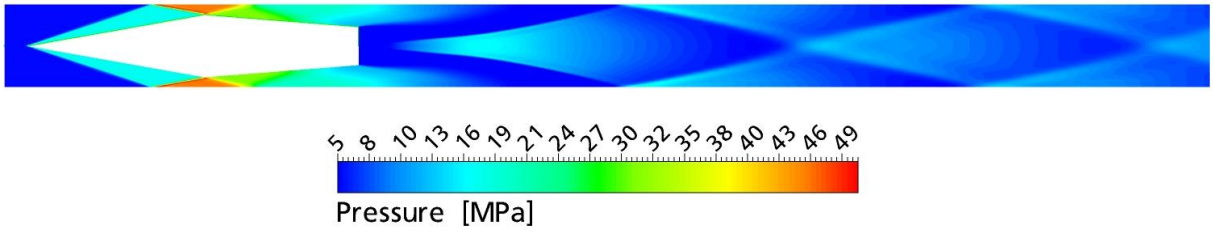


Figure 5.28: Pressure contours, in-coming velocity= $1519\text{m/s}$

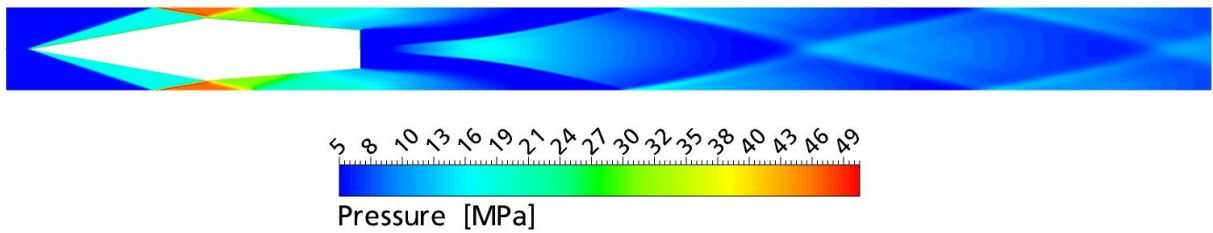


Figure 5.29: Pressure contours, in-coming velocity= $2007\text{m/s}$

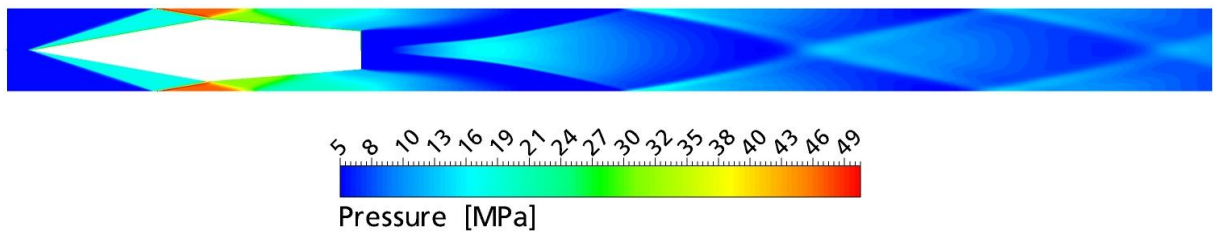


Figure 5.30: Pressure contours, in-coming velocity= $2017\text{m/s}$

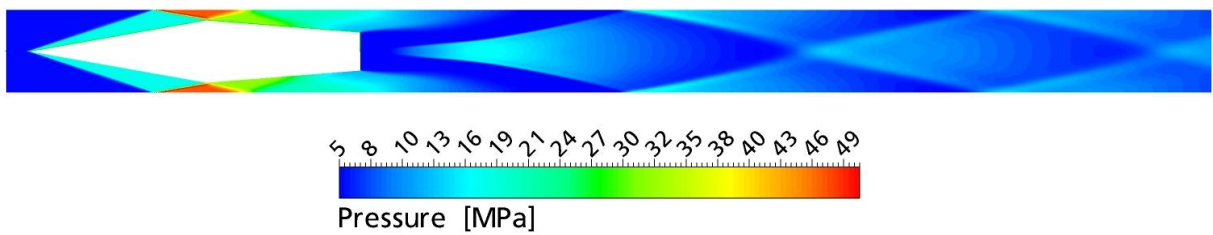


Figure 5.31: Pressure contours, in-coming velocity= $2027\text{m/s}$

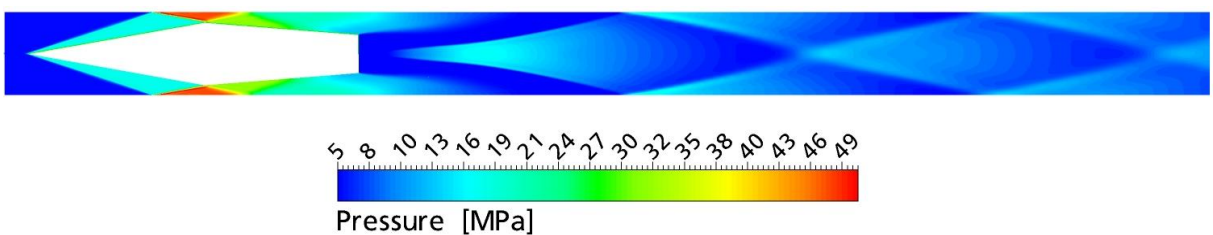


Figure 5.32: Pressure contours, in-coming velocity= $2035\text{m/s}$

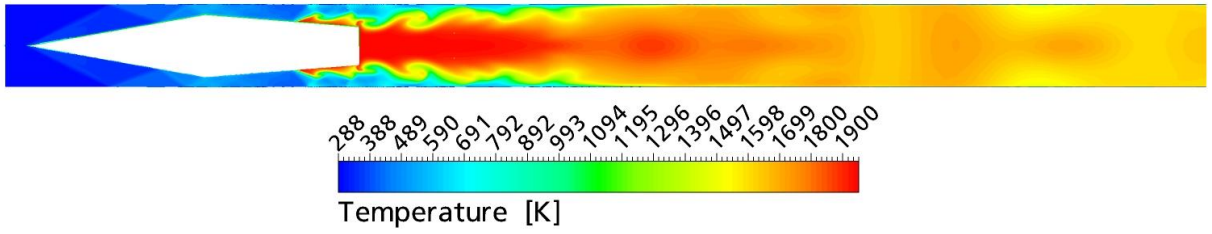


Figure 5.33: Temperature contours, in-coming velocity= $1091\text{m/s}$

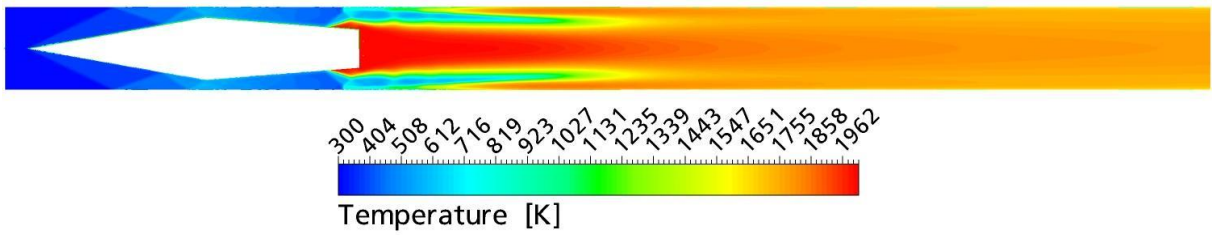


Figure 5.34: Temperature contours, in-coming velocity= $1173\text{m/s}$

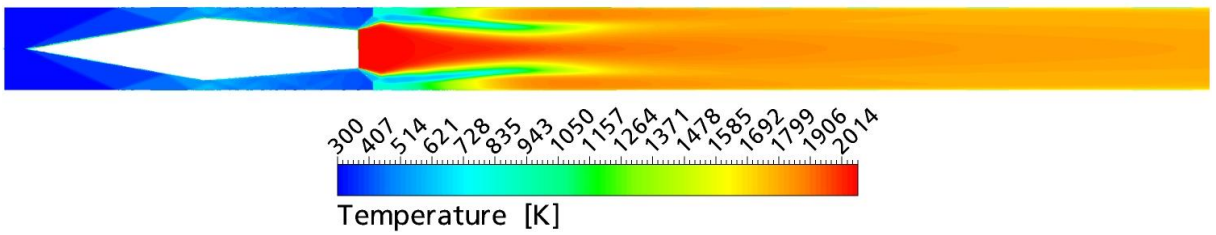


Figure 5.35: Temperature contours, in-coming velocity= $1247\text{m/s}$

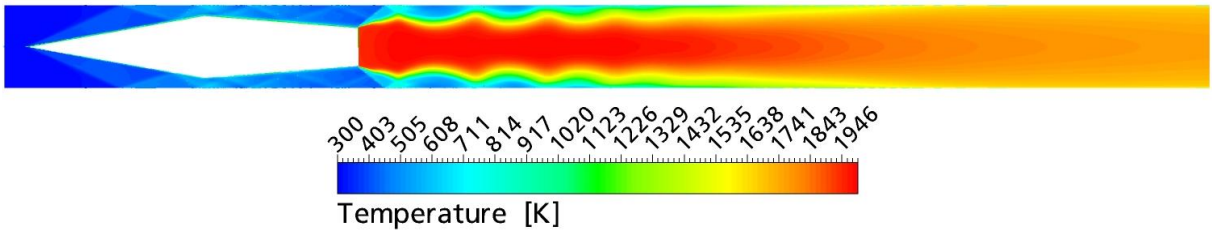


Figure 5.36: Temperature contours, in-coming velocity= $1374\text{m/s}$

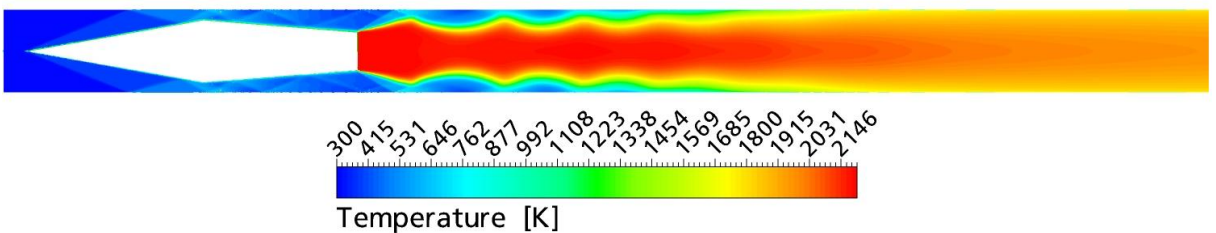


Figure 5.37: Temperature contours, in-coming velocity= $1476\text{m/s}$

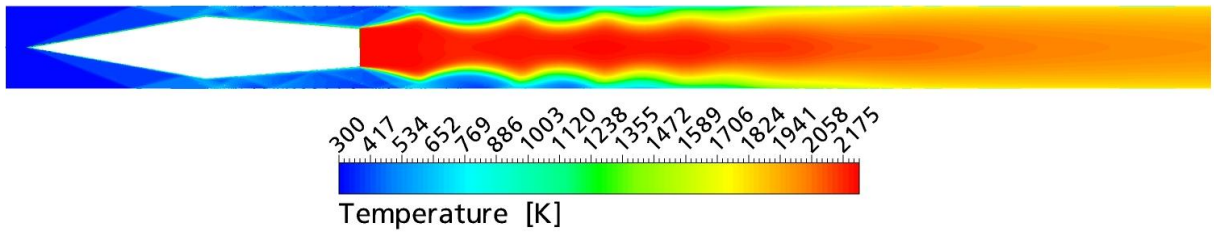


Figure 5.38: Temperature contours, in-coming velocity= $1519\text{m/s}$

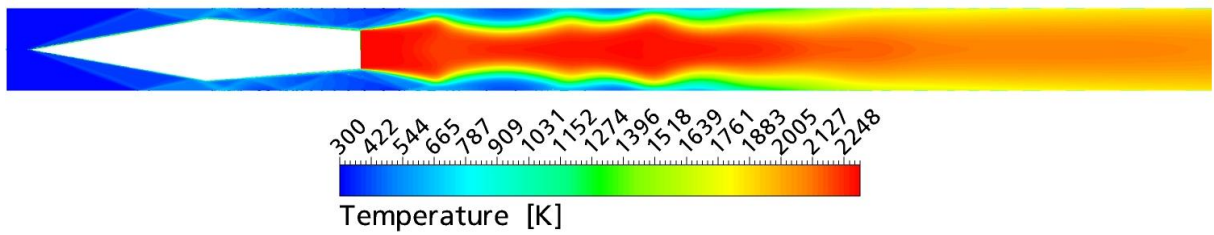


Figure 5.39: Temperature contours, in-coming velocity= $1622\text{m/s}$

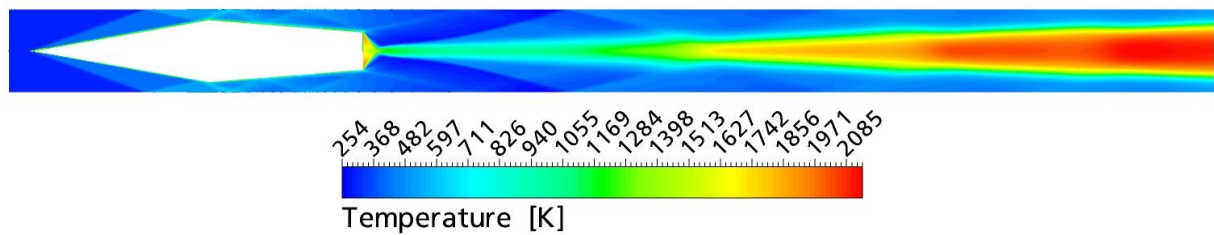


Figure 5.40: Temperature contours, in-coming velocity= $1733\text{m/s}$

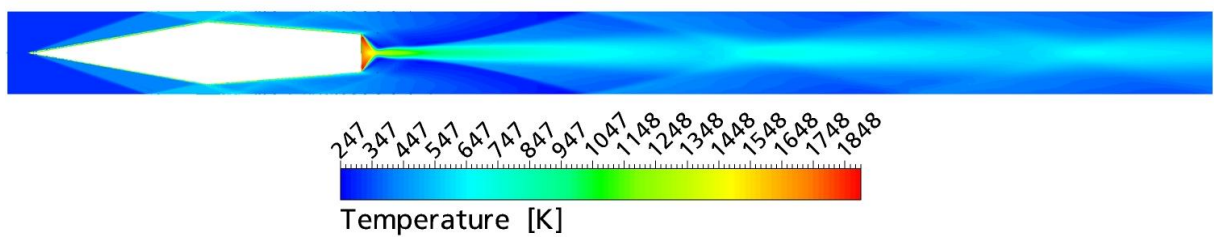


Figure 5.41: Temperature contours, in-coming velocity= $1829\text{m/s}$

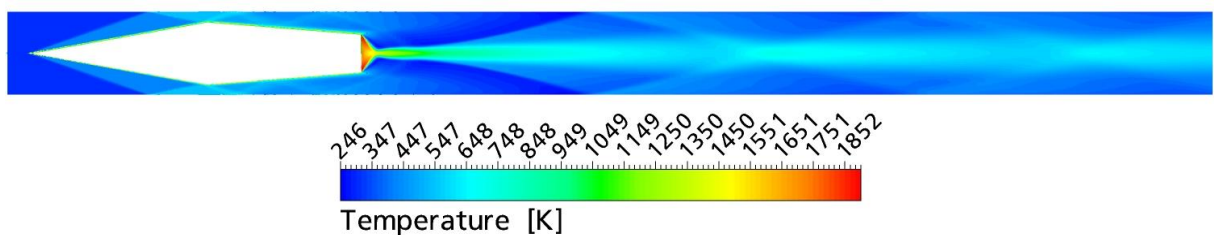


Figure 5.42: Temperature contours, in-coming velocity= $1842\text{m/s}$

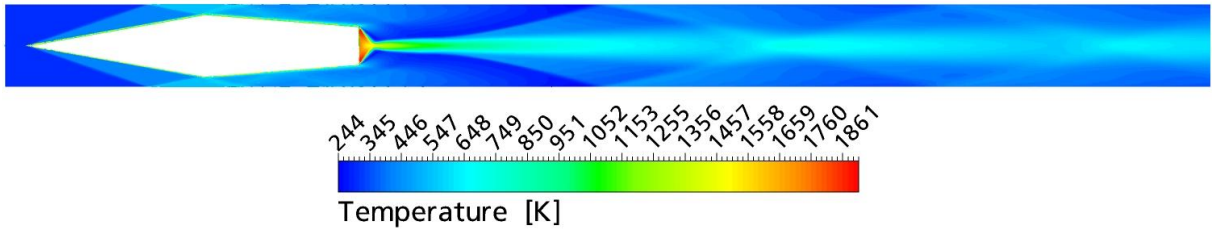


Figure 5.43: Temperature contours, in-coming velocity= $1891\text{m/s}$

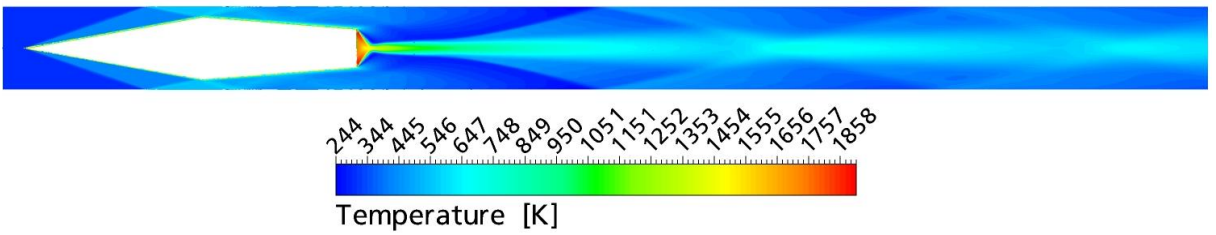


Figure 5.44: Temperature contours, in-coming velocity= $1900\text{m/s}$

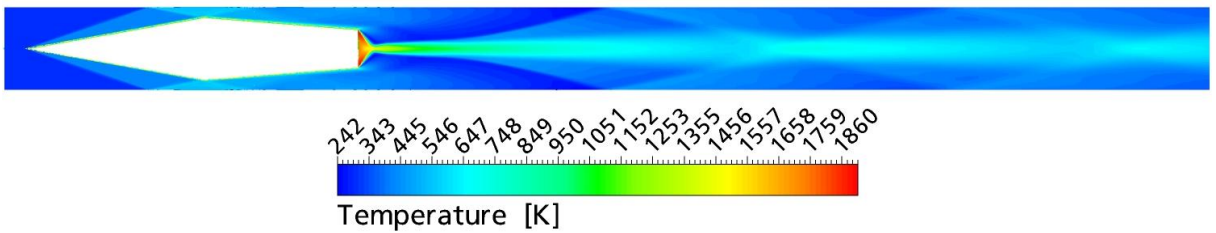


Figure 5.45: Temperature contours, in-coming velocity= $1817\text{m/s}$

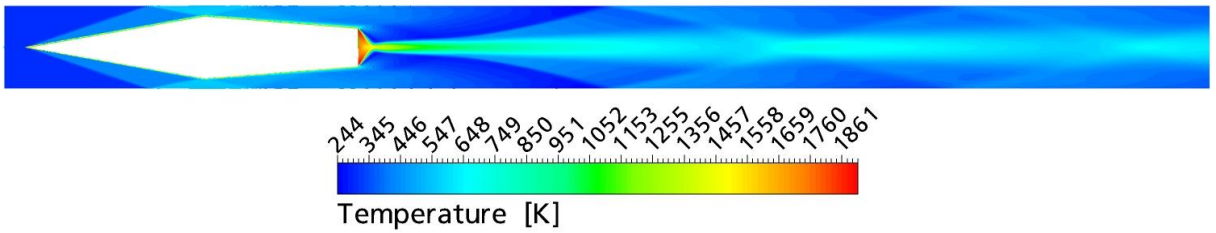


Figure 5.46: Temperature contours, in-coming velocity= $1930\text{m/s}$

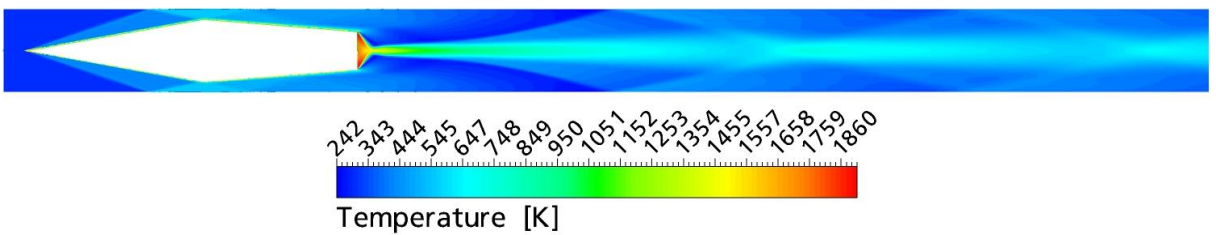
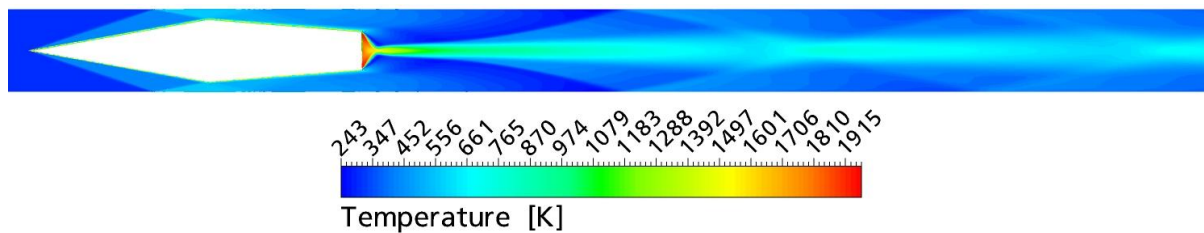
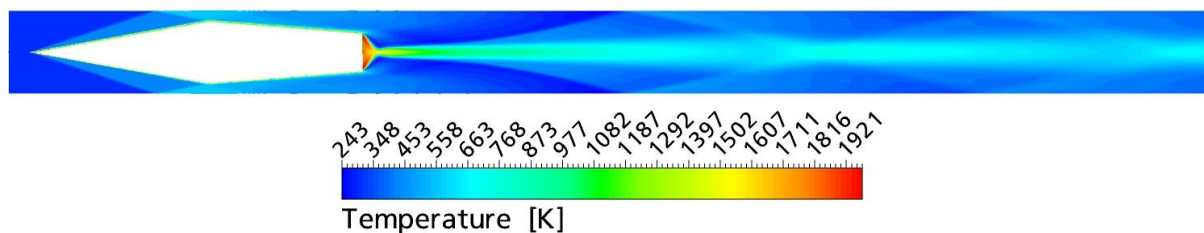
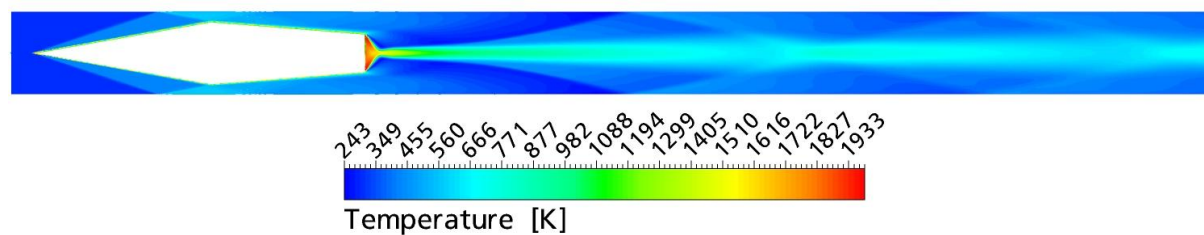
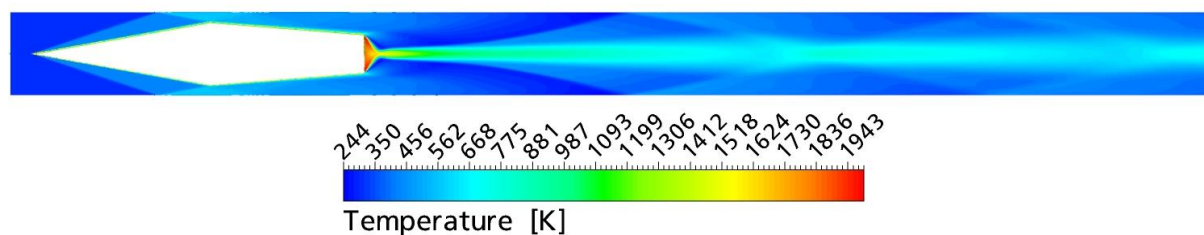
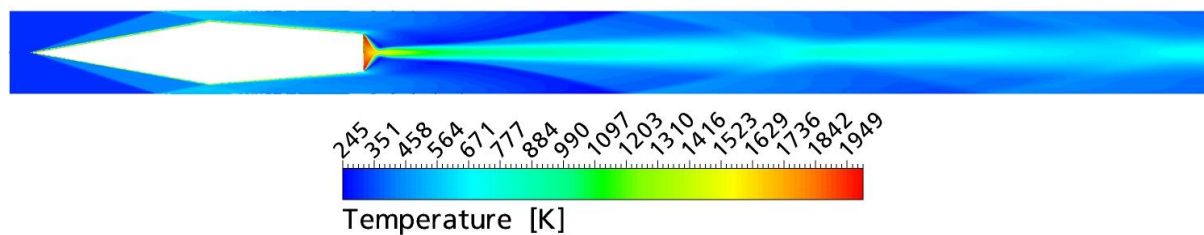


Figure 5.47: Temperature contours, in-coming velocity= $1943\text{m/s}$

Figure 5.48: Temperature contours, in-coming velocity= $1519m/s$ Figure 5.49: Temperature contours, in-coming velocity= $2007m/s$ Figure 5.50: Temperature contours, in-coming velocity= $2017m/s$ Figure 5.51: Temperature contours, in-coming velocity= $2027m/s$ Figure 5.52: Temperature contours, in-coming velocity= $2035m/s$

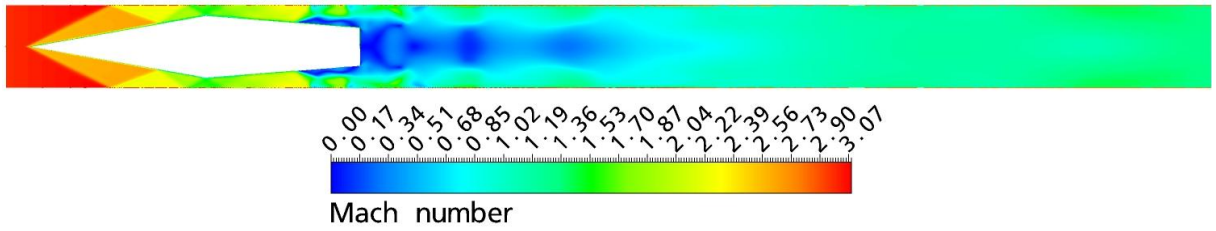


Figure 5.53: Mach number contours, in-coming velocity= $1091m/s$

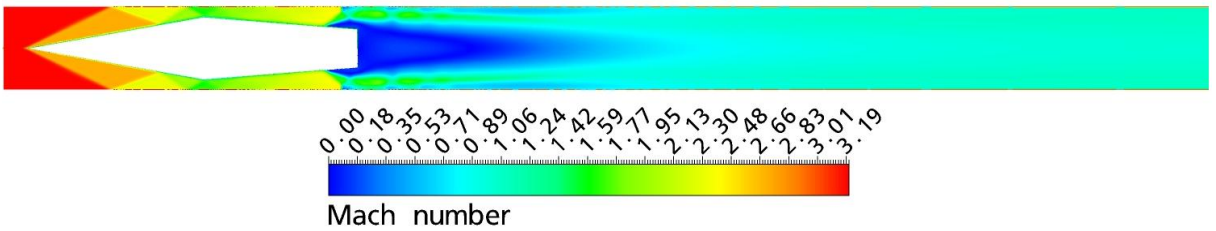


Figure 5.54: Mach number contours, in-coming velocity= $1173m/s$

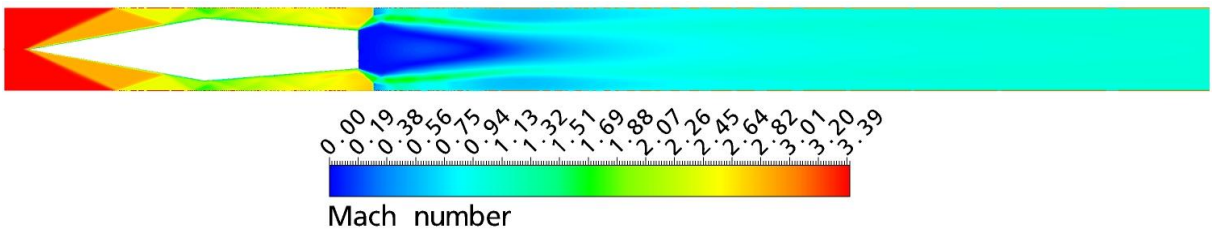


Figure 5.55: Mach number contours, in-coming velocity= $1247m/s$

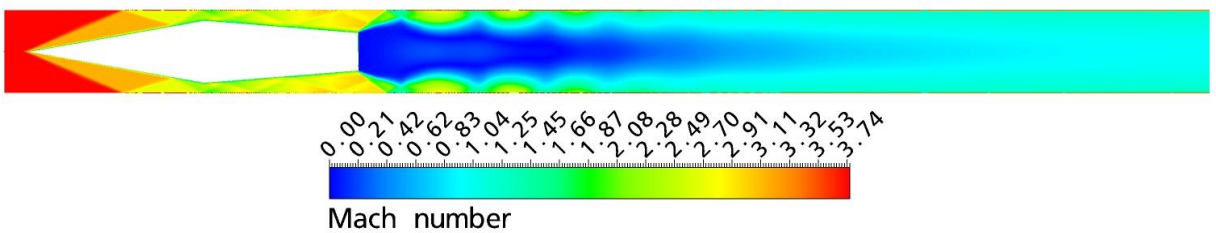


Figure 5.56: Mach number contours, in-coming velocity= $1374m/s$

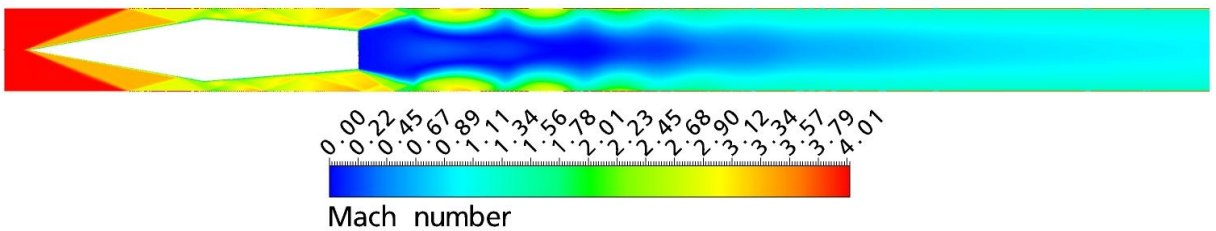


Figure 5.57: Mach number contours, in-coming velocity= $1476m/s$

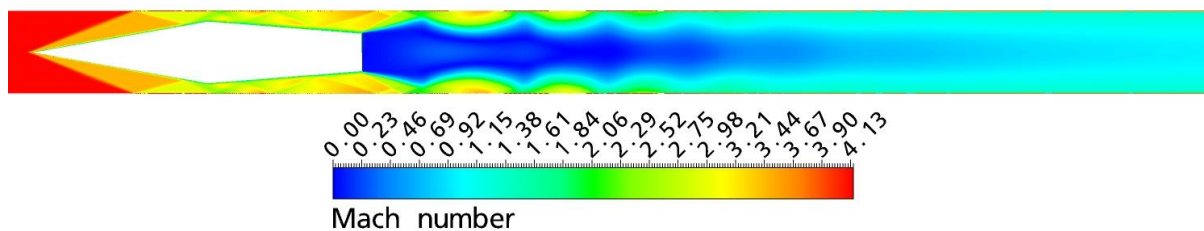


Figure 5.58: Mach number contours, in-coming velocity= $1519\text{m/s}$

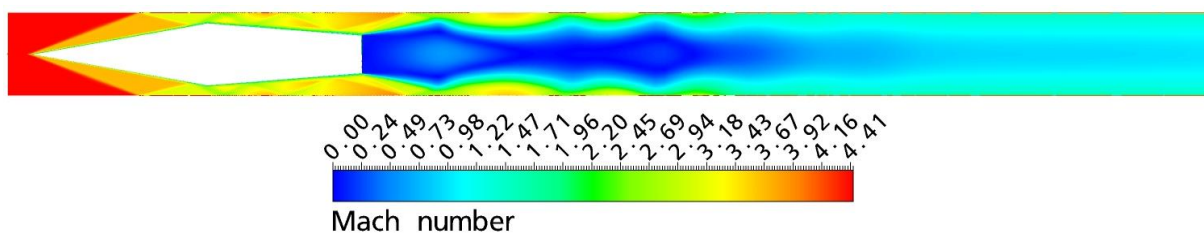


Figure 5.59: Mach number contours, in-coming velocity= $1622\text{m/s}$

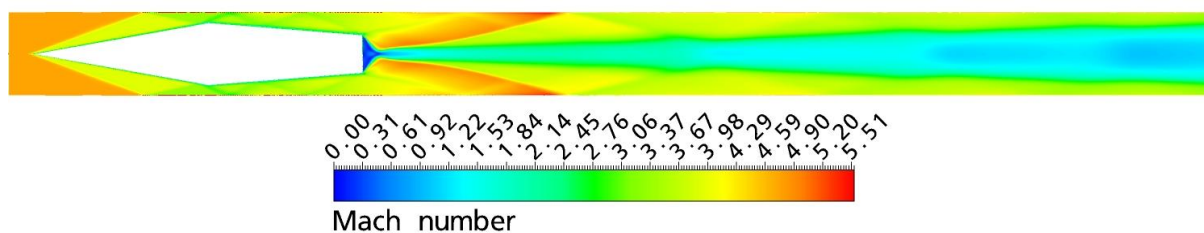


Figure 5.60: Mach number contours, in-coming velocity= $1733\text{m/s}$

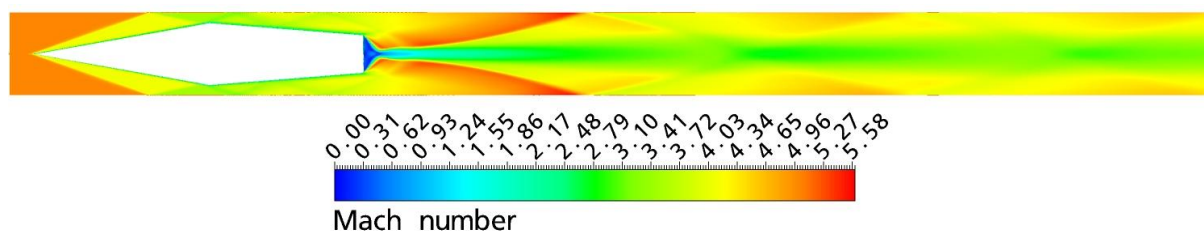


Figure 5.61: Mach number contours, in-coming velocity= $1829\text{m/s}$

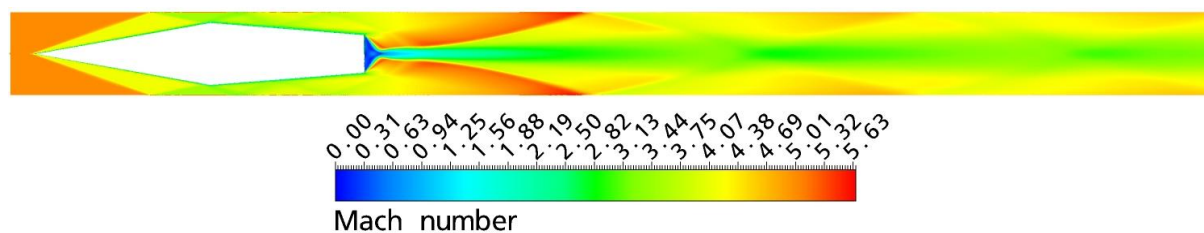


Figure 5.62: Mach number contours, in-coming velocity= $1842\text{m/s}$

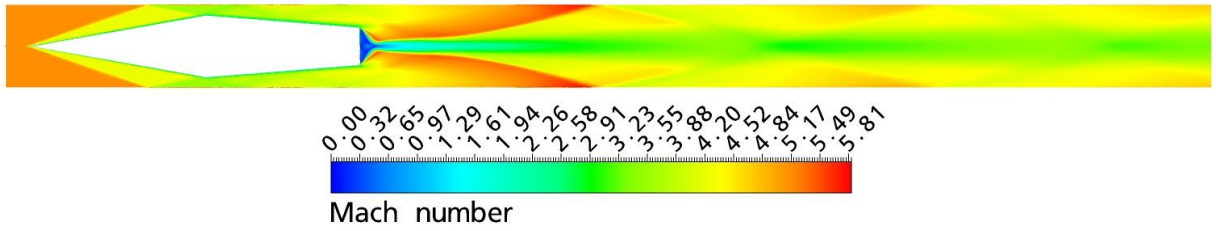


Figure 5.63: Mach number contours, in-coming velocity= $1891m/s$

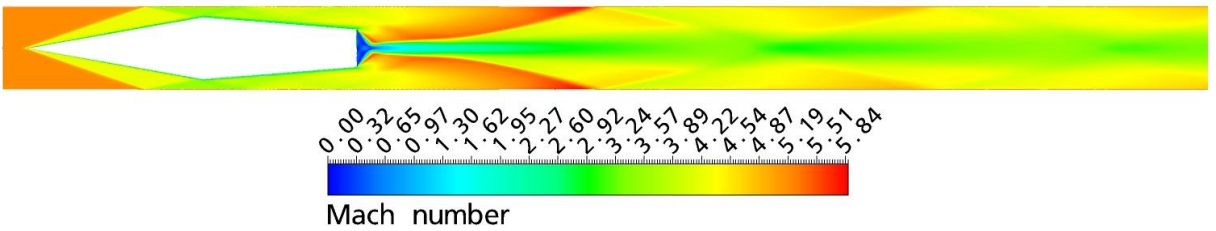


Figure 5.64: Mach number contours, in-coming velocity= $1900m/s$

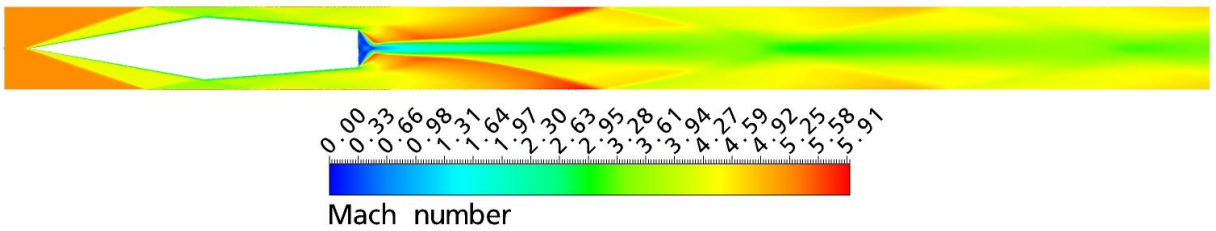


Figure 5.65: Mach number contours, in-coming velocity= $1817m/s$

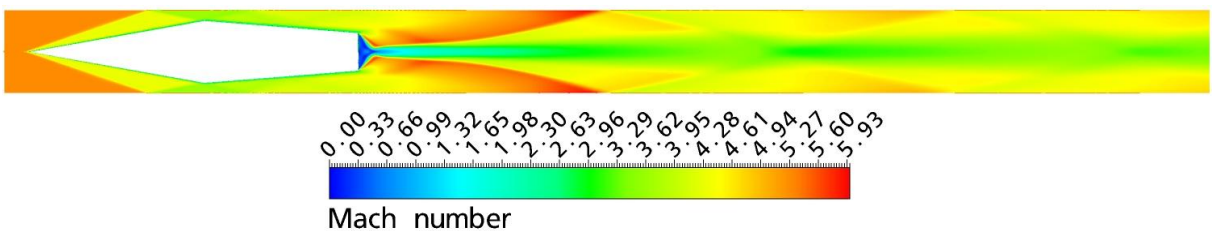


Figure 5.66: Mach number contours, in-coming velocity= $1930m/s$

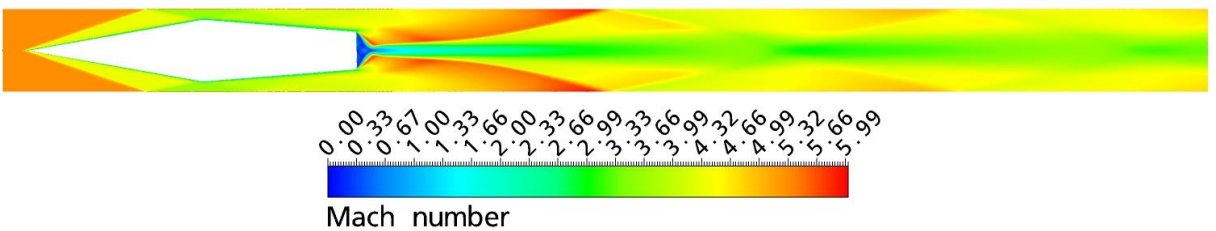


Figure 5.67: Mach number contours, in-coming velocity= $1943m/s$



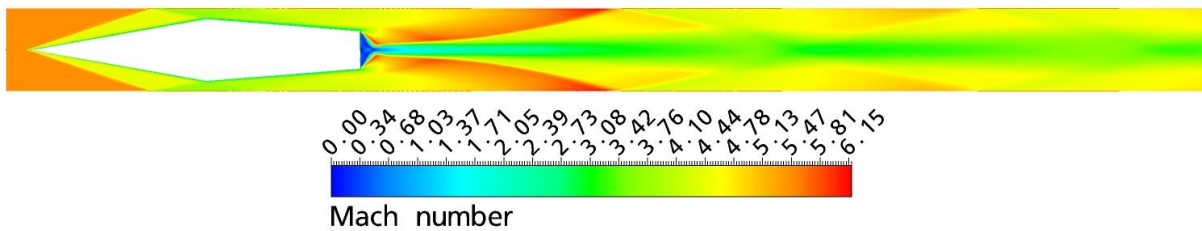


Figure 5.68: Mach number contours, in-coming velocity= $1519m/s$

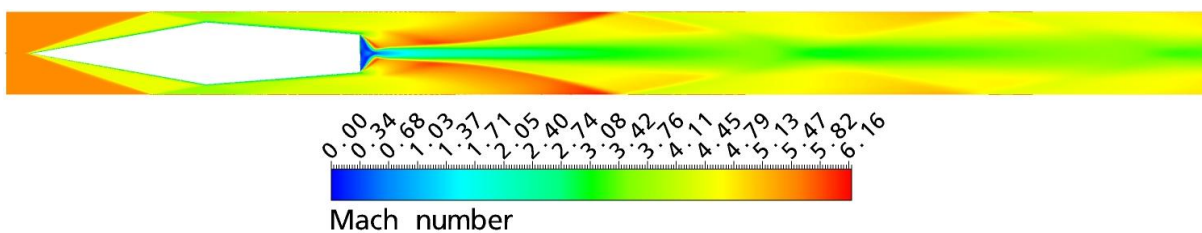


Figure 5.69: Mach number contours, in-coming velocity= $2007m/s$

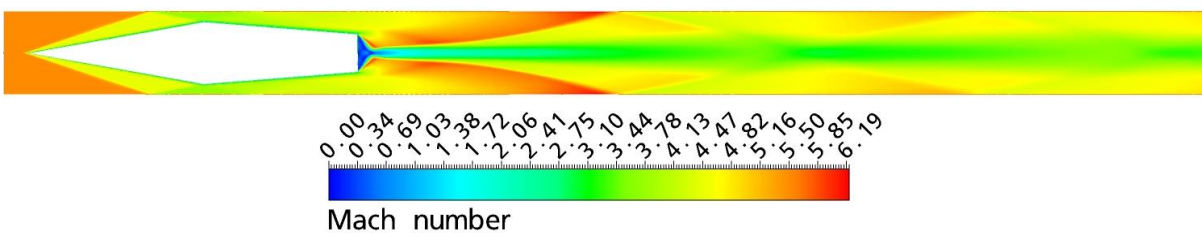


Figure 5.70: Mach number contours, in-coming velocity= $2017m/s$

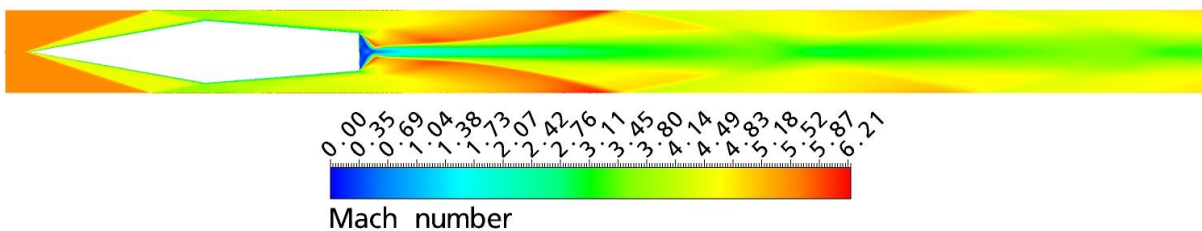


Figure 5.71: Mach number contours, in-coming velocity= $2027m/s$

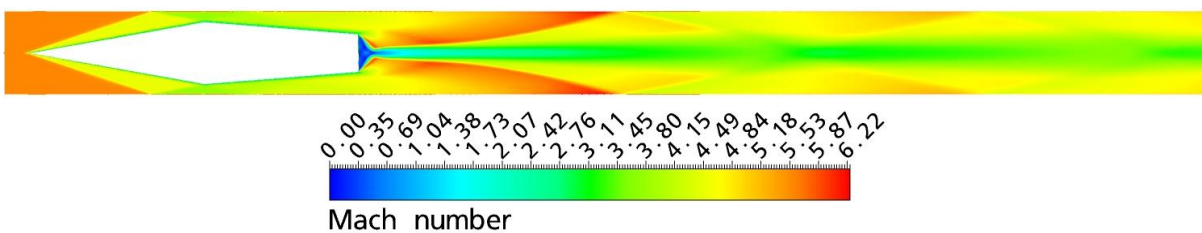


Figure 5.72: Mach number contours, in-coming velocity= $2035m/s$

## 5.4 Thrust

The axial thrust from computations using five-step reaction model is determined by integrating the pressure distribution over the surface of the projectile. figure (5.73) shows that the predicted CFD thrusts at all incoming Mach numbers up to  $M_0 = 4.4$  ( $V_0 = 1622 \text{ m/s}$ ) are 8 to 21% greater than the experimental data, the predicted thrusts between  $M_0 = 4.4$  and  $M_0 = 5.1$  are in good agreement with experimental data. The discrepancy in thrust is due, in part, to lack of fin drag being considered in the calculations. Another factor not considered in the CFD

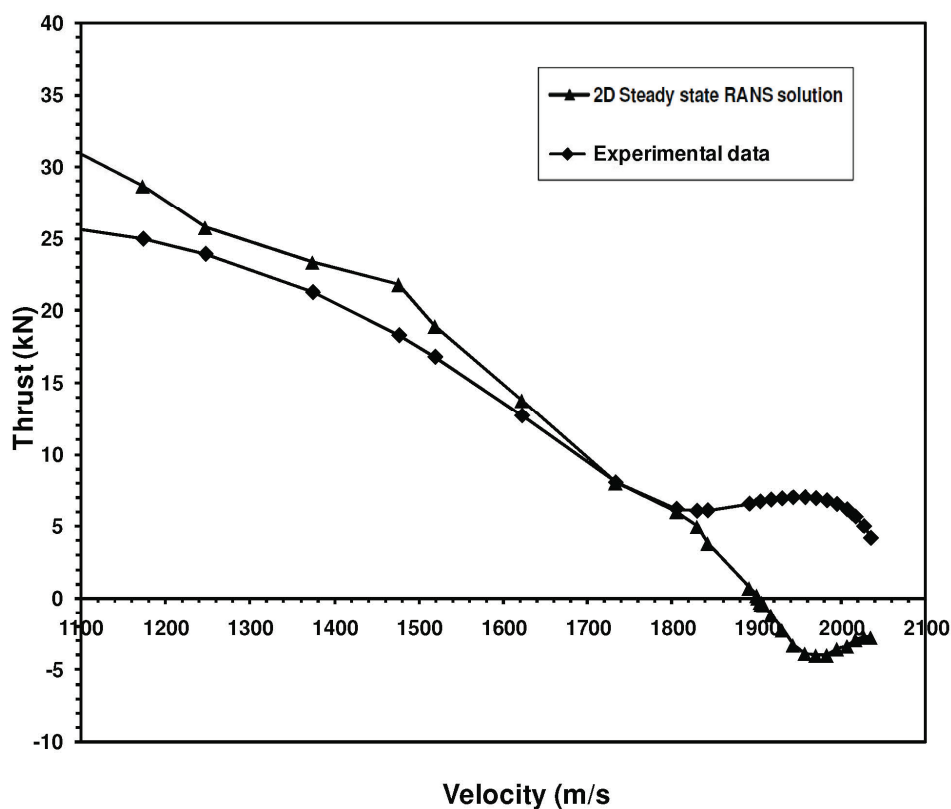


Figure 5.73: Comparison of the CFD predicted thrust with experimental data.

modeling is the unsteadiness of the flow field, i.e., the projectile acceleration under these conditions was  $\sim 25,000$  gees. The experimental thrust seen in figure (5.73) deviates significantly from the theoretical calculation. This is due to the projectile making a transition from the thermally choked propulsive mode to the transdetonative mode [6]. This transition occurs when the projectile reaches approximately 90% of the Chapman-Jouguet speed. The current calculation attempts to predict the ram accelerator performance in the thermally choked regime, as the condition is  $M_2 = 1$  at station 2.

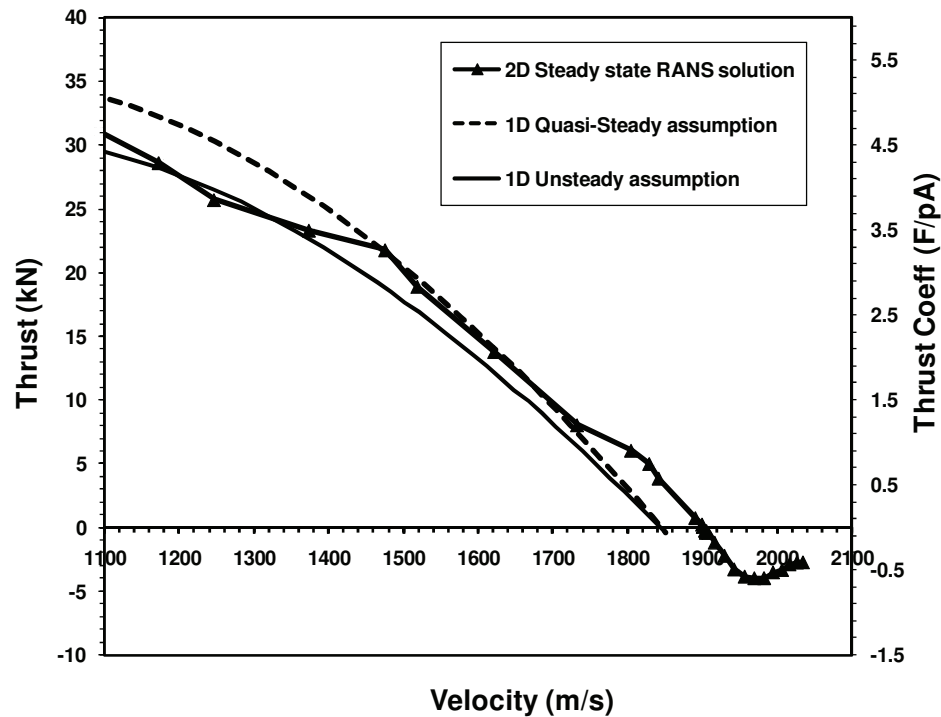


Figure 5.74: Thrust vs velocity

One-dimensional studies have shown that accounting for projectile acceleration reduces predicted thrust in amounts consistent with experiments [60]. figure (5.74) compares the predicted CFD thrust with that from one dimensional modeling, both, quasi-steady and unsteady assumptions are considered for this comparison. It is shown that taking into account the unsteady effects reduces the predicted thrust as shown by Bauer et al [60]. The results show that the predicted CFD thrusts are in good agreement with unsteady one dimensional model at a lower Mach number between  $M_0 = 2.92$ , and  $M_0 = 3.9$ ; however between  $M_0 = 4.4$  and  $M_0 = 4.8$ . The predicted CFD thrusts are in perfect match with that predicted by quasi-steady one dimensional modeling. Increases in CFD thrusts were observed after  $M_0 = 4.9$  by 10 to 14%. The thrust equals zero represents the thrust for which the speed is the Chapman-Jouguet (CJ) detonation speed. The detonation speed predicted by one dimensional modeling for the present propellant is 1845 *m/s* and the predicted detonation speed (CJ) from the CFD calculation is 1901 *m/s*; i.e, a discrepancy of 3%.

## 5.5 Summary

Computational fluid dynamics solutions of the Reynolds Averaged Navier-Stokes (RANS) equations have been used to numerically predict the ram accelerator performance in the thermally choked propulsive mode. Simulations were carried out for a series of incoming velocities. The shear-stress transport turbulence model (SST) and the eddy dissipation combustion model (EDM), with detailed reaction mechanism have been used to simulate the fully turbulent reactive flow field in the ram

accelerator. Simulations take into account the effect of the radiation/turbulence interactions. The spherical harmonic P1 method was used, the gray medium assumption is employed and the Planck-mean absorption coefficients are used to determine the radiative properties of the gas-phase species. Results from the simulation were compared against the experimental data derived from the University of Washington facility. Investigations about the effect of the chemical kinetics mechanism in the modeling, as well as the effect of the thermal radiation have been carried out. Results show that using a five steps kinetics mechanism with thermal radiation in the modeling, was unable to predict the ram accelerator performance at velocities greater than CJ speed. The pressure profile agreed very well with the experimental data in the thermally choked propulsive mode, between Mach number ( $M_0 = 2.98$ ) and ( $M_0 = 4.4$ ). When approaching the trans-detonative propulsion mode the pressure amplitude at the projectile base was under-predicted by the modeling, this may be due to the turbulence settings, which has to be determined differently. The modeling of the turbulent flow in the transdetonative and the super-detonative is our ongoing research. The predicted thrust in the thermally choked propulsive mode agreed well with the experimental data and the velocity for which the thrust is zero was obtained from the CFD modeling.

# Chapter 6

## Refinement on the one dimensional ram accelerator model

### 6.1 Introduction

In chapter 1 we discussed the unsteadiness assumption in the one dimensional modeling of the ram accelerator in the sub-detonative combustion mode, including the real gas effects in the modeling. The control volume model to account for unsteady flow effects indicates that the thrust coefficient vs Mach-number profile obtained is lower than that obtained with the quasi-steady model. This deviation correlates with experimental results obtained in a 38-mm-bore ram accelerator at 5.15 MPa fill pressure, figure (6.1) reference [Figure 1.6]. The theoretical calculations were carried out with the assumption that  $L_{CV}$  was set at twice the projectile length ( $L_{CV} = 2L_P$ ). The evidence of this ratio is based on luminosity and pressure records showing that the termination of the combustion zone occurs approximately one projectile length behind its base [5]. The choice of the length of the control volume remains a key issue in the unsteady modeling of the ram accelerator. In this chapter, more refinement on

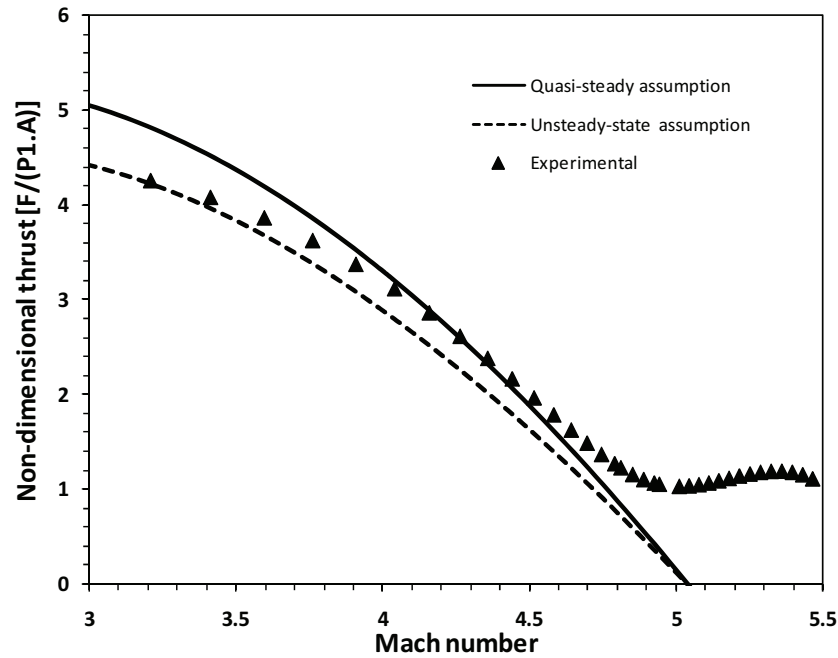


Figure 6.1: Non-dimensional Thrust-Mach plot for  $2.95CH_4 + 2O_2 + 5.7N_2$  propellant with quasi-steady and unsteady modeling;  $L_{CV} = 2L_p$ ,  $P_0 = 5.15MPa$ , (Ideal gas EoS was used at station 1, and Boltzmann EoS was used for the calculation of properties of combustion products)

the unsteady one dimensional model will be carried out to investigate the influence of the length of the control volume on the thrust coefficient and on the projectile acceleration by assuming different values for  $L_{CV}$ . We will also use the findings about the control volume derived from the RANS modeling [Chapter 5], the calculations will be validated against the experimental data.

## 6.2 Influence of the control volume length in the unsteady assumption

The parameter  $L_{CV}$  is a key element in the unsteady modeling because it appears in all of the conservation equations presented in chapter 1 (equations 1.2.4 to 1.2.6). The influence of this parameter on the theoretical non-dimensional thrust versus Mach number behavior is shown in figure (6.2), the results were compared against the experimental data derived from those conducted at University of Washington 38-mm-bore ram accelerator facility. The gas mixture composition:  $2.95CH_4 + 2O_2 + 5.7N_2$ , under 5.15 MPa fill pressure.

The influence on the non-dimensional thrust of a linear variation of  $L_{CV}$  from both  $4L_P$  to  $1L_P$  and  $6L_P$  to  $1L_P$  over the Mach number range 3 to  $M_{CJ}$  was explored. The larger the value of  $L_{CV}$  at a lower Mach number, the greater the reduction in thrust is that from the quasi-steady prediction. As the Mach number approaches to  $M_{CJ}$ , the influence of the assumption for  $L_{CV}$  diminishes as expected [60].

The velocity profiles presented in figure (6.3), shows that all the calculations predicted the velocity up to 6 meters, then it deviates when the projectile approaches the detonation velocity. Note that we attempt to model the characteristics of the ram accelerator in the sub-detonative regime.

The predicted ram accelerator performance for the thrust and velocity are in good agreement with the experimental data when using  $L_{CV} = 2L_P$ .



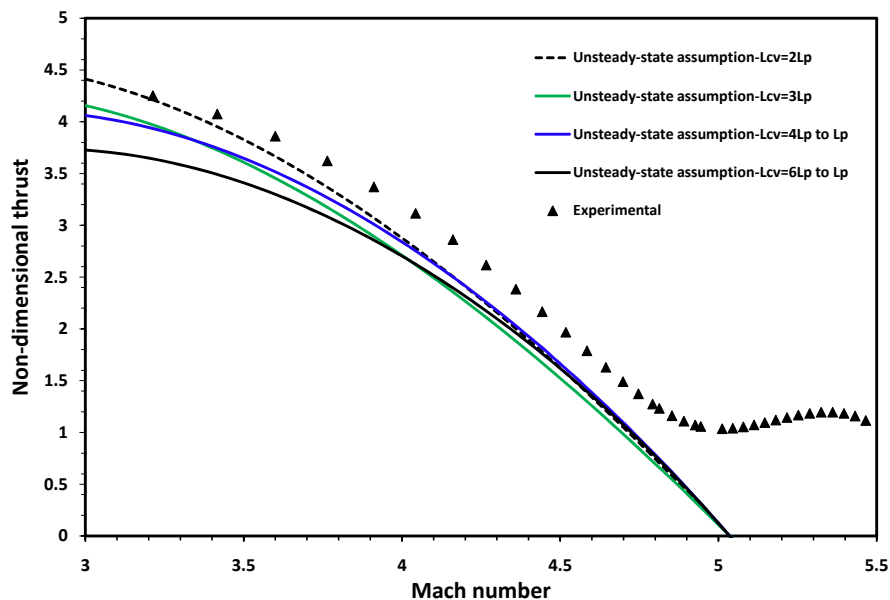


Figure 6.2: Non-dimensional Thrust-Mach plot for  $2.95CH_4 + 2O_2 + 5.7N_2$  propellant,  $P_0 = 5.15MPa$ , various values for  $L_{CV}$  were used (Ideal gas EoS was used at station 1, and Boltzmann EoS was used for the calculation of properties of combustion products)

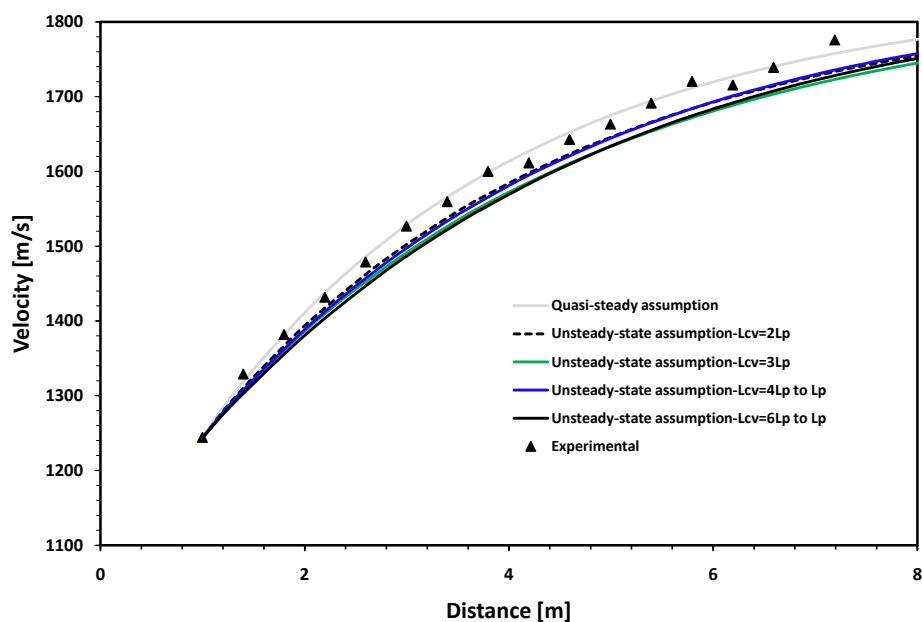


Figure 6.3: Velocity-distance plot for  $2.95CH_4 + 2O_2 + 5.7N_2$  propellant,  $P_0 = 5.15MPa$ , various values for  $L_{CV}$  were used (Ideal gas EoS was used at station 1, and Boltzmann EoS was used for the calculation of properties of combustion products)

The control volume length was investigated by CFD calculation for various in-coming velocities. The calculations consider velocities of the ram accelerator after the projectile had attained a velocity of 1240 m/s where the thermally choked propulsive mode was fully established and  $V_0=1829$  m/s. As expected the results show that control volume length at velocity of 1240 m/s is  $2.8 L_p$  and tends to decrease as mach number increases, to becomes  $1.1 L_p$  at velocity of 1829 m/s. Table (6.1) shows the results about the control volume length for all the incoming velocities considered in the modeling.

By including the CFD finding for the control volume length, it is readily observed in figure (6.4) that the calculated thrust using the CFD results for the control volume length gave a good match with the experimental data. Little deviation on the thrust curve occurs around  $M = 4.6$ , this is maybe due to the fact that the projectile approaches the Champman-Jouguet detonation speed. Note that our CFD modeling is based on ideal gas calculation. The compared velocity profile using different values for  $L_{CV}$  are shown in figure (6.5). Among all the predicted velocities, using CFD finding for the control volume predicts a good results. The difference when using various  $L_{cv}$  was small due to the fact that the acceleration effect is low ( the projectile having an acceleration of  $\sim 25kgee$ . more difference will predicted at high fill pressure as presented in chapter 1, section (1.4).

Table 6.1: The control volume function of the incoming velocity

$V(m/s)$	Control volume	$L_{CV}(m)$
1091	0.363	
1173	0.5032	
1247	0.428	
1374	0.5032	
1476	0.553	
1519	0.553	
1622	0.553	
1733	0.167	
1805	0.17	
1829	0.167	
1842	0.166	
1891	0.166	
1900	0.166	
1901	0.165	
1904	0.165	
1905	0.165	
1906	0.165	
1908	0.165	
1917	0.165	
1930	0.165	
1943	0.165	
1957	0.165	
1970	0.165	
1983	0.165	
1995	0.165	
2007	0.165	
2017	0.165	
2027	0.165	
2035	0.165	

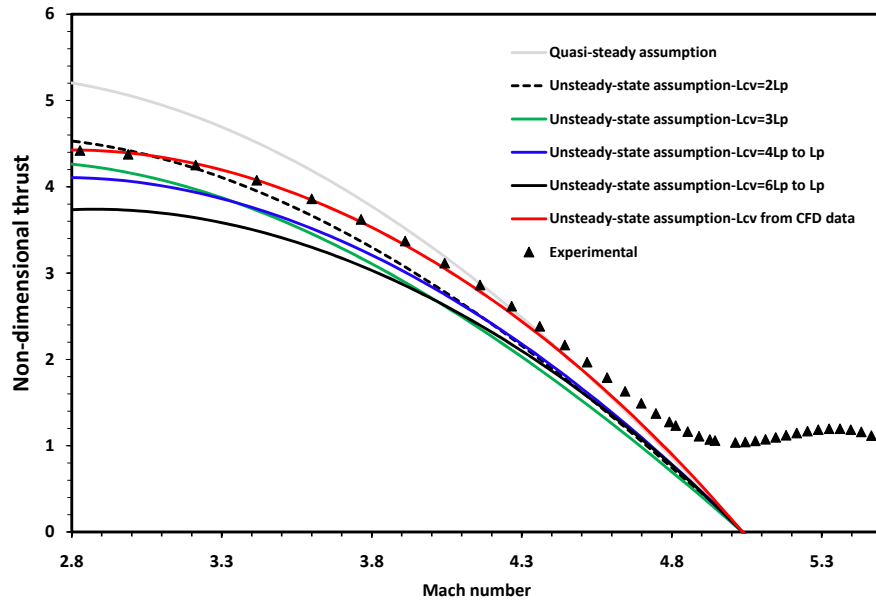


Figure 6.4: Non-dimensional Thrust-Mach plot for  $2.95CH_4 + 2O_2 + 5.7N_2$  propellant,  $P_0 = 5.15MPa$ , various values for  $L_{CV}$  were used (Ideal gas EoS was used at station 1, and Boltzmann EoS was used for the calculation of properties of combustion products)

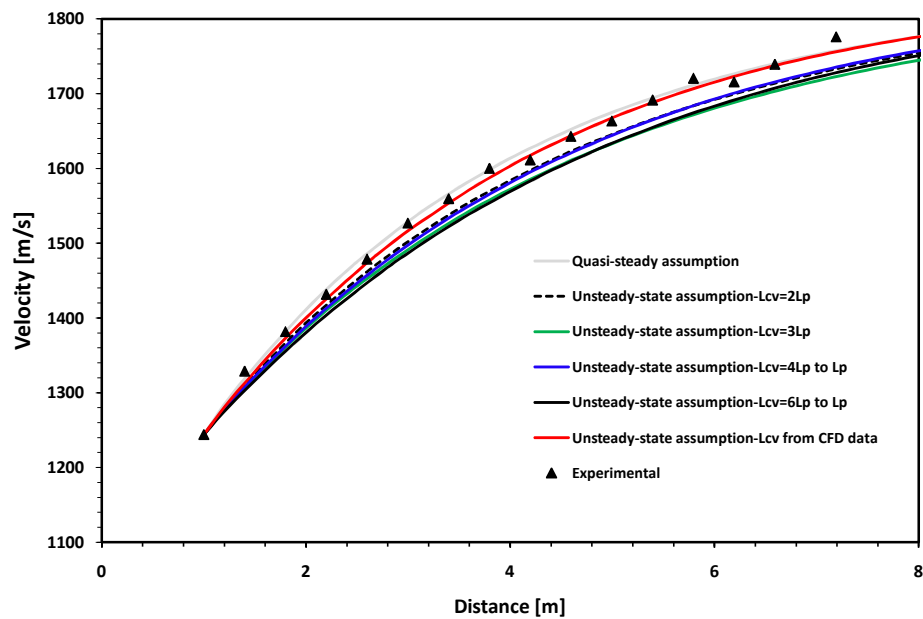


Figure 6.5: Velocity-distance plot for  $2.95CH_4 + 2O_2 + 5.7N_2$  propellant,  $P_0 = 5.15MPa$ , various values for  $L_{CV}$  were used (Ideal gas EoS was used at station 1, and Boltzmann EoS was used for the calculation of properties of combustion products)

Again, the one dimensional computer program "TARAM" for the unsteady calculation, successfully predicted the projectile velocity and thrust coefficient in the ram accelerator when the propulsion mode remains sub-detonative.

### **6.3 Summary**

This chapter was aimed at demonstrating the pertinent use of an unsteady, real gas assessment in the one-dimensional modeling of the ram accelerator. The modeling shows the influence of the control volume length in determining the ram accelerator performance. Investigations were carried out using computational fluid dynamics solutions of the Reynolds Averaged Navier-Stokes (RANS) equations to numerically simulate the reactive flow around the ram accelerator projectile in the thermally choked propulsive mode. Simulations were carried out for a series of in-coming velocities. The control volume length was determined as a function of the in-coming Mach number; the data was then used in the one-dimensional model. Results from the one-dimensional modeling show a better performance correlation with experimental data.

# Chapter 7

## Conclusion

Our research program focuses on predicting the ram accelerator performances in the thermally choked propulsive mode. Our challenge is the extension of the CFD use for applications where the prediction of some complex physical phenomena in the ram accelerator is unclear and/or requires careful and rigorous strategy of simulation. One of these phenomena is the prediction of the thrust as a function of Mach number in the subdetonative propulsion regime. For these purpose we have applied two approaches:

A one-dimensional computer program was first developed in order to predict the ram accelerator performance. The program called TARAM incorporates the following equations of state: ideal gas, Boltzmann, Percus-Yevick, and Becker-Kistiakowsky-Wilson. The following assumptions have been also taken into account by the program:

- Quasi-steady and unsteady assumption;
- Ideal gas equation and real gas equations of state;
- Different equations of state for the real gas modeling;

- The compressibility effects of unreacted propellant.

The developed numerical tool has been successfully validated by comparing the predicted Chapman-Jouguet speeds against an ongoing experimental data performed at the University of Washington for different gas mixture and fill pressures. Overall, TARAM was found to be a flexible and an accurate tool for modeling the ram accelerator performance. Moreover, the developed tool was able to correctly predict the performance of the ram accelerator within only 1 to 3 minutes.

As a second step, we have used the computational fluid dynamics (CFD) solutions of the Reynolds Averaged Navier-Stokes (RANS) equations to numerically predict the ram accelerator performance in the thermally choked propulsive mode. Simulations were carried out on a two-dimensional axi-symmetric projectile geometry for a series of in-coming velocities. The shear-stress transport turbulence model (SST) and the eddy dissipation combustion model (EDM), with detailed reaction mechanism have been used to simulate the fully turbulent reactive flow field in the ram accelerator. The effect of the radiation/turbulence interactions has been considered in all our simulations. The spherical harmonic P1 method, the gray medium assumption and the Planck-mean absorption coefficients are used to determine the radiative properties of the gas-phase species as a function of temperature. An investigation was carried out to study the accuracy of chemical kinetics mechanisms on the modeling. First, our results revealed that the choice of chemical kinetics mechanism is of critical importance in achieving an accurate numerical simulation of the ram accelerator. The predicted thrust from the CFD simulation was compared with data from a representative experiment at the University of Washington 38-mm-bore facility. In summary, we found

that with careful strategy of modeling the simulations were capable of successfully predicting the experimental data when the projectile remains in the sub-detonative regime. However, when the projectile reaches the trans-detonative regime, simulations failed to predict the pressure in the combustion zone and in the far field.

Remaining discrepancies for the pressure between experiment and the CFD modeling can be attributed to:

- The turbulent combustion modeling in the trans-detonative propulsion regime;
- The neglect of turbulent fluctuations that may be caused by the fins on the projectile body.

These are the subject of ongoing research.

## 7.1 Future work

An interesting continuation of this work could be to conduct 3D RANS simulations and modeling to predict the 3D nature of the flow in the ram accelerator and where the position of the normal shock on the projectile body depend primarily on the history of the flow upstream. In this case the effect of the fins should be considered. It would be also appropriate to adapt the present 2D-RANS approaches such as the five steps kinetics mechanism and the thermal radiation in the 3D-RANS modeling. Since all the data from the experiments are available, it is recommended to consider the projectile acceleration by modeling the unsteady reactive flow. Finally, if provided sufficient computing resources, performing a large eddy simulation "LES" might yield



a more accurate prediction of the large scale turbulent structures, possibly improve the comparison with the available experimental data.

# Appendix A

## Appendix A: One dimensional model

### A.1 Introduction

The one dimensional ram accelerator model was developed at University of Washington [11]. The analytical results were obtained by simple differentiations between the flow upstream and downstream, without taking into account the entropy variation between the initial and final state.

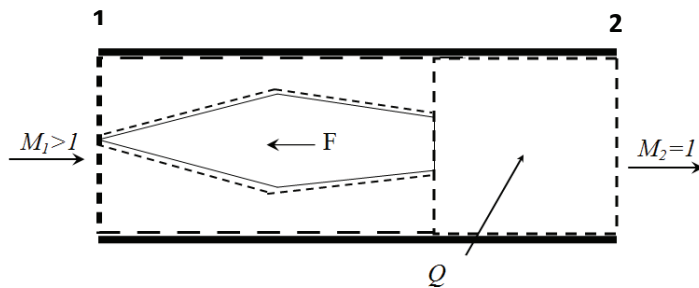


Figure A.1: Control volume model used for the numerical analysis

From the continuity equation:

$$\frac{d}{dt} \int_{CV} \rho dv + \int_A \rho(\vec{u} \cdot \vec{n}) dA = 0 \quad (\text{A.1.1})$$

where  $V$  is the control volume and  $A$  is the cross section. Assuming a steady state assumption Eq.(A.1.1) becomes:

$$\int_{A_1} \rho_1(\vec{u}_1 \cdot \vec{n}_1) dA + \int_{A_2} \rho_2(\vec{u}_2 \cdot \vec{n}_2) dA = 0 \quad (\text{A.1.2})$$

then

$$\rho_1 u_1 A_1 = \rho_2 u_2 A_2 \quad (\text{A.1.3})$$

Moreover, since the cross section is constant, Eq. (A.1.3) becomes

$$\rho_1 u_1 = \rho_2 u_2 \quad (\text{A.1.4})$$

Energy Equation:

$$\frac{d}{dt} \int_{CV} \rho \left( U + \frac{u^2}{2} \right) dv = \int_{CV} \vec{V}_F \cdot \vec{u} dv + \int_A \vec{A}_F \cdot \vec{u} dA \quad (\text{A.1.5})$$

where  $U$  is the internal Energy,  $(\vec{V}_F)$  is the volume forces.  $(\vec{A}_F)$  is surface forces. the volume and the surfaces of the domain are constant.

$$h_1 + h_{f1} + \frac{u_1^2}{2} = h_2 + h_{f2} + \frac{u_2^2}{2} \quad (\text{A.1.6})$$

$$\frac{d}{dt} \int_{CV} \rho \vec{u} dv + \int_A \rho \vec{u} (\vec{u} \cdot \vec{n}) dA = \int_{\Phi} \vec{P} \cdot \vec{n} \cdot dA + \int_A \vec{t} \cdot \vec{n} \cdot dA + \vec{F}_F \quad (\text{A.1.7})$$

$$\rho_1 u_1^2 A_1 + P_1 A_1 + F_F = \rho_2 u_2^2 A_2 + P_2 A_2 \quad (\text{A.1.8})$$

the cross section area ( $A$ ) respectively at station1 and at station2 is constant, equation (1.7) becomes:

$$\rho_1 u_1^2 + P_1 + \frac{F_F}{A} = \rho_2 u_2^2 + P_2 \quad (\text{A.1.9})$$

Next step is to consider the following non-dimensional parameters [Bauer].

The non-dimensional heat release  $Q$ :

$$Q = \frac{(h_{f1} - h_{f2})}{Cp_1 T_1} \quad (\text{A.1.10})$$

where ,  $c_p$  is the specific heat at constant pressure,  $T$  the Temperature, and  $h_f$  is the enthalpy of formation at 0K.

- The non-dimensional thrust  $I$ :

$$I = \frac{F_F}{p_1 A} \quad (\text{A.1.11})$$

- The non-dimensional Pressure  $P$ :

$$P = \frac{p_2}{p_1} \quad (\text{A.1.12})$$

- The non-dimensional volume  $V$ :

$$V = \frac{v_2}{v_1} \quad (\text{A.1.13})$$

- Mach number  $M$ :

$$M = \frac{u}{a} \quad (\text{A.1.14})$$

- The speed of sound  $a$ :

$$a = \sqrt{\Gamma RT} \quad (\text{A.1.15})$$

where

$$\Gamma = \left(\frac{dh}{dU}\right)_s \quad (\text{A.1.16})$$

the equation of state can be written in the form:

$$pv = \sigma RT \quad (\text{A.1.17})$$

where  $\sigma$  is compressibility coefficient. Combining the equation (A.1.8) and (A.1.11) gives:

$$I = \frac{P_2}{P_1} + \frac{u_2^2}{v_2 P_1} - \frac{u_1^2}{v_1 P_1} - 1 \quad (\text{A.1.18})$$

$$I = P + P \frac{a_2^2 M_2^2}{v_2 P_2} - \frac{a_1^2 M_1^2}{v_1 P_1} - 1 \quad (\text{A.1.19})$$

$$I = P + P \frac{\Gamma_2 R_2 T_2 M_2^2}{\sigma_2 R_2 T_2} - \frac{\Gamma_1 R_1 T_1 M_1^2}{\sigma_1 R_1 T_1} - 1 \quad (\text{A.1.20})$$

$$I = P + P \frac{\Gamma_2 M_2^2}{\sigma_2} - \frac{\Gamma_1 M_1^2}{\sigma_1} - 1 = P \left(1 + \frac{\Gamma_2 M_2^2}{\sigma_2}\right) - \frac{\Gamma_1 M_1^2}{\sigma_1} - 1 \quad (\text{A.1.21})$$

with

$$P = \frac{p_2}{p_1} = \frac{v_1 \sigma_2 R_2 T_2}{v_2 \sigma_1 R_1 T_1} \quad (\text{A.1.22})$$

with equation (A.1.4)

$$V = \frac{v_2}{v_1} = \frac{u_2}{u_1} = \frac{M_2 \sqrt{\Gamma_2 r_2 T_2}}{M_1 \sqrt{\Gamma_1 r_1 T_1}} \quad (\text{A.1.23})$$

where

$$\frac{p_2}{p_1} = \frac{M_1 \sqrt{\Gamma_1 R_1 T_1} \sigma_2 R_2 T_2}{M_2 \sqrt{\Gamma_2 R_2 T_2} \sigma_1 R_1 T_1} = \frac{\sigma_2 M_1 \sqrt{\Gamma_1 R_2 T_2}}{\sigma_1 M_2 \sqrt{\Gamma_1 R_1 T_1}} \quad (\text{A.1.24})$$

Equation (A.1.23) and equation (A.1.24) in (A.1.21):

$$I = \frac{\sigma_2 M_1 \sqrt{\Gamma_2 R_2 T_2}}{\sigma_1 M_2 \sqrt{\Gamma_1 R_1 T_1}} \left(1 + \frac{\Gamma_2 M_2^2}{\sigma_2}\right) - \left(1 + \frac{\Gamma_1 M_1^2}{\sigma_1}\right) \quad (\text{A.1.25})$$

Energy equation gives:

$$\eta_1 c p_1 T_1 + h_{f1} + \frac{a_1^2 M_1^2}{2} = \eta_2 c p_2 T_2 + h_{f2} + \frac{a_2^2 M_2^2}{2} \quad (\text{A.1.26})$$

when  $\eta = h/cpT$ .

$$\eta_1 cp_1 T_1 + h_{f1} + \frac{\Gamma_1 R_1 T_1 M_1^2}{2} = \eta_2 cp_2 T_2 + h_{f2} + \frac{\Gamma_2 R_2 T_2 M_2^2}{2} \quad (\text{A.1.27})$$

we use Q (dimensional)

$$T_2(\eta_2 cp_2 + \frac{\Gamma_2 R_2 M_2^2}{2}) = T_1(\eta_1 cp_1 + \frac{\Gamma_1 R_1 M_1^2}{2} + \frac{h_{f1} - h_{f2}}{T_1}) \quad (\text{A.1.28})$$

$$T_2(\eta_2 cp_2 + \frac{\Gamma_2 R_2 M_2^2}{2}) = T_1(\eta_1 cp_1 + \frac{\Gamma_1 R_1 M_1^2}{2} + Q cp_1) \quad (\text{A.1.29})$$

$$\frac{T_2}{T_1} = \frac{cp_1(\eta_1 + \frac{\Gamma_1 R_1 M_1^2}{2cp_1} + Q)}{cp_2(\eta_2 + \frac{\Gamma_2 R_2 M_2^2}{2cp_2})} \quad (\text{A.1.30})$$

$$cp_1(\Gamma_1 - 1) = R_1 \Gamma_1 \quad (\text{A.1.31})$$

$$\frac{T_2}{T_1} = \frac{cp_1(\eta_1 + \frac{(\Gamma_1 - 1)M_1^2}{2} + Q)}{cp_2(\eta_2 + \frac{\Gamma_2 R_2 M_2^2}{2cp_2})} \quad (\text{A.1.32})$$

Finally

$$P = \frac{\sigma_2 M_1 \sqrt{\Gamma_1 R_2}}{\sigma_1 M_2 \sqrt{\Gamma_2 R_1}} \sqrt{\frac{cp_1(\eta_1 + \frac{(\Gamma_1 - 1)M_1^2}{2} + Q)}{cp_2(\eta_2 + \frac{\Gamma_2 R_2 M_2^2}{2cp_2})}} \quad (\text{A.1.33})$$

and

$$I = \frac{\sigma_2 M_1 \sqrt{\Gamma_1 R_2}}{\sigma_1 M_2 \sqrt{\Gamma_2 r_1}} \sqrt{\frac{cp_1(\eta_1 + \frac{(\Gamma_1 - 1)M_1^2}{2} + Q)}{cp_2(\eta_2 + \frac{\Gamma_2 R_2 M_2^2}{2cp_2})}} (1 + \frac{\Gamma_2 M_2^2}{\sigma_2}) - (1 + \frac{\Gamma_1 M_1^2}{\sigma_1}) \quad (\text{A.1.34})$$

note that  $\sigma_1 = 1$  and  $\Gamma_1 = \gamma_1$  for the reactants. This expression for the nondimensional thrust (I) corresponds to the thermally choked propulsive mode when  $M_2 = 1$ .

## A.2 Real gas effects on the prediction of ram accelerator performance

The main idea of this modeling is to describe the aerothermodynamics of the flow around the projectile as a global process between the state of the propellant entering

the control volume and the state of thermally choked exit flow. This modeling is based on the set of one dimensional conservation equations for steady flow presented in Section (A.1) [57]. The preceding equations require the knowledge of series of thermodynamic functions which will be written as follows:

Enthalpy and internal energy may be expressed in the general form:

$$\Psi^{rg} = \Psi^{ig} + \Psi^{ex} \quad (\text{A.2.1})$$

where  $\Phi$  is either the enthalpy or internal energy and  $\Psi^{ex}$  is the correction term of the corresponding parameter. These correction terms may be expressed in the following differential forms [134]:

$$dH^{ex} = (v - T \frac{\partial v}{\partial T}|_p) dp \quad (\text{A.2.2})$$

$$dU^{ex} = (T \frac{\partial p}{\partial T}|_v - p) dv \quad (\text{A.2.3})$$

we introduce a series of operators involving partial derivatives of  $\sigma$  [59]:

$$\sigma_v = v \frac{\partial \sigma}{\partial v}|_T \quad (\text{A.2.4})$$

$$\sigma_T = T \frac{\partial \sigma}{\partial T}|_v \quad (\text{A.2.5})$$

using this operators in Eq. (A.2.2), and (A.2.3) yields:

$$dH^{ex} = RT(\sigma_v + \sigma_T) \frac{dv}{v} \quad (\text{A.2.6})$$

$$dU^{ex} = RT\sigma_T \frac{dv}{v} \quad (\text{A.2.7})$$

the gas correction should also applied to the adiabatic gamma [134]

$$\Gamma = \gamma(1 - \frac{\sigma_v}{\sigma} - n_v) \quad (\text{A.2.8})$$

where

$$n_v = \frac{v}{n} \frac{\partial n}{\partial v} \Big|_T \quad (\text{A.2.9})$$

These parameters involve  $T$  and  $v$  and therefore, they cannot be readily calculated. In order to perform such a calculation one can switch to  $p$  and  $T$  variables which are more representative of the actual inputs of the problem. On the basis of a set of finite difference relationships which can be obtained by a simple equilibrium calculation [100] for two distinct  $p, T$  set of values, namely  $(p, T)$  and  $(p + \delta p), T$ . The value of the dissociation rates,  $n_v$  may thus be derived from the preceding operators:

$$n_v = N_p \frac{v}{p} \frac{\partial p}{\partial v} \Big|_T \quad (\text{A.2.10})$$

where

$$N_p = \frac{p}{n} \frac{\delta n}{\delta p} \Big|_T \quad (\text{A.2.11})$$

It can be shown that the derivatives involved in these expressions can be expressed as functions of the former operators (A.2.4) and (A.2.4) as follows:

$$n_v = -\left(1 - \frac{\sigma_v}{\sigma}\right) \frac{N_p}{1 - N_p} \quad (\text{A.2.12})$$

All the preceding equations depend on the general parameter  $\sigma$  and its derivative. It can be expressed in different forms for different equations of state.

### A.3 Equations of state

Computing the compressibility factor for a given equation of state is the basis for incorporating real gas corrections. Numerous equations of state have been developed based on generalized empirical, and theoretical considerations. Detailed formulations



about each equation of state can be found in [heuzé]. We will give herein the general forms of each EoS incorporated in TARAM.

### A.3.1 Boltzmann

The Boltzmann EoS adequately predicts the Chapman-Jouguet properties when the pressure of combustion products does not exceed 200MPa[Bauer 1985]. This equation of state treats the individual molecules as hard spheres and the mixing rule only accounts for interactions of similar species. The Boltzmann expansion for the compressibility factor is computed by the formula

$$\sigma = 1 + x + 0.626x^2 + 0.287x^3 + 0.193x^4 \quad (\text{A.3.1})$$

where  $x$  is defined:

$$x = \sum_i \frac{X_i B_i}{v_i} \quad (\text{A.3.2})$$

$B_i$  is the co-volume,  $X_i$  is the mole fraction, and  $v_i$  is the specific volume of species  $i$  [100]

### A.3.2 Percus-Yevick

The Percus-Yevick equation of state can be considered a summation of virial development in which the compressibility factor is computed from

$$\sigma = \frac{(1 + z + z^2)}{(1 - z^3)} \quad (\text{A.3.3})$$

where the non-dimensional factor  $z$  is given by

$$z = \frac{\pi}{6} r^{*3} \frac{\widehat{N}n}{V} \quad (\text{A.3.4})$$

where  $\widehat{N}$  is Avogadro's number,  $n$  is the number of moles, and  $V$  is the volume [100]. The characteristic distance term,  $r^*$ , is derived from the interaction law

$$r^* = \lambda \left( \sum_i \sum_j X_i X_j r_{ij}^3 \right)^{1/3} \quad (\text{A.3.5})$$

$$r_{ij} = \frac{r_i + r_j}{2} \quad (\text{A.3.6})$$

where  $r_i$  and  $r_j$  are the molecular diameters of the two interacting species and  $\lambda$  is an adjustable constant.

### A.3.3 Becker-Kistiakowsky-Wilson (BKW)

It was introduced in 1921 by Becker, and modified by Kistiakowsky and Wilson. It can be presented as follows:

$$\frac{PV}{RT} = 1 + x.e^{(\beta x)} \quad (\text{A.3.7})$$

with

$$x = \frac{\kappa B}{V(T + \theta)^\alpha} \quad (\text{A.3.8})$$

and

$$B = \sum_i x_i B_i \quad (\text{A.3.9})$$

where  $\alpha, \theta, \kappa, B_i$  are semi-empirical constants that must be adjusted.  $B_i$  are the co-volumes where there is no link to the co-volume defined by Boltzmann equation. This form of EoS is used for condensed explosive; however, previous research by Bauer et al. [58] and Heuzé et al. [100] shows that this EoS is used for the calculation of detonation characteristics at extremely elevated pressures, however, in this specific case, all the adjustable parameters must be set accordingly. We have used BKW EoS in this present ram accelerator modeling as a reference to show the capability of our

program at incorporating any equation of state.

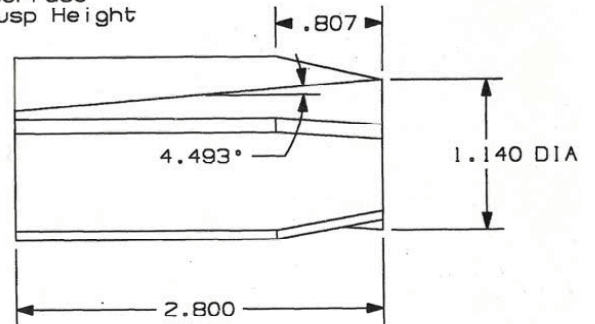
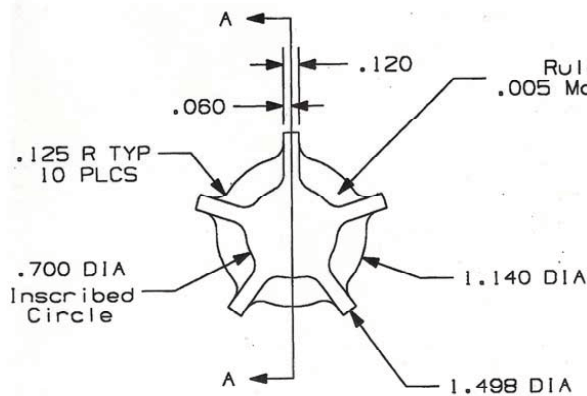
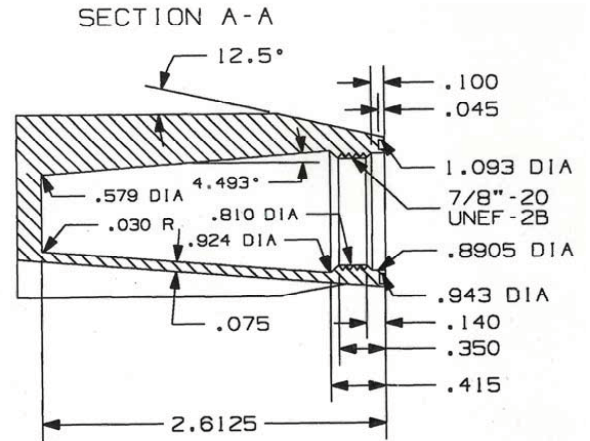
# Appendix B

## Appendix B: Ram accelerator projectile geometry and scaling

Ram Accelerator  
Five Fin Aluminum Body  
18 October 1995

ALL DIMENSIONS IN INCHES  
UNLESS OTHERWISE NOTED

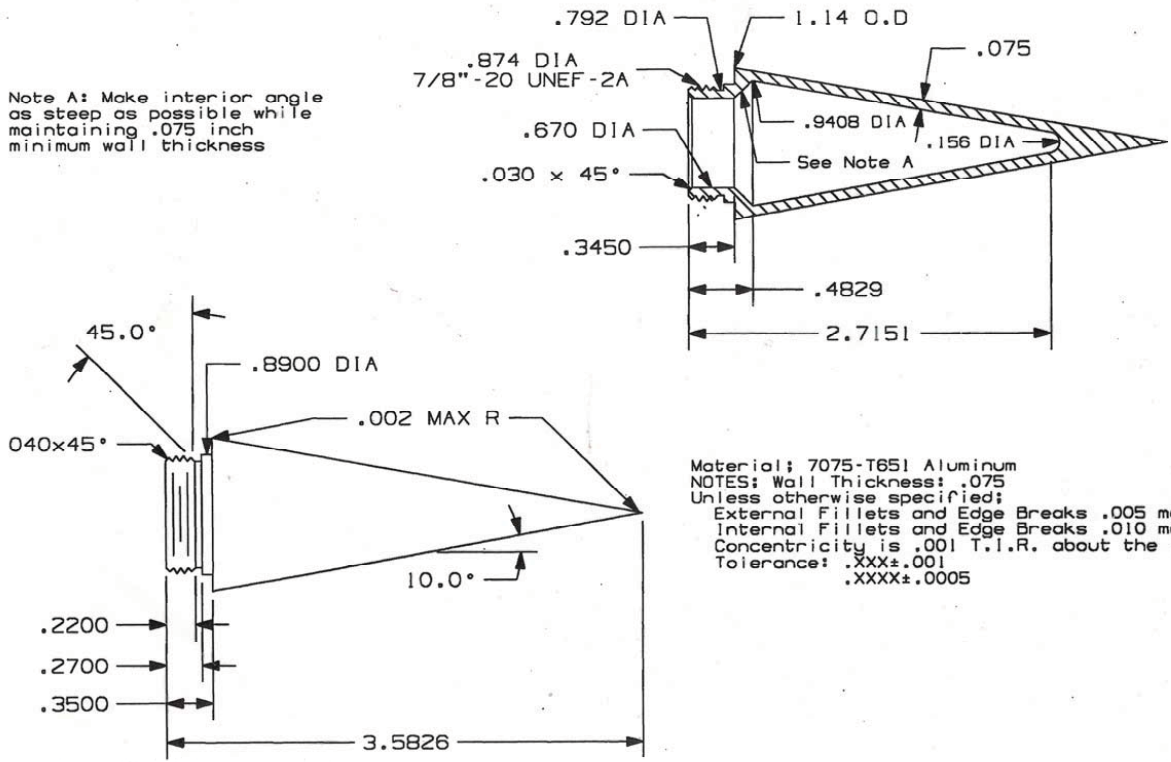
Material: 7075-T651 Aluminum  
NOTES: Wall Thickness: .075  
Unless otherwise specified:  
External Fillets and Edge Breaks .005 max  
Internal Fillets and Edge Breaks .010 max  
Concentricity is .001 T.I.R. about the .890 Dia.  
Tolerance: .xxx±.001  
.xxxx±.0005



Ram Accelerator  
 10° Aluminum Nose Cone  
 11 October 1995

ALL DIMENSIONS IN INCHES  
 UNLESS OTHERWISE NOTED

Note A: Make interior angle as steep as possible while maintaining .075 inch minimum wall thickness



Material: 7075-T651 Aluminum  
 NOTES: Wall Thickness: .075  
 Unless otherwise specified:  
 External Fillets and Edge Breaks .005 max  
 Internal Fillets and Edge Breaks .010 max  
 Concentricity is .001 T.I.R. about the .890 Dia.  
 Tolerance: .XXX±.001  
 .XXXX±.0005

## Appendix C

### Appendix C: Convergence history

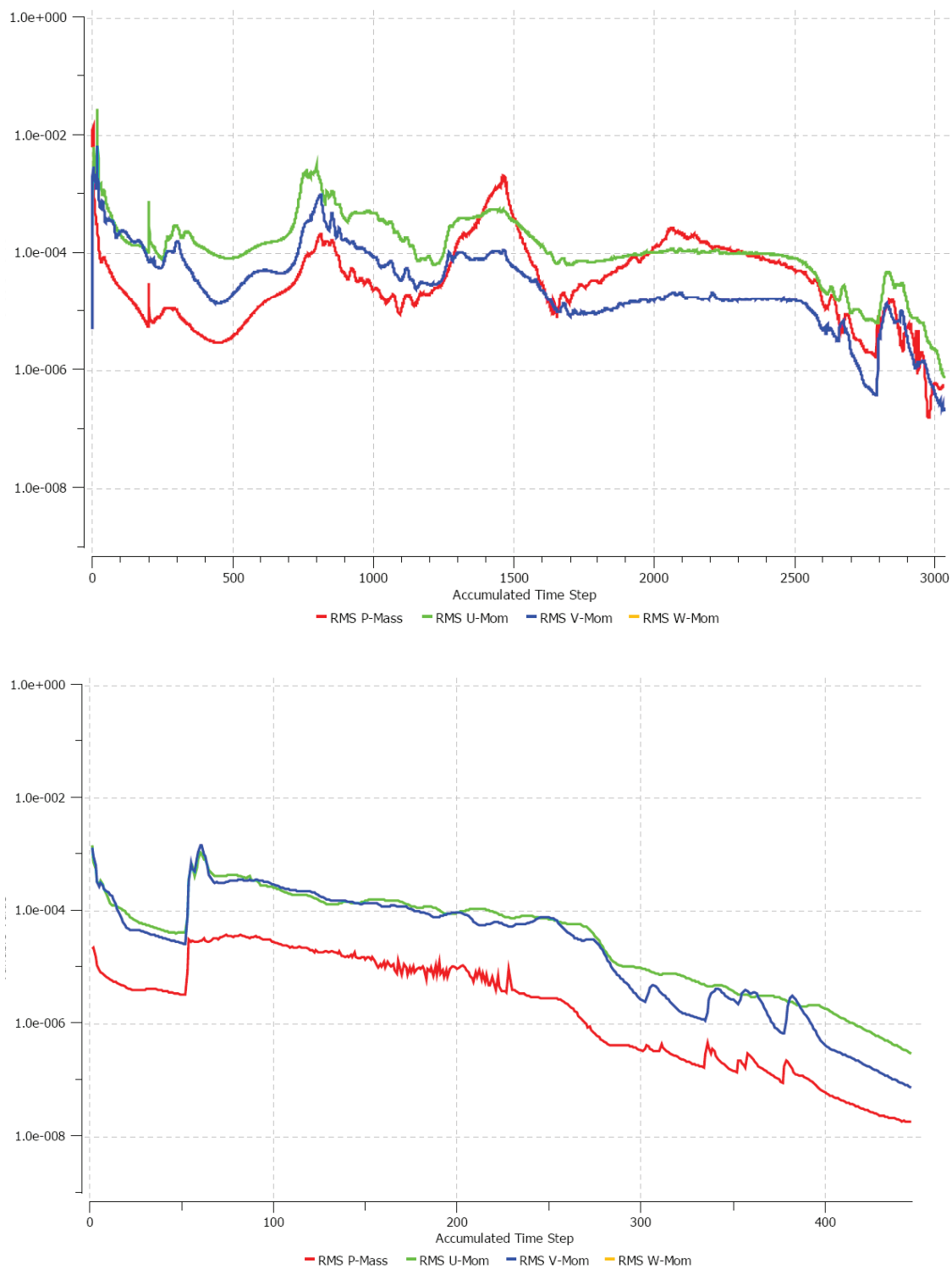


Figure C.1: Convergence history for the velocity and pressure (Top,  $V_0 = 1120 \text{ m/s}$ , Bottom,  $V_0 = 1829 \text{ m/s}$ )

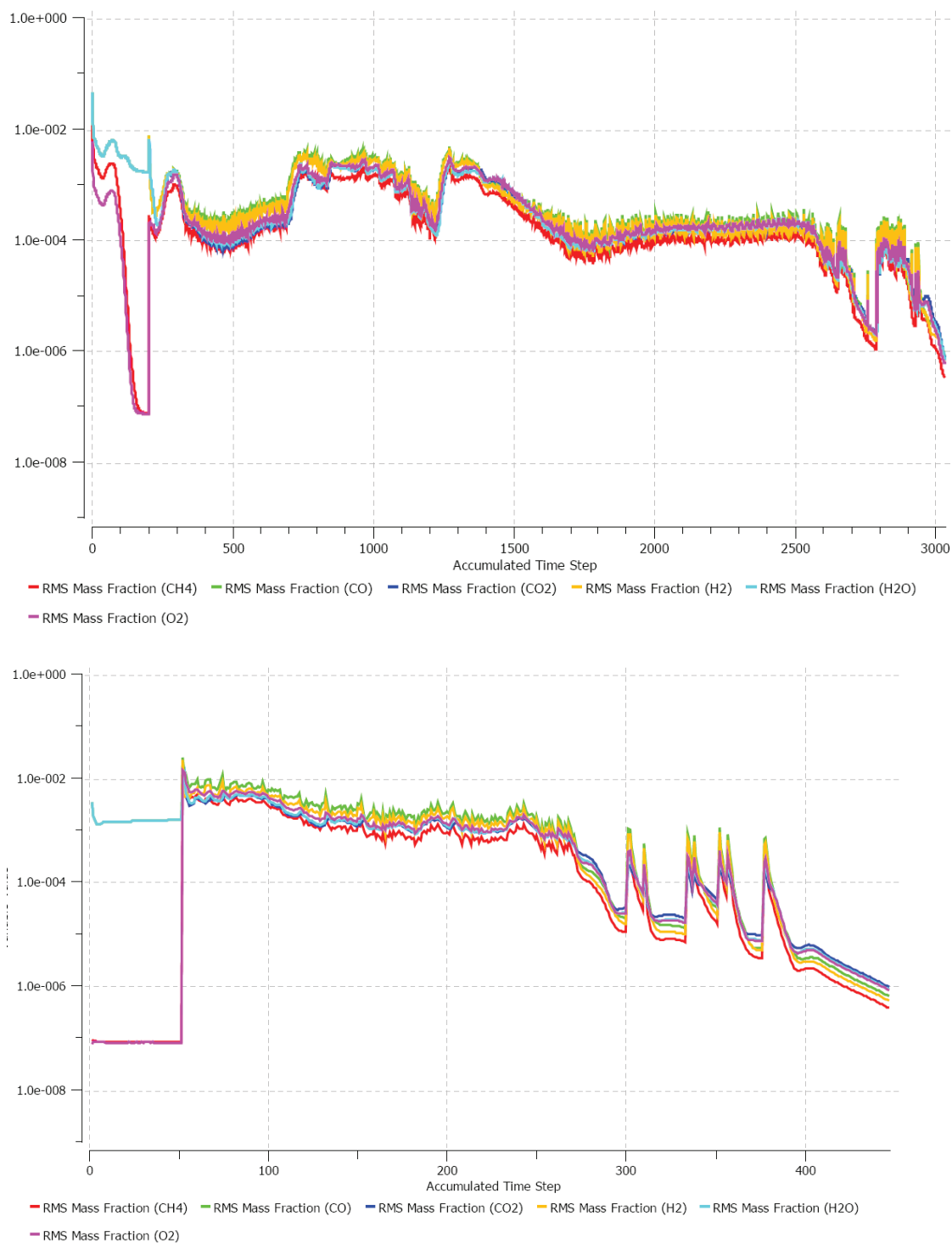


Figure C.2: Convergence history for mass fraction of the fuel and the combustion products (Top,  $V_0 = 1120 \text{ m/s}$ , Bottom,  $V_0 = 1829 \text{ m/s}$ )



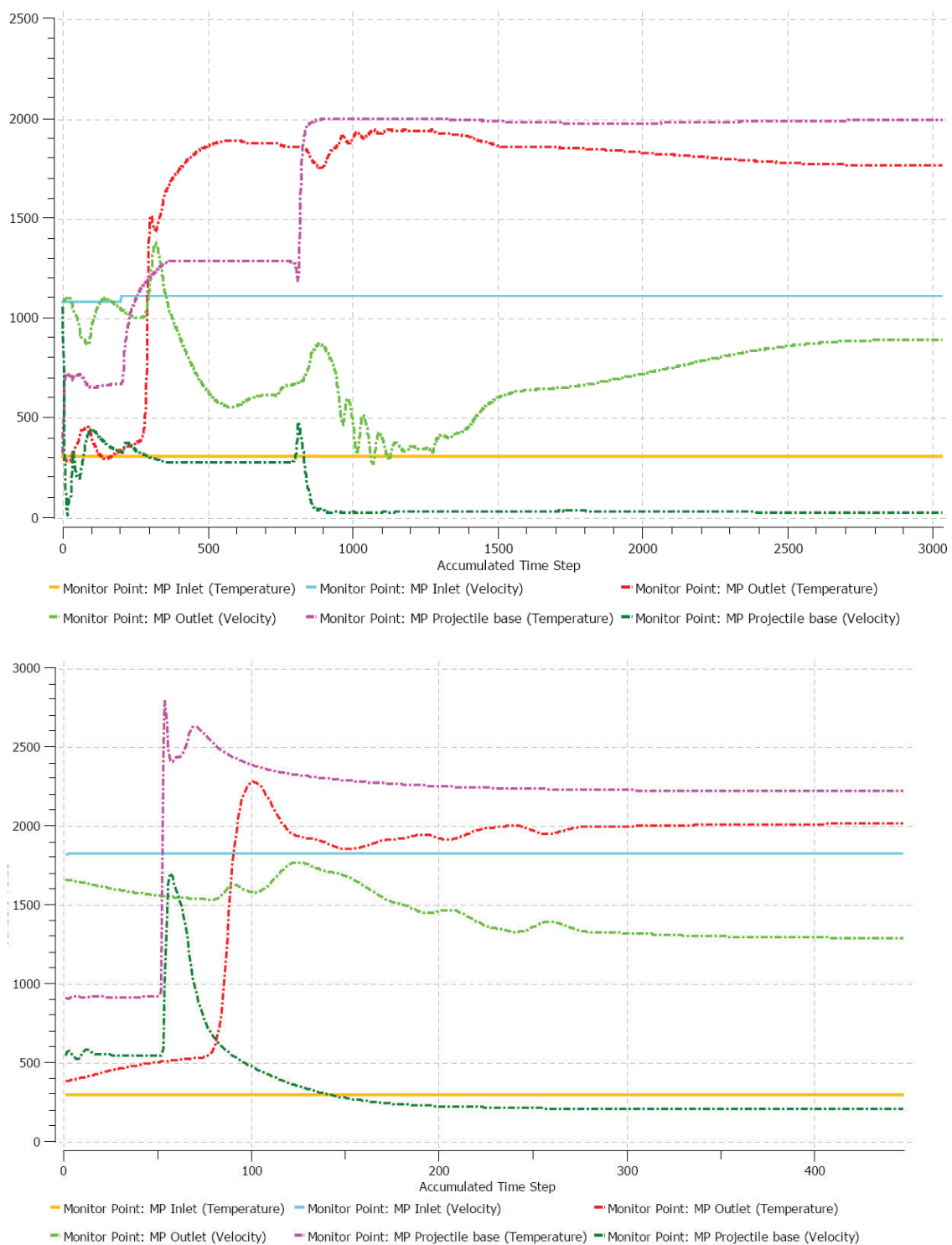


Figure C.3: Monitoring points at different locations in the computational domain showing that the steady state solution has been achieved. i.e., presented here are the Temperature and velocity (Top,  $V_0 = 1120 \text{ m/s}$  , Bottom,  $V_0 = 1829 \text{ m/s}$  )

# Bibliography

- [1] A. Hertzberg, A.P Bruckner, and D.W Bogdanoff. The ram accelerator: A new chemical method of achieving ultra-high velocities. 37th ARA-Meeting. *Quebec, Canada*, 1986.
- [2] A. Hertzberg, A.P Bruckner, D.W Bogdanoff, and C. Knowlen. The ram accelerator and its applications- A new approach for reaching ultrahigh velocities. *16th International Symposium of Shock tubes and waves, Aachen, Federal Republic of Germany*, pages 117–128, 1988.
- [3] A. Hertzberg. Thermodynamics of the ram accelerator. In *American Institute of Physics Conference Proceedings*, volume 208, pages 2–11, 1990.
- [4] C. Knowlen, A.P Bruckner, D.W Bogdanoff, and A. Hertzberg. Performance capabilities of the ram accelerator. *AIAA paper*, pages 87–2152, 1987.
- [5] A.P Bruckner, C. Knowlen, K.A Scott, and A. Hertzberg. High-velocity modes of the thermally choked ram accelerator. In *AIAA, 24th Joint Propulsion Conference, Boston, MA*, 1988.
- [6] A. Hertzberg, A.P Bruckner, and C. Knowlen. Experimental investigation of ram accelerator propulsion modes. *Shock Waves*, 1(1):17–25, 1991.

- [7] A. Hertzberg, E.A Burnham, and J.B Hinkey. Recent advances in ram accelerator technology. *Combustion in High Speed Flows. Kluwer Academic Publishers, Dordrecht*, pages 309–342, 1994.
- [8] C. Knowlen, A.P Bruckner, and A. Hertzberg. Internal Ballistics of the Ram Accelerator. In *13th International Symposium on Ballistics. Stockholm, Sweden*, pages 1–3, 1992.
- [9] C. Knowlen and A.P. Bruckner. Direct space launch using ram accelerator technology. In *AIP Conference Proceedings*, volume 552, page 583, 2001.
- [10] A.E Kull, E.A Burnham, C. Knowlen, A.P Bruckner, and A. Hertzberg. Experimental studies of superdetonative ram accelerator modes. *AIAA, 25th Joint Propulsion Conference, Monterey, CA*, 1996.
- [11] C. Knowlen. *C., Theoretical and Experimental Investigation of the Thermodynamics of the Ram Accelerator in the Thermally Choked Mode*. PhD thesis, Department of Aeronautics and Astronautics, University of Washington, Seattle, WA, 1991.
- [12] G. Chew, C. Knowlen, E.A Burnham, A. Hertzberg, and A.P Bruckner. Experiments on Hypersonic Ramjet Propulsion Cycles up to  $M=8.5$  Using a Ram Accelerator. *AIAA Paper 91-2489*, 1991.
- [13] D.C Brackett and D.W Bogdanoff. Computational investigation of oblique detonation ramjet-in-tube concepts. *Journal of Propulsion and Power*, 5(3):276–281, 1989.

- [14] S. Yungster, S. Eberhardt, and A.P Bruckner. Numerical simulation of shock-induced combustion generated by high-speed projectiles in detonable gas mixtures. *AIAA Paper, 89-0673*, 1989.
- [15] S. Yungster and A.P Bruckner. Computational studies of a superdetonative ram accelerator mode. *Journal of Propulsion and Power*, 8(2):457–463, 1992.
- [16] D. Bogdanoff. Ram accelerator direct space launch system- New concepts. *Journal of Propulsion and Power*, 8(2):481–490, 1992.
- [17] A.J Higgins, C. Knowlen, and A.P Bruckner. An investigation of ram accelerator gas dynamic limits. In *AIAA, 29th Joint Propulsion Conference and Exhibit, Monterey, CA.*, 1993.
- [18] A.J Higgins. Comment on Performance Limits for Projectile Flight in the Ram and External Propulsion Accelerators. *Journal of Propulsion and Power*, 15(1):159, 1999.
- [19] E.A Burnham, A.E Kull, C. Knowlen, A.P Bruckner, and A. Hertzberg. Operation of the ram accelerator in the transdetonative velocity regime. In *AIAA, 26th Joint Propulsion Conference, , Orlando, FL*, page 1990, 1990.
- [20] A.P Bruckner, C. Knowlen, A. Hertzberg, and D.W Bogdanoff. Operational characteristics of the thermally choked ram accelerator. *Journal of Propulsion and Power*, 7(5):828–836, 1991.
- [21] A.P Bruckner, E.A Burnham, C. Knowlen, A. Hertzberg, and D.W Bogdanoff. Initiation of combustion in the thermally choked ram accelerator. In *Shock*

waves; *Proceedings of the 18th International Symposium, Sendai, Japan, July 21-26, 1991, Editors: K. Takayama, A.Sasoh*, volume 1, 1992.

- [22] C. Knowlen, A.J Higgins, A.P Bruckner, and A. Hertzberg. In-tube photography of ram accelerator projectiles. *19th International Symposium on Shock Waves, Marseille, France, 26-30 July 1993*, pages 189–194, 1995.
- [23] C. Knowlen, A.J Higgins, A.P Bruckner, and W. Seattle. Aerothermodynamics of the Ram Accelerator. *AIAA paper, 95-0289*, 1995.
- [24] C. Knowlen, A.J. Higgins, A.P Bruckner, and P. Bauer. Ram accelerator operation in the superdetonative velocity regime. *AIAA paper, 96-0098*, 1996.
- [25] J.E Elvander, C. Knowlen, and A.P Bruckner. High velocity performance of the ram accelerator. *AIAA paper, 96-2675*, 1996.
- [26] J.E Elvander, C. Knowlen, and A.P Bruckner. Recent results of high acceleration experiments in the University of Washington ram accelerator. *AIAA Paper, 97-2650*, 1997.
- [27] C. Bundy, C. Knowlen, and A.P Bruckner. Elevated pressure experiments in a 38-mm bore ram accelerator. *AIAA Paper, 98-3144*, 1998.
- [28] C. Bundy, C. Knowlen, and A.P Bruckner. Ram accelerator operating characteristics at fill pressures greater than 10 MPa. In *AIAA, 35th Joint Propulsion Conference, Los Angeles, CA*, 1999.
- [29] C. Bundy, C. Knowlen, and A.P Bruckner. Investigation of ram accelerator operation at fill pressures up to 20 MPa. In *AIAA, 36th Joint Propulsion Conference, Huntsville, AL*, 2000.

- [30] C. Knowlen, C. Bundy, and A.P Bruckner. Ram accelerator experiments leading to operation at fill pressures up to 20 MPa. In *AIAA Aerospace Sciences Meeting & Exhibit, 40 th, Reno, NV*, 2002.
- [31] C. Bundy, C. Knowlen, and A.P Bruckner. Unsteady Effects on Ram Accelerator Operation at Elevated Fill Pressures. *Journal of Propulsion and Power*, 20(5):801–810, 2004.
- [32] C. Knowlen, A.J. Higgins, P. Harris, and A.P. Bruckner. Hypersonic Shock-Induced Combustion Propulsion. In *47th AIAA Aerospace Sciences Meeting, Orlando, AIAA paper, 2009-715 2009*.
- [33] M. Giraud, J.F Legendre, G. Simon, and L. Catoire. Ram accelerator in 90 mm caliber. First results concerning the scale effect in the thermally choked propulsion mode. In *13th International Symposium on Ballistics, Stockholm, Sweden*, 1992.
- [34] M. Giraud, J.F Legendre, and G. Simon. Ram-accelerator in 90-mm-caliber or RAMAC 90: experimental results concerning the transdetonative combustion mode. In *14th International Symposium on Ballistics, Quebec, Canada*, pages 95–104, 1993.
- [35] M. Giraud, J.F Legendre, and G. Simon. Ram accelerator studies in 90 mm caliber. In *43rd Meeting of the Aeroballistic Range Association, Columbus, OH*, volume 28.

- [36] K.W. Naumann and A.P. Bruckner. Ram accelerator ballistic range concept for softly accelerating hypersonic free-flying models. *Journal of Aircraft*, 31(6): 1310–1316, 1994.
- [37] F. Seiler, G. Patz, G. Smeets, and J. Srulijes. The 30-mm-caliber scram accelerator RAMAC 30 of ISL. In *IUTAM Symposium on Combustion Supersonic Flows, Poitiers, France*, pages 263–272, 1997.
- [38] M. Giraud and H. Simon. Sabot for projectiles of RAM accelerators and projectiles equipped with such a sabot. In *United States Patent No. 5, 394, 805*, 1995.
- [39] M. Giraud, J.F Legendre, and M. Henner. RAMAC in Subdetonative Propulsion Mode: State of the ISL Studies. *Ram Accelerators*, pages 65–77.
- [40] J.F Legendre, M. Giraud, and M. Henner. Ram-accelerator: A new hypervelocity launcher for ballistic studies. *International Journal of Impact Engineering*, 23(1P2):533–545, 1999.
- [41] J.F Legendre and M. Giraud. Enhanced RAMAC performance in subdetonative propulsion mode with semi-combustible projectile. *Eur. Phys. J. AP*, 10(11), 2000.
- [42] J.F Legendre, P. Bauer, and M. Giraud. Helium dilution for ram accelerator operation. *Shock Waves*, 11(5):361–367, 2002.
- [43] M. Henner. Initiation of reactive mixtures in a ram accelerator. In *AIAA, 34th, Joint Propulsion Conference, Cleveland, OH.*, 1998.

- [44] M. Henner, M. Giraud, J.F Legendre, and C. Berner. Initiation of reactive mixtures in a ram accelerator. In *Proceedings of the 33rd Joint Propulsion Conference, July 7-9, Seattle, WA, USA, 1997*, pages 97–3173.
- [45] M. Henner. *Contribution à l'étude de l'effet d'échelle dans les mécanismes d'accélération par effet stato*,. PhD thesis, Dissertation de Thèse de Doctorat de l'Université de Poitiers, France, 1998.
- [46] D.L Kruczynski. Analysis of ram acceleration for high velocity applications. In *AIAA, 27th Joint Propulsion Conference, Sacramento, CA*, 1991.
- [47] D.L Kruczynski and M.J Nusca. Experimental and computational investigation of scaling phenomena in a large caliber ram accelerator. In *AIAA, 28th Joint Propulsion Conference and Exhibit, Nashville, TN.*, 1992.
- [48] D.L Kruczynski. New experiments in a 120-mm ram accelerator at high pressures. *AIAA paper, 93-2589*, 1993.
- [49] D.L Kruczynski. Experiments in a 120-mm Ram Accelerator. In *14th International Symposium on Ballistics, Quebec, Canada, 1993*, 1993–9618156.
- [50] D.L. Kruczynski, F. Liberatore, and M. Kiwan. Flow visualization of steady and transient combustion in a 120-mm ram accelerator. In *AIAA, 30th Joint Propulsion Conference, Indianapolis.*, 1994.
- [51] D.L Kruczynski and F. Liberatore. Ram accelerator experiments with unique projectile geometries. In *AIAA, 31st Joint Propulsion Conference and Exhibit, San Diego, CA*, 1995.



- [52] D.L Kruczynski and F. Liberatore. Experimental investigation of high pressure/performance ram accelerator operation. *AIAA paper, 96-2676*, 1996.
- [53] D.L. Kruczynski, F. Liberatore, and M.J. Nusca. Experimental flow visualization for a large-scale ram accelerator. *Journal of Propulsion and Power*, 12(1): 206–210, 1996.
- [54] D.L Kruczynski. High performance ram accelerator research. In *Ram Accelerators: Proceedings of the Third International Workshop on Ram Accelerators, Held in Sendai, Japan, 16-18 July 1997, Editors: K. Takayama, A.Sasoh*, page 97. Springer Verlag, 1998.
- [55] D.L Kruczynski and M.J Nusca. Experimental and Computational Investigation of Scaling Phenomena in a Large Caliber Ram Accelerator. AIAA paper 92-3245. AIAA 28th Joint Propulsion Conference. Nashville, TN., 1992.
- [56] C. Knowlen and A.P Bruckner. Hugoniot analysis of the ram accelerator. *Shock waves*, pages 617–622, 1991.
- [57] P. Bauer, C. Knowlen, and A. Bruckner. Real gas effects on the prediction of ram accelerator performance. *Shock Waves*, 8(2):113–118, 1998.
- [58] Brochet O Heuze and H. N. Presles P. Bauer, C. Equation of state for dense gases. *Arch Comb*, 5:35–45, 1985.
- [59] P. Bauer and C. Knowlen. Compressibility effects of unreacted propellant on thermally choked ram accelerator performance. *Eur. Phys. J. AP*, 21:233–238, 2003.

- [60] P. Bauer, C. Knowlen, and A.P Bruckner. One-dimensional modeling of ram accelerator at high acceleration rates in the subdetonative velocity regime. *The European Physical Journal Applied Physics*, 29(3):253–258, 2005.
- [61] P. Bauer, C. Knowlen, and A.P Bruckner. Modeling acceleration effects on ram accelerator thrust at high pressure. *Journal of propulsion and power*, 21(5):955–958, 2005.
- [62] S. Yungster and A.P Bruckner. A numerical study of the ram accelerator concept in the superdetonative velocity range. *AIAA Paper*, 89–2677, 1989.
- [63] S. Yungster. Numerical study of shock-wave/boundary-layer interactions in premixed combustible gases. *AIAA journal*, 30(10):2379–2387, 1992.
- [64] S. Yungster. Navier-Stokes simulation of the supersonic combustion flowfield in a ram accelerator. *AIAA Paper*, 91–1916, 1991.
- [65] S. Yungster and M.J. Rabinowitz. Computation of shock-induced combustion using a detailed methane-air mechanism. *Journal of Propulsion and Power*, 10(5):609–617, 1994.
- [66] F. Liberatore. Ram Accelerator Performance Calculations Using a Modified Version of the NASA CET89 Equilibrium Chemistry Code, 1994.
- [67] S. Yungster and K. Radhakrishnan. Computational study of reacting flow establishment in expansion tube facilities. *Shock Waves*, 7(6):335–342, 1997.
- [68] M.J. Nusca. Numerical simulation of reacting flow in a thermally choked ram accelerator projectile launch system. In *AIAA, 27th, Joint Propulsion Conference, Sacramento, CA.*, 1991.

- [69] M.J. Nusca. Numerical simulation of fluid dynamics with finite-rate and equilibrium combustion kinetics for the 120-mm ram accelerator. In *AIAA, 29th, Joint Propulsion Conference and Exhibit, Monterey, CA.*, 1993.
- [70] M.J Nusca. Numerical Simulation of Gas Dynamics and Combustion for 120-mm Ram Accelerator. In *14th International Symposium on Ballistics*, volume 1, pages 261–272.
- [71] M.J Nusca. Navier-Stokes Simulation of Fluid Dynamic and Combustion Phenomena in the RAM Accelerator. In *28th JANNAF Combustion Meeting, CPIA publication*, volume 573.
- [72] C.K. Westbrook and F.L. Dryer. Simplified reaction mechanisms for the oxidation of hydrocarbon fuels in flames. *Combustion Science and Technology*, 27(1):31–43, 1981.
- [73] M. NUSCA. Numerical simulation of ram accelerator performance including transient effects during initiation of combustion and sensitivity studies. In *Johns Hopkins Univ, The 31 st JANNAF Combustion Subcommittee Meeting.*, volume 1, 1994.
- [74] M.J. Nusca. Reacting flow simulation of transient, multi-stage ram accelerator operation and design studies. In *AIAA, 31st Joint Propulsion Conference and Exhibit, San Diego, CA*, 1995.
- [75] S. Yungster and K. Radhakrishnan. Computational study of flow establishment in hypersonic pulse facilities. In *2nd International Workshop on Ram Accelerators, Seattle, WA, United States, 17-20 Jul. Editor C. Knowlen*, 1995.

- [76] M. Soetrisno, S. IMLAY, and D. ROBERTS. Numerical simulations of the superdetonative ram accelerator combusting flow field. In *AIAA, 29th Joint Propulsion Conference, Monterey, CA*, 1993.
- [77] M. Soetrisno and S.T. Imlay. Simulation of the flow field of a ram accelerator. In *AIAA, 27th, Joint Propulsion Conference, Sacramento, CA.*, 1991.
- [78] P. Bauer, M. Henner, and M. Giraud. Numerical investigation of the fin geometry of ram accelerator projectiles in subdetonative propulsion mode. *Eur. Phys. J. AP*, 23:139–145, 2003.
- [79] J.B. Hinkey Jr. A Experimental and Numerical Investigation of the Three-Dimensional Flow Field about a RAM Accelerator Projectile. *PhD dissertation, Department of Aeronautics and Astronautics, University of Washington, Seattle, WA., 1994.*
- [80] M. Henner, M. Giraud, J.F Legendre, and C. Berner. CFD computations of steady and non-reactive flow around fin-guided ram projectiles. In *Ram Accelerators: Proceedings of the Third International Workshop on Ram Accelerators, Held in Sendai, Japan, 16-18 July 1997, Editors: K. Takayama, A.Sasoh*, page 325. Springer Verlag, 1998.
- [81] P. Bauer, M. Henner, J.F Legendre, and M. Giraud. Diameter effect in the initiation process of combustion in a ram accelerator in subdetonative mode. *Eur. Phys. J. AP*, 19:185–194, 2002.

- [82] C. Li, K. Kailasanath, E.S Oran, J.P Boris, and A.M Landsberg. Numerical simulations of transient flows in ram accelerators. In *AIAA, 29th Joint Propulsion Conference, Monterey, CA.*, 1993.
- [83] C. Li, K. Kailasanath, E.S Oran, A.M Landsberg, and J.P Boris. Analysis of Transient Flows in Thermally Choked Ram Accelerator. *AIAA Paper, 93-2187*, 1993.
- [84] S. Bhat. Computational Examination of Parameters Influencing Practicability of Ram Accelerator. *Defence Science Journal*, 54(3):259–270, 2004.
- [85] K.W Naumann. Heating and ablation of projectiles during acceleration in a ram accelerator tube. In *AIAA, 29th Joint Propulsion Conference, Monterey, CA.*, 1993.
- [86] K. Sung, I. Jeung, F. Seiler, G. Patz, G. Smeets, and J. Srulijes. Numerical Study on Effect of Projectile Shape Change by Ablation in RAMAC30. Proc. 21st ICDERS, Poitiers, France.
- [87] E.L. Petersen, D.F. Davidson, and R.K Hanson. Ignition delay times of ram accelerator mixtures. In *AIAA, 32nd Joint Propulsion Conference, Lake Buena Vista, FL.*, 1996.
- [88] M.J. Nusca and D.L. Kruczynski. Reacting flow simulation for a large-scale ram accelerator. *Journal of Propulsion and Power*, 12(1):61–69, 1996.
- [89] M.J. Nusca. Investigation of ram accelerator flows for high pressure mixtures of various chemical compositions. *AIAA paper, 96-2946*, 1996.

- [90] M.J. Nusca. Computational Simulation of the Ram Accelerator Using a Coupled CFD/Interior-Ballistics Approach. *AIAA paper, 97-2653*, 1997.
- [91] M.J. Nusca. Computational simulation of starting dynamics in a ram accelerator. *AIAA Paper, 98-3146*, 1998.
- [92] C. Li and K. Kailasanath. Initiation Mechanism of Thermally Choked Combustion in Ram Accelerators. *Journal of Propulsion and Power*, 15(1), 1999.
- [93] S. Yungster, K. Radhakrishnan, and M.J Rabinowitz. Reacting flow establishment in ram accelerators: a numerical study. *Journal of Propulsion and Power*, 14(1):10-17, 1998.
- [94] J.Y. Choi, I.S. Jeung, and Y. Yoon. Numerical study of scram accelerator starting characteristics. *AIAA*, 36(6):1029-1038, 1998.
- [95] J.Y. Choi, I.S. Jeung, and Y. Yoon. Unsteady simulation of model ram accelerator in expansion tube. *AIAA Paper, 98-3450*, 1998.
- [96] J.Y. Choi, I.S Jeung, and Y. Yoon. Scaling Effect of the Combustion Induced by Shock-Wave Boundary-Layer Interaction in Premixed Gas. In *Symposium International on Combustion*, volume 2, pages 2181-2188, 1998.
- [97] J.Y. Choi, I.S. Jeung, and Y. Yoon. Unsteady state simulation of model ram accelerator in expansion tube. *AIAA journal*, 37(5):537-543, 1999.
- [98] M.J. Nusca. Numerical simulation of the ram accelerator using a new chemical kinetics mechanism. *Journal of Propulsion and Power*, 18(1):44-52, 2002.

- [99] Takayama K. Bauer P. Knowlen C. Hamate Y.. Giraud, M. Bruckner A. Ram Accelerators : History, Principles, Performance and Applications. In *55th Aeroballistic Range Association, Freiburg, Allemagne, September 2004*.
- [100] O. Heuzé. Equations of state of detonation products: Influence of the repulsive intermolecular potential. *Physical Review A*, 34(1):428–432, 1986.
- [101] P. Bauer, H.N Presles, and M. Dunand. Detonation characteristics of gaseous methane-oxygen-nitrogen mixtures at extremely elevated initial pressures. *Dynamics of detonations and explosions: Detonations, AIAA, Vol. 133 of progress in Astronautics and aeronautics.*, pages 56–62, 1991.
- [102] P. Bauer, J.F Legendre, C. Knowlen, and A. Higgins. A review of detonation initiation techniques for insensitive dense methane-oxygen-nitrogen mixtures. *Eur. Phys. J. AP*, 2:183–188.
- [103] M. Champion and P.A. Libby. Turbulent premixed combustion in a boundary layer. *Combustion Science and Technology*, 38(5):267–291, 1984.
- [104] R. Borghi and M. Champion. *Modélisation et théorie des flammes*. Editions Technip. ISBN 2710807580,, 2000.
- [105] F.A. Williams. Combustion theory. *Perseus Books, 1985.*, 1985. ISBN 0201407779.
- [106] T. Poinso and D. Veynante. *Theoretical and numerical combustion*. RT Edwards, Inc., 2005.

- [107] T. Poinso, T. Echekki, and M.G Mungal. A study of the laminar flame tip and implications for premixed turbulent combustion. *Combustion Science and Technology*, 81(1):45–73, 1992.
- [108] D.C. Wilcox. Turbulence modeling for CFD. *DCW Industries, Inc. La Cañada, California*, 1993. ISBN 0963605100.
- [109] F.R Menter. Two-equation eddy-viscosity turbulence models for aerodynamic flows. *AIAA Paper*, 93–2906, 1993.
- [110] KNC Bray, M. Champion, and P.A. Libby. Premixed flames in stagnating turbulence part II. The mean velocities and pressure and the Damköhler number. *Combustion and Flame*, 112(4):635–653, 1998.
- [111] R.G Abdel-Gayed and D. Bradley. Criteria for turbulent propagation limits of premixed flames. *Combustion and flame*, 62(1):61–68, 1985.
- [112] R.G Abdel-Gayed, D. Bradley, and M. Lawes. Turbulent burning velocities: a general correlation in terms of straining rates. *Proceedings of the Royal Society of London. Series A, Mathematical and Physical Sciences*, pages 389–413, 1987.
- [113] W.P Jones and R.P Lindstedt. Global reaction schemes for hydrocarbon combustion. *Combustion and Flame*, 73(3):233–249, 1988.
- [114] D.B Spalding. Thirteenth Symposium International on Combustion. *The Combustion Institute*, page 649, 1971.
- [115] H.B Mason and D.B Spalding. Prediction of reaction-rates in turbulent premixed boundary-layer flows. In *Combustion Institute, European Symposium, Sheffield, England*, pages 601–606, 1973.



- [116] B.F Magnussen and B.H Hjertager. 16th International Symposium on Combustion. *The Combustion Institute, Pittsburgh, Pennsylvania*, page 719, 1977.
- [117] B.R.F. Magnussen. On the structure of turbulence and a generalized eddy dissipation concept for chemical reaction in turbulent flow. In *AIAA, 19th Aerospace Sciences Meeting, St. Louis, Mo.*, 1981.
- [118] B.F Magnussen. The Eddy dissipation concept. In *XI Task Leaders Meeting-Energy Conservation in Combustion, IEA*, 1989.
- [119] A.D Gosman and P.S Harvey. Computer analysis of fuel-air mixing and combustion in an axisymmetric D. I. Diesel. *SAE transactions*, 91(1):121–141, 1982.
- [120] S. Pichon, G. Black, N. Chaumeix, M. Yahyaoui, J.M Simmie, H.J Curran, and R. Donohue. The combustion chemistry of a fuel tracer: Measured flame speeds and ignition delays and a detailed chemical kinetic model for the oxidation of acetone. *Combustion and Flame*, 156(2):494–504, 2009.
- [121] C.A Varnavas and D.N Assanis. Combustion Studies in a Diesel Engine Using a Multidimensional Engine Simulation. Technical report, ASME 91-ICE-2, 1991.
- [122] Lebrere L Neveu F. Dillies B, Ducamin A. Direct injection Diesel engine simulation: A combined numerical and experimental approach from aerodynamics to combustion. Technical report, SAE 970880, 1997.
- [123] A. Harten. High resolution schemes for hyperbolic conservation laws. *Journal of computational physics*, 135(2):260–278, 1997.

- [124] B. van Leer. Upwind and high-resolution methods for compressible flow: From donor cell to residual-distribution schemes. *Communications in Computational Physics*, 1(2):192–205, 2006.
- [125] B.E Launder and D.B Spalding. The numerical computation of turbulent flows. *Computer methods in applied mechanics and engineering*, pages 269–289, 1990.
- [126] M.F. Modest. *Radiative heat transfer*. Academic Press, 2003.
- [127] M.P Menguc and B.W Webb. Radiative heat transfer. *Coal science and technology*, 20:375–431, 1993.
- [128] R.E Marshak. Note on the spherical harmonic method as applied to the Milne problem for a sphere. *Physical Review*, 71(7):443–446, 1947.
- [129] R.C. Haskell, L.O. Svaasand, T.T. Tsay, T.C. Feng, M.S. McAdams, and B.J. Tromberg. Boundary conditions for the diffusion equation in radiative transfer. *Journal of the Optical Society of America A*, 11(10):2727–2741, 1994.
- [130] E.L Petersen, D.F Davidson, and R.K Hanson. Ignition Delay Times of Ram Accelerator CH<sub>4</sub>/O<sub>2</sub>/Diluent Mixtures. *Journal of Propulsion and Power*, 15(1):82–91, 1999.
- [131] M.J Nusca. Numerical simulations of unsteady ram accelerator flow phenomena. In *Ram Accelerators: Proceedings of the Third International Workshop on Ram Accelerators, Held in Sendai, Japan, 16-18 July 1997, Editors: K. Takayama, A.Sasoh*, page 305. Springer Verlag, 1998.
- [132] Barlow R. S. Chen J.-Y. Smith, N. S. A. and R. W Bilger. *Combust. Flame* 117:4-31.

- [133] W.L Grosshandler. RADCAL: A narrow-band model for radiation calculations in a combustion environment. NIST Technical Note 1402 (April). 1993.
- [134] A. Amaee W. Byers. Review of Equation of State of Fluids Valid to High Densities. *Departement of Chemistery, University of Manchester, UK*, Report 39/1992, 1992.
- [135] T. Bengherbia, Y. Yao, and P Bauer. Computational Investigation of Transitional Viscous Flow over a Ram Accelerator Projectile in Sub- Detonative Propulsion Mode. In *AIAA 2006-0558, January 2006*.
- [136] S.C Li and F.A Williams. Reaction mechanisms for methane ignition. *Journal of Engineering for gas turbines and power*, 124:471, 2002.
- [137] P.L. Houston. *Chemical kinetics and reaction dynamics*. Dover Publications, 2006, 2006 ISBN 0486453340.
- [138] J. Warnatz, U. Maas, and R.W. Dibble. *Combustion: physical and chemical fundamentals, modeling and simulation, experiments, pollutant formation*. Springer Verlag, 2006.
- [139] H.K. Versteeg and W. Malalasekera. *An introduction to computational fluid dynamics: the finite volume method*. Prentice Hall, 2007.
- [140] F.M El-Mahallawy and S.E.D Habik. *Fundamentals and technology of combustion*. Elsevier Boston, 2002.
- [141] B.F Magnussen. Modeling of NO<sub>x</sub> and soot formation by the Eddy Dissipation Concept. In *Int. Flame Research Foundation, 1st Topic Oriented Technical Meeting*, pages 17–19, 1989.

- [142] D. Bradley, P.H Gaskell, and X.J Gu. Burning velocities, Markstein lengths, and flame quenching for spherical methane-air flames: A computational study. *Combustion and Flame*, 104(1-2):176–198, 1996.
- [143] J.O Hinze. Turbulence: an Introduction to its Mechanism and Theory (2nd edn), 1975.
- [144] KNC Bray, M. Champion, and P.A. Libby. Premixed flames in stagnating turbulence part IV: a new theory for the Reynolds stresses and Reynolds fluxes applied to impinging flows. *Combustion and Flame*, 120(1-2):1–18, 2000.
- [145] KNC Bray, M. Champion, and P.A. Libby. Pre-mixed flames in stagnating turbulence Part V: evaluation of models for the chemical source term. *Combustion and Flame*, 127(1-2):2023–2040, 2001.
- [146] P. Bailly, M. Champion, and D. Garreton. Counter-gradient diffusion in a confined turbulent premixed flame. *Physics of Fluids*, 9:766, 1997.

## **Contribution à l'étude des performances d'un accélérateur à effet stato en régime sous-détonatif**

L'accélérateur par effet stato en régime sous-détonatif, caractérisés par une vitesse du projectile inférieure à la célérité de la détonation dans le mélange considéré est, à l'heure actuelle, le mieux connu. La compréhension des phénomènes mis en jeu dans cette technologie est subordonnée à une importante étude expérimentale associée à la mise au point de moyens numériques. C'est l'objet du travail présenté dans ce mémoire qui décrit numériquement, à l'aide d'un code CFD de combustion turbulente, le processus de combustion qui s'opère autour du projectile. Les résultats, comparés aux données expérimentales existantes disponibles au Laboratoire de l'Université de Washington, ont permis de parfaire la fiabilité d'un code de calcul monodimensionnel en régime sous-détonatif. Les calculs analytiques font intervenir des équations d'état dont la validité est discutée. La poussée générée par l'accélérateur est calculée et les valeurs déduites de cette analyse 1D sont en excellent accord avec les expériences. Cette démarche a pour but d'apporter une contribution en termes de prédiction des performances de poussée d'un accélérateur à effet stato et de choix du mélange réactif optimal.

## **Contribution to numerical simulation analysis of the flow in the ram accelerator in Subdetonative combustion mode**

The purpose of this work is to examine in details the flow field characteristics of the thermally choked ram accelerator using five step kinetic reaction mechanisms. The results from the simulations are compared with experimental values from representative experiments at the University of Washington 38-mm-bore facility. The data that were used for comparison with theory were derived from experiments performed in a 16-m-long tube with CH<sub>4</sub>/O<sub>2</sub>/N<sub>2</sub> propellant mixtures at pressures on the order of several MPa. The data derived from these CFD calculations were used to implement a one-dimensional computer code which has been developed to predict the thrust in the thermally choked combustion mode and is aimed at providing data over a wide range of initial pressures, where the steady state calculation is no longer valid and the real gas effects must be accounted for. This code includes both steady and unsteady state calculations, using several equations of state. The predicted thrust and velocity agree well with experimental values. The code, which requires simple data input and very low computer capabilities, provides an easy and rapid access to the prediction of the ram accelerator performance in the thermally choked combustion regime, over a wide range of mixture compositions and fill pressures.

### **Mots clefs**

Simulation numérique, accélérateur, propulsion, supersonique, combustion, détonation, onde de choc, CFD